

8

Center for  
Materials Science and Engineering  
The University of Texas  
at Austin

AD-A147 504

TITANIUM MATRIX/CONTINUOUS FIBER COMPOSITE INTERFACE INTERACTIONS  
AND THEIR INFLUENCE ON MECHANICAL PROPERTIES

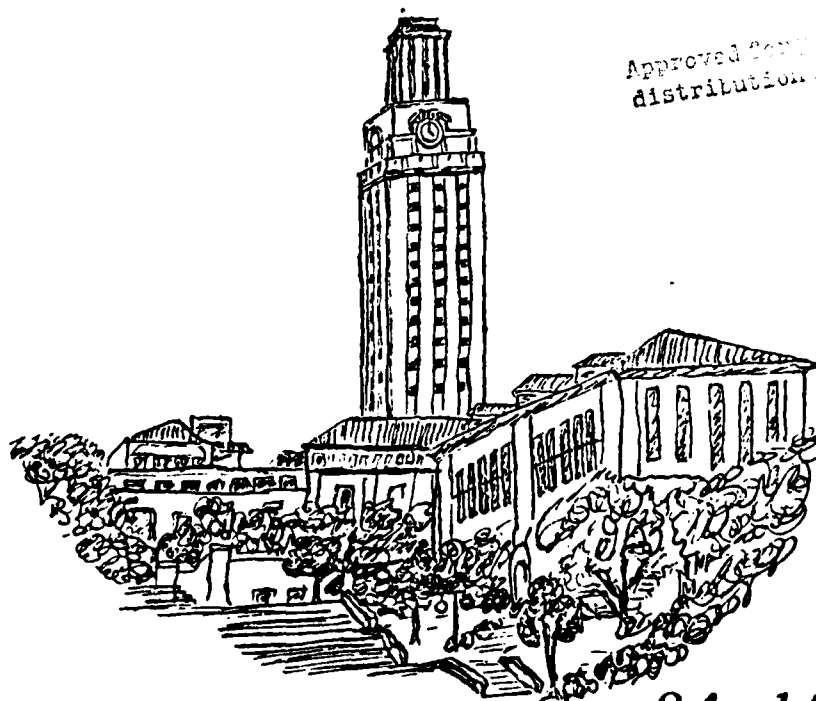
HARRIS L. MARCUS  
PRINCIPAL INVESTIGATOR

Final Technical Report  
Grant No. AFOSR 80-0052

Report No. UTCMSE-84-2  
1 Jan 1980 - 31 May 1984

Department of Mechanical Engineering/Center for Materials Science and Engineering

DTIC FILE COPY



Approved for  
distribution

DTIC  
ELECTE  
NOV 5 1984  
S D

84 10 26 051

Final Technical Report  
Grant No. AFOSR 80-0052  
The University of Texas at Austin  
Final Reporting Period: 1 January 1980 - 31 May 1984

TITANIUM MATRIX/CONTINUOUS FIBER COMPOSITE  
INTERFACE INTERACTIONS AND THEIR INFLUENCE  
ON MECHANICAL PROPERTIES

Accession For	
NTIS GRA&I	<input checked="" type="checkbox"/>
DTIC TAB	<input type="checkbox"/>
Unannounced	<input type="checkbox"/>
Justification	
By	
Distribution/	
Availability Codes	
Dist	Avail and/or Special
A/1	



CONFIDENTIAL

Principal Investigator

Harris L. Marcus, Professor  
Mechanical Engineering/Materials Science and Engineering

Report Number: UTCMSE-84-2

SECURITY CLASSIFICATION OF THIS PAGE (When Data Entered)

REPORT DOCUMENTATION PAGE		READ INSTRUCTIONS BEFORE COMPLETING FORM
1. REPORT NUMBER <b>AFOSR TR- 84-0812</b>	2. GOVT ACCESSION NO. <b>AD-A147504</b>	3. RECIPIENT'S CATALOG NUMBER
4. TITLE (and Subtitle) Titanium Matrix/Continuous Fiber Composite Interface Interactions and Their Influence on Mechanical Properties	5. TYPE OF REPORT & PERIOD COVERED Final Technical Report 1 Jan 1980 - 31 May 1984	
7. AUTHOR(s) H.L. Marcus	6. PERFORMING ORG. REPORT NUMBER UTCMS-84-2	
9. PERFORMING ORGANIZATION NAME AND ADDRESS Department of Mechanical Eng./MS&E The University of Texas at Austin Austin, TX 78712	8. CONTRACT OR GRANT NUMBER(s) AFOSR 80-0052	
11. CONTROLLING OFFICE NAME AND ADDRESS Department of the Air Force AFOSR/NE, Air Force Office of Scientific Research Bolling AFB, DC 20332	10. PROGRAM ELEMENT, PROJECT, TASK AREA & WORK UNIT NUMBERS  61102F, 2306, A1	
14. MONITORING AGENCY NAME & ADDRESS (if different from Controlling Office)	12. REPORT DATE 6 August 1984	
	13. NUMBER OF PAGES	
	15. SECURITY CLASS. (of this report) Unclassified	
	15a. DECLASSIFICATION/DOWNGRADING SCHEDULE	
16. DISTRIBUTION STATEMENT (of this Report)  Approved for public release and distribution unlimited.		
17. DISTRIBUTION STATEMENT (of the abstract entered in Block 20, if different from Report)		
18. SUPPLEMENTARY NOTES		
19. KEY WORDS (Continue on reverse side if necessary and identify by block number) fracture, fatigue crack growth, titanium metal matrix composites, environmental effects, fatigue, AES, thermal fatigue, mixed mode fracture, SiC, B <sub>4</sub> C/B, interface diffusion, Borsic, TEM of MMC.		
20. ABSTRACT (Continue on reverse side if necessary and identify by block number) Research on the influence of the interface on the mechanical properties of Ti-6Al-4V metal matrix composites (MMC) containing Borsic, SiC and B <sub>4</sub> C/B continuous fibers is reported. The potential high temperature application of the Ti MMC was the basis for thermal fatigue experiments.  The mechanical measurements included monotonic and cyclic mixed mode testing. In the testing it is found that the crack follows the matrix/fiber interface for angles from transverse loading up to about 45° and propagates		

1405

SECURITY CLASSIFICATION OF THIS PAGE(When Data Entered)

normal to the fiber for higher angles and longitudinal loading. This leads to properties that are bimodal in behavior, poor in the first case and higher in the second case. Degradation of the interfaces modified by thermal cycling has a much larger effect on the longitudinal properties. The transverse properties are dominated by the matrix properties. H<sub>2</sub>O and H<sub>2</sub> gaseous environments increase the room temperature fatigue crack growth rate for all the materials in all conditions tested.

→ An analysis of diffusion down the interface and into the matrix is described and data presented for both thermal fatigue and isothermal treatments. The interface diffusion is about 10<sup>5</sup> greater than the coupled diffusion into the matrix.

TEM, EELS and AES results show the interfaces in the Ti MMC to contain very complex chemical, crystallographic and morphological features that are modified by exposure to humidity or a sulfur bearing environment.

In addition segregation to the interface and its effect on the cohesive energy was analyzed with a non-equilibrium thermodynamics model

↑



## INDEX

	<u>Page</u>
I. Introduction	1
II. Results and Discussion	2
A. Mixed Mode Crack Growth	2
B. Thermal Fatigue and Fatigue Crack Growth	5
C. Interface Diffusion	6
D. Interface Decohesion and Impurity Elements	7
E. TEM of Ti MMC Interfaces	7
III. Summary	8
IV. Personnel Involved in Research	10
V. Dissertations/Thesis	10
VI. Publications	10
APPENDIX A - "Mixed Mode Crack Propagation in Continuous Fiber Metal Matrix Composites"	13
APPENDIX B - "Mixed Mode Fracture in Titanium Metal Matrix Composites"	25
APPENDIX C - "Environmental Influences on the Fracture and Fatigue Properties of Titanium Metal Matrix Continuous Fiber Composites"	33
APPENDIX D - "Environmentally Influenced Mixed Mode Fatigue Crack Propagation of Titanium Metal Matrix Composites"	70
APPENDIX E - "Influence of Interface Degradation and Environment on the Thermal and Fracture Fatigue Properties of Titanium Matrix/Continuous SiC Fiber Composites"	78
APPENDIX F - "Fatigue Crack Growth Behavior of Ti-6Al-4V Metal Matrix/Continuous SiC and B <sub>4</sub> C/B Fiber Composites"	89

APPENDIX G - "Interface Diffusion Studies in Titanium Metal Matrix/Continuous SiC and B <sub>4</sub> C/B Fiber Composites"	112
APPENDIX H - "The Influence of Alloying Ele- ments on Impurity Induced Grain Boundary Embrittlement"	149
APPENDIX I - "TEM and EELS Interfacial Studies of Ti Metal Matrix Composites"	165

# TITANIUM MATRIX/CONTINUOUS FIBER COMPOSITE INTERFACE INTERACTIONS AND THEIR INFLUENCE ON MECHANICAL PROPERTIES

## I. Introduction

Filamentary metal-matrix composites have generated a considerable amount of interest in the materials field because of their potential applications in dynamic structures. A metal matrix composite system (MMC) carries certain distinct advantages over other composite systems. High strength, modulus, toughness, surface durability, and low notch sensitivity are just a few of these potential advantages over other composite systems.

Titanium metal matrix composites are attractive for applications requiring a stronger matrix and higher temperature capability than other metal matrix composites. Applications requiring high stiffness and low weight in the 450-800 °K temperature range will benefit from the development of titanium matrix composites.

In the research reported on here, various experiments and analyses were done to study the effects of temperature and other environments on the interfaces and the mechanical properties of the titanium metal matrix composites reinforced with SiC, Borsic or B<sub>4</sub>C/B fibers. Specimens of longitudinal and transverse fiber orientation as well as mixed mode orientations were used in the mechanical tests.

The mechanical properties studied are mixed mode loading residual strength after thermal and thermal fatigue exposure and fatigue crack growth under Mode I and Mixed Mode loading after thermal treatment and in various gaseous environments. The condition of the

matrix fiber interface as a function of the above treatments is characterized with both Scanning Auger Microscopy (SAM), Transmission Electron Microscopy (TEM) and Scanning Electron Microscopy (SEM). The fiber interface chemistries were modified by thermal treatment in oxygen and sulfur bearing environments, under isothermal and thermal fatigue conditions.

The composite materials used in this investigation are Ti-6Al-4V metal matrix reinforced with about 40 V%, Borsic,  $B_4C/B$  or SiC filaments. Materials were obtained in the form of sheet panels through the Air Force Materials Laboratory. The composite panel was cut by electric-discharge-machine (EDM) into specimens.

## II. Results and Discussion

The results obtained during this research are given in great detail in Appendices A-I, most of which are copies of reprints or preprints of published papers. In this part of the report the key observations will be summarized and the reader will be referred to the appendices for the details. Appendices A-D focus on the nature of mixed mode crack propagation. Appendices E and F describe fatigue crack growth and thermal fatigue effects on the composites. Appendix G details the experimental results of interface diffusion studies and the two-dimensional diffusion analysis. Appendix H is a thermodynamic approach to interface cohesion as influenced by segregation. Appendix I shows the results of TEM analysis of the interfaces of the Ti-MMC.

### A. Mixed Mode Crack Growth

In the continuous fiber metal matrix composites there are two primary directions, the longitudinal parallel to the fiber and the

transverse normal to the fiber. Of more general interest is how a crack will propagate when the fibers are loaded at an arbitrary angle to the load axis, commonly identified as mixed mode loading. Appendices A-C describe a series of experiments on the mixed mode fracture of the Ti-6Al-4V MMC with SiC, Borsic and B<sub>4</sub>C/B fibers. Both fracture and fatigue crack growth measurements were made on the as-received composites and on samples isothermally and thermally-fatigued in air, sulfur and vacuum environments. For monotonically loaded fracture specimens, the crack propagated in a self-similar manner from 0° to 45° and normal to the fiber for 60° and above. The fracture stress was very dependent on the method of crack propagation. The cracks that propagated normal to the fiber showed the maximum failure stress and those that propagated in a self-similar manner the lowest fracture energy. This corresponds to interface failure combined with fiber splitting.

The impact of thermal treatments that result in oxygen or sulfur at the interface on the fracture behavior is a severe degradation of the longitudinal fracture strength. This is basically due to the setting of notches at the fiber. Only a limited amount of reduction in fracture stress occurs in the cracking that is self-similar including the transverse strength. This is due to the majority of the transverse strength comes from the matrix. A simple model of the fibers as holes gives support to this explanation. The fracture stress when occurring in a self-similar manner can be approximated by the strain energy release at fracture model in an orthotropic material given by  $G_F = G_I + G_{II}$ .  $G_I$  and  $G_{II}$  are the strain energy release components under mode I and mode II loading.

The model was extended further into the fatigue crack growth behavior. The fatigue crack growth was found to follow the form

$$da/dN \propto (\Delta G/GF)^m$$

when propagation was self-similar.  $\Delta G = \Delta G_I + \Delta G_{II}$ .

The above did not explain the modification in the growth rate when a gaseous environment was present during the fatigue crack growth. Humid environments tended to increase the crack growth rate. The fatigue crack growth rate increased as one went from longitudinal loading to transverse loading. In each case humid air showed an increase in crack growth rate when compared to tests in vacuum.

A significant problem was associated with separating the relative importance of interface failure and fiber splitting on the crack growth rate. Prior thermal treatment, gaseous environments and load ratio all impact the fatigue crack growth rate. What is clear is that mixed mode fracture and fatigue crack growth is a complex phenomenon strongly affected by mechanical, metallurgical and environmental parameters. Any model must be used carefully due to the uncertainty in the interfaces, the K calibration, and the interactions with the environment. The reader is referred to Appendices A-D for the details of the results of the mixed mode fracture studies in the Ti MMC.

### B. Thermal Fatigue and Fatigue Crack Growth

One of the potential applications of Ti MMC is for use at elevated temperatures, as high as 550°C. Usually involved in the applications are thermal excursions that can lead to extreme thermal fatigue problems that arise due to the mismatch in coefficients of thermal expansion between the fiber and the matrix. Appendices D-F discuss the influence of the thermal cycling on the ambient fatigue crack growth behavior. The fatigue crack growth studies were run in vacuum, humid air and hydrogen environments. The thermal cycling was done in vacuum, air and a sulfur environment. The influence of the environment on the interface was established with the SEM and AES. The fractography results showed that the oxygen and sulfur diffusion down the interface produced a brittle layer that split and degraded the longitudinal properties. A much thicker layer of both the oxide and the sulfide was observed when thermal fatigued then under isothermal aging for the same elevated temperature exposure. The impact on the fracture properties of the interface phases shows that thermal fatigue was much more damaging than isothermal exposure.

The H<sub>2</sub> and H<sub>2</sub>O gaseous environmental effect was most pronounced when the sulfur rich layer was present. This is explained in terms of the hydrogen-sulfur interactions reducing the cohesive energy normal to the interface. Dry hydrogen is not as severe an embrittler in terms of the fatigue crack growth as the humid air, but does increase crack growth rate when compared to dry N<sub>2</sub> or vacuum air. The details of these experiments are in Appendices D-F.

Additional studies trying to uniquely separate out interface from fiber splitting impact on fatigue crack growth were done.

SEM fractography of matching sides of the fracture surfaces were studied. What was observed is that the correlations found between the fatigue crack mode of failure and the other controlled variables, and reported in the Appendices, contained a large statistical variation. Much of this is due to the influence of the Mode III component that is applied during an unloading cycle in the thin plate material used. Other contributions come from the variability of the local notch effects from the interface region and the variability in both interface strength and the transverse fracture strength of the fibers.

### C. Interface Diffusion

In an attempt to quantify the diffusion of both oxygen and sulfur from the environment down the interface between the Ti-6Al-4V matrix and the fibers a series of diffusion experiments were run. In addition a 2-dimensional analysis of the diffusion down the interface and normal to the interface was performed. Included are results of the interface modifications due to thermal cycling treatments between room temperature and 550°C and isothermal treatments at 550°C in gaseous sulfur and air environments. The interaction between the sulfur environment and the titanium MMC (Ti-6Al-4V/SiC and B<sub>4</sub>C/B) fiber interfaces was evaluated in terms of interface diffusion. The diffusion down the interface was enhanced under the thermal cycling conditions. The 550°C sulfur interface diffusion coefficient was found to be  $5 \times 10^{-9}$  cm<sup>2</sup>/sec for the SiC composites and  $7 \times 10^{-9}$  cm<sup>2</sup>/sec for the interface diffusion in B<sub>4</sub>C/B composites.

In addition to the diffusion down the interface, diffusion into the matrix was studied with combined scanning Auger microscopy



and inert ion sputtering. The rapid diffusion down the boundary was separated from the slow diffusion into the bulk resulting in two one-dimensional analyses. The sulfur diffusion down the interface was much larger than that into the bulk, a  $10^5$  difference in diffusion distance.

The details of the study are presented in Appendix G.

#### D. Interface Decohesion and Impurity Elements

As part of a broad base nonequilibrium thermodynamic analysis of the influence of segregating impurity elements on the fracture behavior of interfaces, Appendix H, the MMC composites were analyzed. In this limited model of MMC, the assumption was that impurity segregation was only from the matrix. A strong case can be made for this due to limited solubility of many elements in the fibers. In the Ti MMC this is particularly true for the Cl and S impurities originating in the Ti matrix. With this and several other assumptions a calculable impact on the fracture behavior of segregation is possible for the composites. The data reported in Appendix H is for grain boundary segregation in a series of steels alloyed to test the predictions of the model. For these systems the model correlates to a high degree with the observed results.

#### E. TEM of Ti MMC Interfaces

In order to determine the crystallography of the interface phases samples of the Ti MMC were ion thinned to produce thin foils of the interfaces of the various systems for TEM, STEM and EELS analysis. The detailed results including the sputter parameters are reported in Appendix I.

In the as-received Ti-6Al-4V/SiC specimens, TiO, TiC and TiO<sub>2</sub> were identified. For samples thermal cycling in a sulfur environment TiS<sub>2</sub> was the sulfide identified.

TiO and TiB<sub>2</sub> were found in the B<sub>4</sub>C/B fiber containing composite.

A more detailed analysis was done on the Borsic/Ti composite. In this system combined TEM and EELS analyses across the interface were performed. The SiC in the Borsic is found next to the boron and TiC at the metal interface. The Ti must have reduced the SiC to produce the TiC. The chemistry starting from the boron fiber and going away from the fiber gave boron followed by silicon and carbon, followed by titanium, carbon and silicon and then into the titanium matrix. These analyses show how complex the interfaces are and the many layers that could act as the lowest cohesive energy fracture path. The results presented here are not complete and only give an indication of how complex the interface is.

### III. Summary

Research on the influence of the interface on the mechanical properties of Ti-6Al-4V metal matrix composites (MMC) containing Borsic, SiC and B<sub>4</sub>C/B continuous fibers is reported. The potential high temperature application of the Ti MMC was the basis for thermal fatigue experiments.

The mechanical measurements included monotonic and cyclic mixed mode testing. In the testing it is found that the crack follows the matrix/fiber interface for angles from transverse loading up to about 45° and propagates normal to the fiber for higher angles

and longitudinal loading. This leads to properties that are bimodal in behavior, poor in the first case and higher in the second case. Degradation of the interfaces modified by thermal cycling has a much larger effect on the longitudinal properties. The transverse properties are dominated by the matrix properties.  $H_2O$  and  $H_2$  gaseous environments increase the room temperature fatigue crack growth rate for all the materials in all conditions tested.

An analysis of diffusion down the interface and into the matrix is described and data presented for both thermal fatigue and isothermal treatments. The interface diffusion is about  $10^5$  greater than the coupled diffusion into the matrix.

TEM, EELS and AES results show the interfaces in the Ti MMC to contain very complex chemical, crystallographic and morphological features that are modified by exposure to humidity or a sulfur bearing environment.

In addition segregation to the interface and its effect on the cohesive energy was analyzed with a non-equilibrium thermodynamics model.

#### IV. Personnel Involved in Research

##### Principal Investigator:

Harris L. Marcus

Harry L. Kent Jr. Professor of Mechanical Engineering

##### Others:

Professor John P. Stark

[served as an unpaid consultant on the thermodynamic modeling]

Michael Schmerling  
Research Associate

J. Steve Swinnea  
Research Associate

##### Graduate Students

Young Hoon Park - Thermal fatigue, Mixed mode fracture, Interface diffusion

Deepak Mahulikar - Mixed mode fracture, Fatigue crack growth

Doo Young Lee - Interface segregation

Dushyant Narayen - Environmental fatigue crack growth

Li Jiuan Fu - TEM

#### V. Dissertations

Deepak S. Mahulikar, "Effect of Environments on the Fatigue Crack Propagation Behavior of Titanium Metal Matrix Composites," December 1981; The University of Texas, Austin.

Young Hoon Park, "Influence of Interface Degradation by Environments on the Thermal and Fracture Fatigue Properties of Titanium-Continuous Fiber Composites," May 1983, The University of Texas, Austin.

##### Thesis

Dushyant Narayen, "Fracture of Titanium Metal Matrix Composite Materials," August 1983, The University of Texas, Austin.

#### VI. Publications

1. D.S. Mahulikar, Y.H. Park and H.L. Marcus, "Mixed Mode Crack Propagation in Continuous Fiber Metal Matrix Composites," Proceedings of the Greece/USA Mixed Mode Fracture Conference, Athens, Greece; Sih, G.C. and Theocaris, P.S., Editors, Sijthoff and Noordhoff, p. 385 (1981).
2. D.S. Mahulikar, Y.H. Park and H.L. Marcus, "Environmental Influences on the Fracture and Fatigue Properties of Titanium Metal Matrix Continuous Fiber Composites," in Fracture Mechanics, Fourteenth Symposium, J.C. Lewis and G. Sines, eds. ASTM-STP 791, vol. II, 1983, pp. 579-597 (Philadelphia, PA).

3. Y.H. Park and H.L. Marcus, "Influence of Interface Degradation and Environment on the Thermal and Fracture Fatigue Properties of Titanium Matrix/Continuous SiC Fiber Composites," in Mechanical Behavior of Metal-Matrix Composites, J.E. Hack and M.F. Amateau, eds., 1983, TMS-AIME:New York, pp. 65-75.
4. D.S. Mahulikar and H.L. Marcus, "Environmentally Influenced Mixed Mode Fatigue Crack Propagation of Titanium Metal Matrix Composites," Metal. Trans. 15A, 209 (1984).
5. D. Finello, Y.H. Park, M. Schmerling and H.L. Marcus, "Fractography of Metal Matrix Composites," in Fractography of Ceramic and Metal Failures, J.J. Mecholsky and S.R. Powell, eds., 1984, ASTM STP 827:Philadelphia, PA, pp. 387-396.
6. Y.H. Park, D. Narayen, M. Schmerling and H.L. Marcus, "Fatigue Crack Growth Behavior of Ti-6Al-4V Metal Matrix/Continuous SiC and B<sub>4</sub>C/B Fiber Composites," in press, J. of Materials Science, 1984.
7. D.Y. Lee, E.V. Barrera, J.P. Stark and H.L. Marcus, "The Influence of Alloying Elements on Impurity Induced Grain Boundary Embrittlement," Met. Trans. 15A, 1415 (1984).
8. Y.H. Park, D. Narayen and H.L. Marcus, "Interface Diffusion Studies in Titanium Metal Matrix/Continuous SiC and B<sub>4</sub>C/B Fiber Composites," in press, MS&E, 1984.
9. Deepak Mahulikar and H.L. Marcus, "Mixed Mode Fracture in Titanium Metal Matrix Composites," Theoretical and Applied Fracture Mechanics, 1984.

#### Talks

1. H.L. Marcus, Invited Talk, "Mixed Mode Crack Propagation in Continuous Fiber Metal Matrix Composites," Greece/USA Mixed Mode Fracture Conference, Athens, Greece, August 1980.
2. Y.H. Park, D.S. Mahulikar and H.L. Marcus, "Interfacial Degradation Due to Isothermal and Cyclic Thermal Treatment in Ti-6Al-4V Matrix Composites," 1981 Annual AIME Meeting, Chicago, February 1981.
3. D.S. Mahulikar, Y.H. Park and H.L. Marcus, "Environmental Influences on the Fracture and Fatigue Properties of Titanium Metal Matrix Continuous Fiber Composites," 14th National Symposium on Fracture Mechanics, ASTM-STP, June/July 1981, Los Angeles.
4. Y.H. Park and H.L. Marcus, "Influence of Interface Degradation and Environment on the Thermal and Fracture Fatigue Properties of Titanium Matrix/Continuous SiC Fiber Composites," 6th Failure Modes in Composites Conference, Dallas, February 1982.

5. H.L. Marcus, "The Influence of Impurity Elements on the Properties of Alloys," Joint TMS-AIME and BSD-ACS, Louisville, October 1981.
6. H.L. Marcus, Invited Talk, "Metal Matrix Composites," General Dynamics, Fort Worth, TX, January 19, 1983.
7. H.L. Marcus, Invited Talk, "Studies in Metal Matrix Composites," Aerospace Corporation, Los Angeles, December 1982.
8. Y.H. Park and H.L. Marcus, "An Interface Diffusion Study in Titanium Metal Matrix/Continuous  $B_4C/B$  Fiber Composites," AIME Annual Meeting, Atlanta, GA, March 1983.
9. H.L. Marcus, D.Y. Lee, E.V. Barrera and J.P. Stark, "The Effect of Alloying Elements on Impurity Induced Grain Boundary Embrittlement in Iron Band Alloys," TMS-AIME Fall Meeting, Philadelphia, PA, October 1983.
10. H.L. Marcus, "Interfaces and Fracture in Metal Matrix Composites, MRC-DARPA Meeting, Workshop on Fracture Toughness of Advanced Fibrous Composites, La Jolla, CA, July 19-20, 1984.
11. H.L. Marcus, "Fracture in Metal Matrix Composites," Invited Talk, Lockheed Corporation, Sunnyvale, CA, July 23, 1984.
12. H.L. Marcus, "Metallurgical Characterization of the Interface of MMC," Tri-Service Workshop on MMC, Washington, D.C. August 21-23, 1984.
13. H.L. Marcus, "The Effect of Alloying Elements on Impurity Induced G.B.E. of Fe Alloys," Invited Talk, Olin Corporation, August 20, 1984.
14. H.L. Marcus, D. Narayan and Y.H. Park, "Interface Diffusion Studies in Ti Metal Matrix/Continuous  $SiC$  and  $B_4C/B$  Fiber Composites," TMS-AIME Fall Meeting, Philadelphia, PA October 1983.

## APPENDIX A

## MIXED MODE CRACK PROPAGATION IN CONTINUOUS FIBER METAL MATRIX COMPOSITES

D. S. Mahulikar, Y. H. Park and H. L. Marcus

Department of Mechanical Engineering and Materials Science  
and Engineering, The University of Texas at Austin

## ABSTRACT

Metal Matrix Composites are characterized by heterogeneity, anisotropy and interfaces. During Mode I loading a propagating crack entering the brittle interfacial region around the fiber can experience a mixed mode loading condition if the crack grows around the fiber. The weak interfaces can significantly influence the mixed mode crack propagation behavior of the composites. It is thus essential to consider the interfaces as well as the stress state around the crack tip in order to study the mixed mode behavior of the Metal Matrix Composites. These effects are discussed in this paper on the basis of microscopic observations. A brief review of mixed mode cracking in this type of composite is also presented.

## INTRODUCTION

Continuous fiber metal matrix composites have generated a considerable amount of interest in the materials field because of their potential application in the dynamic structures. A Metal Matrix Composite system (MMC) in general consists of a high modulus reinforcement (e.g. fibers) incorporated in a compatible metal matrix. The MMC carries some distinct advantages over the resin-matrix composite system and the monolithic materials. These advantages include: high strength, high modulus, toughness and impact properties, excellent reproducibility of properties, surface durability, relatively low notch sensitivity, and low sensitivity to changes in temperature. They also exhibit better transverse properties than the resin-matrix composites. [1]

However, the MMCs are characterized by heterogeneity, anisotropy and interfaces. Due to the high temperatures involved during the fabrication of the MMCs, the fibers tend to react with the metal matrix forming interfaces and reaction zones [2]. The chemistry and thickness of these interfaces is dependent on the matrix-reinforcement properties. [2] Interfaces in

general are the weak links in the composite system. It is observed, therefore, that many of the mechanical properties, including off-axis properties, are highly interface dependent [3]. In Ti-matrix/coated boron fibers or SiC fibers MMC system, for example, a reaction zone is formed at the fiber/matrix interface during fabrication. The mechanical properties of this system are known to depend on the chemistry and the thickness of the reaction zone [4]. Because of the formation of brittle oxides and carbides at the interfaces of Ti and the fibers, these zones provide fracture initiation or propagation sites. Thus it is expected that propagation of a crack in such composites is not only the function of stress state around the crack tip, but also the nature of the fiber/matrix interface.

When loaded in tension, there are various ways in which a MMC can fail. Fracture modes of a filamentary composite in general are described in [5]. Those related to a brittle fiber/ductile matrix system apply to the MMCs. The more important ones include: fiber pull out, crack bridging, microcracks in matrix, fiber failure, interface debonding, matrix failure, etc. Since there are so many ways by which a MMC can fail, it would be difficult to have a single model which predicts its fracture behavior. In addition, the type of loading involved, and the stresses it generates at the macro as well as micro level become very important parameters. On a macro scale the loading can either be a single mode (mode I for example) or a mixed mode. For MMCs, mixed mode loading analysis is more pertinent for various reasons. Firstly, the off-axis strength of these composites is an important parameter in the design. Off-axis loading involves a mixed mode analysis assuming presence of flaws. Secondly, due to inherent anisotropy and presence of defect structures at the fiber/matrix interfaces, the flaws do not tend to propagate in a self-similar manner. Any change in direction of crack propagation will involve a mixed mode loading at the micro level around the crack tip. Finally, when a propagating flaw goes around the fiber, it experiences a mixed mode loading. These three cases are shown in Fig. 1 (a, b and c). In cases 1(a) and 1(c) mode I and II type of loading is predominant, whereas in 1(b) mode III type of loading is also present.

Many attempts at modeling the mixed mode crack propagation in fibrous composites have been made. [5-15]. First attempts included direct application of the linear elastic fracture mechanics, by considering the composite a homogeneous orthotropic linear elastic plate. For this case, in which cracks are present, and extend in a direction normal to one of the planes of symmetry, the stress fields around the crack front were simply separated into symmetric (mode I) and skew symmetric (mode II) [7,8]. The combined mode analysis consists of superposition of crack tip stresses given by symmetric and skew symmetric fields. Application of strain energy release rate criterion to combined mode



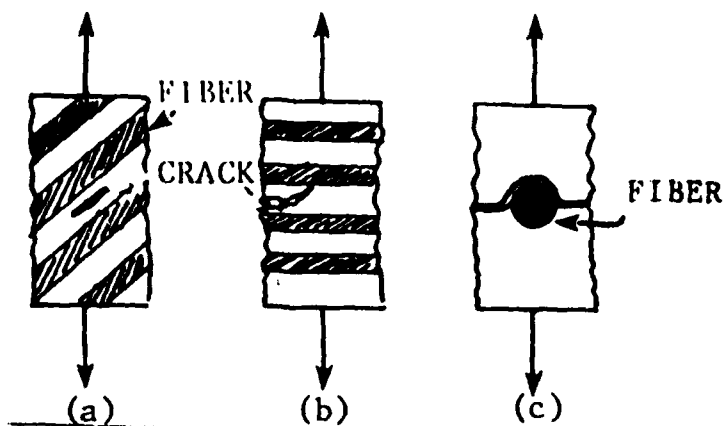


Fig. 1 : Mixed Mode Loading on  
a MMC

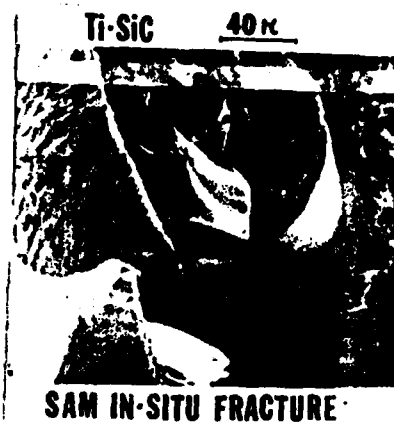


Fig. 2: SEM of the  
In-Situ  
Fractured Surface

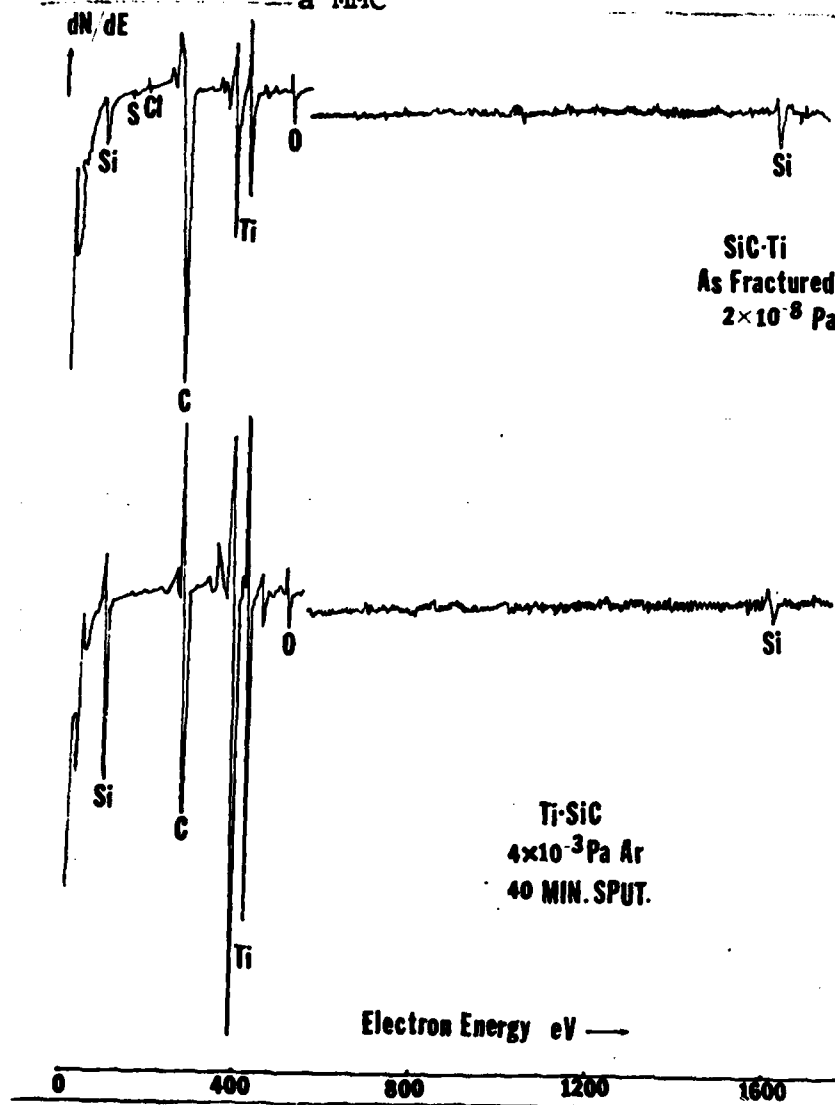


Fig. 3  
SAM Profiles for  
As-Fractured and  
As-Sputtered Specimens

loading in composites has been attempted [9,10,11] giving a combined failure criteria,

$$G_I + G_{II} = G_{\text{critical}}$$

Where  $G$  refers to the strain energy release rate and suffixes I and II denote the modes of crack extension. The theories, however, are applicable only to self similar crack growth. They also ignore the inherent heterogeneity of composite materials and the effect of interfaces.

For non-collinear crack growth several models have been proposed [12-15]. In these models the main crack is oriented parallel to the fiber direction. For the mixed mode loading Sih [13,14] introduced a strain energy density concept to determine the condition for crack extension and also its direction in unidirectionally reinforced composites. He also used an anisotropic elasticity model and a matrix crack propagation model to obtain critical fracture stresses for different angles of fiber orientation [14]. Tirosh [15] recently used energy release rate criterion to predict inner matrix path fracture and an energy momentum tensor to predict transfibral path fracture in filamentary composites. He suggests that under certain conditions of loading branching of crack from inner matrix path to transfibral path will occur. He also showed that operationally simple energy release rate criterion shows good agreement with the experimental data as well as with Sih's models.

Most of these models show excellent agreement with the experimental data at angles measured from the load axis which are greater than  $45^\circ$ , where fracture is predominantly matrix dependent. At lower angles, however, due to complex failure modes of the fibers, the models show some discrepancies. Secondly the initial crack is assumed to be parallel to fiber orientation. The analysis would be different if the initial crack was not parallel to the fibers. Finally, the presence of interfaces should make a considerable difference. Interfaces, which are usually the weak links in the MMCs, can present the least resistant paths for crack propagation. Thus the crack will prefer to propagate along the weakly bonded fibers, and not by the path predicted by the above models which neglect presence of interfaces. This problem is more important to MMCs in general and Ti-matrix composites in particular. The purpose of this paper is to verify the applicability of mechanics models to Ti-matrix unidirectional continuous fiber composites, and establish the role played by the fiber/matrix interface in the mixed mode crack propagation. Experiments were performed to obtain the critical stresses at different crack angles for Ti-matrix composites, for cracks along the fibers. In order to find the effect of initial crack orientation, experiments were done with the initial flaw perpendicular to the tensile load

and at an angle to the fibers. In order to establish the role of the interface, tensile data was obtained for thermally cycled specimens since thermal cycling is known to degrade the interfaces in MMCs [16,17]. Fractographic studies clearly indicate that interfaces play a significant role in mixed mode crack propagation of Ti-matrix composites. It is therefore suggested that in the mixed mode analysis of MMCs, both interfacial properties and the mechanics should be considered,

#### EXPERIMENTAL PROCEDURE

Experiments were performed on a Ti-6Al-4V alloy matrix/B<sub>4</sub>C-B or SiC fiber MMC system. The fibers are continuous approximately 150 $\mu$ m diameter fibers. The volume fraction of fibers in the composite is approximately 0.4. The as received material was first cut into small specimens of desired orientation (3mm x 30mm) for the Scanning Auger Electron Microscope (SAM) and 10mm x 30mm for fracture studies by an electro-discharge machine, to minimize the damage during sample preparation. The Auger samples were then cleaned and fractured 'in situ' in the SAM. A fractures surface is shown in Fig. 2. SAM studies were then carried out on the fractured surface. The Auger profiles of fractured and argon ion sputtered surfaces are shown in Fig. 3 for a select point on the matrix side of the interface. Similar studies were carried out on thermally fatigued Ti/SiC specimens.

For mixed mode loading experiments, the specimens had different fiber orientations. For the first set of experiments, the fibers were at an angle of 0, 35, 60 and 90° to the loading axis. An initial edge notch (2mm) was cut along the fiber direction. The specimens were then tested in tension on an Instron machine and the load-displacement curves were obtained till fracture. The load-displacement curve was linear up to the point of fracture. The fracture stresses were calculated and plotted against the crack angles [Fig. 4].

In the second set of tension experiments; the initial notches (2mm) were cut perpendicular to the loading axis and at an angle to the fiber orientation [0°, 30°, 45°, 60°, 90°]. These specimens were then fractured in tension and the stresses were recorded against the angles of fiber orientation with respect to the notch [Fig. 5]. Fig. 6 shows schematically the difference in the crack geometry for the two types of experiments.

In addition, tension specimens were exposed to thermal fatigue and for comparison isothermally heated at the maximum temperature for thermal cycling, before notching. The thermal fatigue specimens were cycled between 40°C and 550°C in three minute

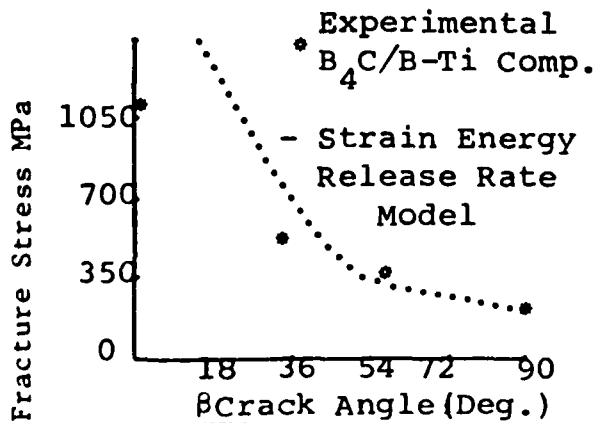


Fig. 4  
Fracture Stress vs.  
Crack Angle ( $\beta$ ).

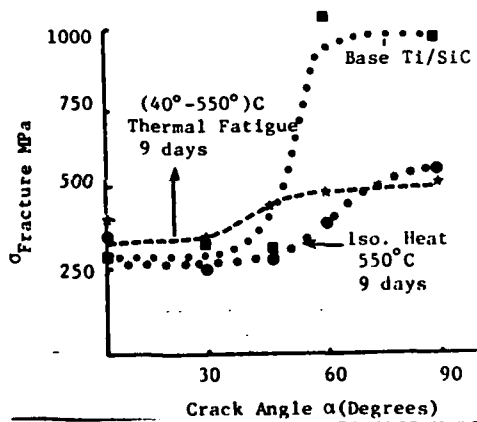


Fig. 5  
Fracture Stress vs.  
Crack Angle ( $\alpha$ )

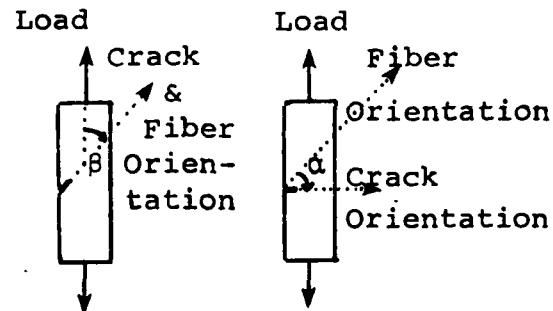


Fig. 6  
Initial Notch Orientations  
for Tension Specimens

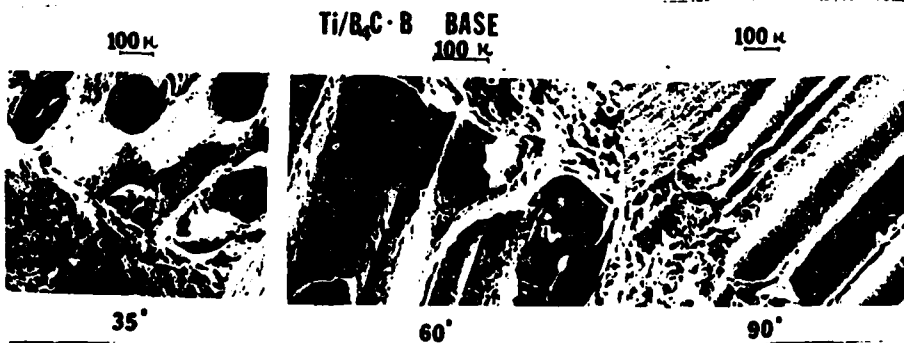


Fig. 7  
SEMs of  
Initial Notch  
Region

cycles for as long as 9 days. The isothermal aging was done at 550°C for as long as 9 days. After the specimens were notched with a 2mm deep crack perpendicular to the loading axis and fractured in tension. The fracture stresses were then plotted against the angles [Fig.5]

Fractographic studies were then carried out on all of the fractured specimens. The mixed mode crack propagation was studied with the help of SEM and optical micrography.

## RESULTS AND DISCUSSION

The SAM studies carried out on the in-situ fractured surfaces of the Ti-matrix composites, indicate that the fracture path is very close to the fiber side of the reaction zone. The surface shows presence of brittle compounds such as TiC, oxides for Ti/SiC [Fig. 3] and borides for the Ti/B<sub>4</sub>C-B. Chlorine and sulfur impurities that have segregated to the interface are also present on the fracture surface. After inert ion sputtering, the impurities and most of the oxide are removed [Fig. 3b] indicating that the preferred and probably lowest energy fracture path was on a layer containing large amounts of brittle compounds and impurities. The fracture surface [Fig. 2] shows fiber pull out and fiber breakage indicative of a weak bond at the interface. The SAM studies on the thermally fatigued Ti/SiC specimens show large amounts of oxides and almost no carbides, indicating that degradation of interfaces has resulted in oxide formation.

For the first set of mixed mode tension experiments, where the initial crack was cut parallel to the fibers, the results indicate that the fracture stress continuously decreases as the crack angle  $\beta$  increases [Fig. 4]. The fracture stress decreases sharply as  $\beta$  varies from 0° to 45°. Fractographic studies [Fig.7] show that except for 0° and 35° ( $\beta=0^\circ$  does not have a precrack in it) crack angle, the crack propagates along the interface self-similarly. For the 0° and 35° crack angles both fiber fracture and interface failure are observed.

The experimental data is compared to a simple energy release rate model [15]. It's observed that the data fits the model only for crack angles above 45° when the fracture path is predominantly in the matrix and interface. At lower angles, however, additional failure modes are observed which are not taken into account by the models and the correlation no longer exists [Fig. 4].

A very important factor influencing the fracture path is the interfacial region. If the crack is aligned along the fiber direction it follows the interfacial self-similar path for  $\beta$  greater than 45°. This, however, does not establish the

role of the interface in crack propagation. On the other hand, if the crack were aligned at an angle  $\alpha$  to the fiber orientation, it will propagate along a path influenced by the mechanics as well as the material properties of the interface. Fig. 6 shows this loading geometry. Hence in the second set of experiments the initial notch was cut perpendicular to the load axis and at an angle ( $\alpha$ ) to the fiber orientation. The specimens were then tensile tested till fracture and the fracture stresses were plotted against the angle [Fig. 5] which now is the angle between the initial crack orientation and the fiber orientation. The sigmoidal shaped curve shows sharp decline of fracture between  $60^\circ$  and  $45^\circ$ . Below  $45^\circ$ , the curve levels off. Fractographic studies on the specimens show some interesting characteristics. [Fig. 8 and 9]. For  $0^\circ$  and  $30^\circ$  angles the crack propagation is along the fiber direction [Fig. 8]. At  $45^\circ$  angle the crack shows an interfacial as well as transfibral fracture. [Fig. 8]. Interfacial splitting is combined with transfibral crack propagation for an average crack propagation direction corresponding to  $\alpha=30^\circ$  [Fig. 8]. Thus it seemed that for Ti-matrix/SiC composites the mixed mode crack propagation was influenced by interfaces as well as the stress state resulting in a crack with large regions of interface fracture but with a common average angle of fracture.

If the interface influences the crack propagation, then that effect will be more dominant if the interface was further degraded. Thus in the third set of experiments the Ti-/SiC specimens were thermally fatigued for 9 days between  $40^\circ\text{C}$  to  $550^\circ\text{C}$  with a cycle of 3 min. Another set of specimens were isothermally heated at  $550^\circ\text{C}$  for 9 days. All the specimens were notched following the thermal treatment with the notch normal to the loading direction and then tension tested until fracture. The data is presented in Fig. 5 along with the base composite data tested under identical conditions.

It can be noticed that the sigmoidal curves for both types of thermal treatments, the change in fracture stress with an angle is much less than the base composite curves. The angle at which there is a transition in the fracture stress shows a shift from that in the baseline data. A considerable drop in the longitudinal strength is observed, which indicates that fibers have been degraded by thermal cycling and continuous heating. However, no significant changes in fracture stress at lower angles were noticed. This suggests that the transverse strength has remained the same despite thermal cycling and continuous heating. This observation may be due to the fact that the transverse properties are titanium matrix dependent; and the transverse strength really represents the intrinsic matrix toughness. A calculation of transverse strength, considering a hexagonal array of holes in Ti-6Al-4V matrix, for a fiber volume fraction of 0.40, gives a stress concentration of approximately 4 [16]. This gives a transverse strength of approximately



Fig. 8  
Optical Micrographs of  
the Fractured Surface

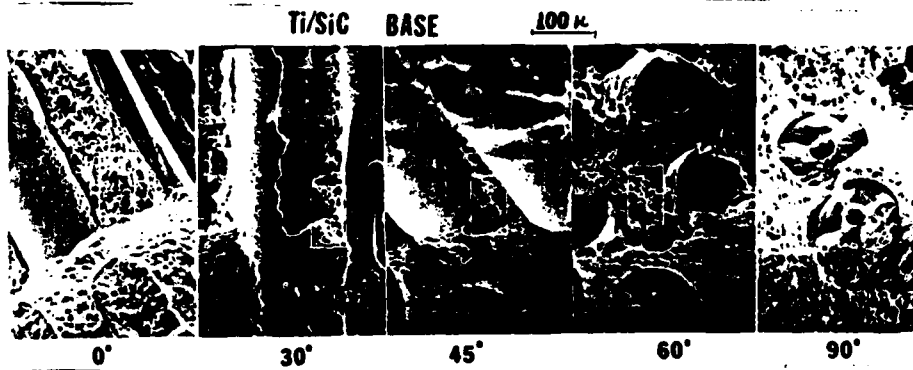


Fig. 9  
SEMs of  
Initial Notch  
Region

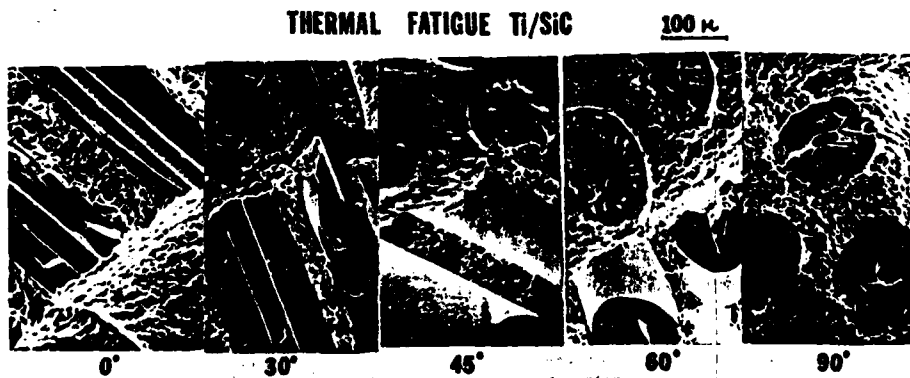


Fig. 10(a)  
SEMs of  
Initial  
Notch  
Region



Fig. 10(b)  
Optical Micrographs  
of the Fractured Surface

245 MPa for Ti-6Al-4V matrix with hexagonal array of cylindrical holes in it. This simple calculation may explain why the transverse strengths obtained for base composite and thermally degraded composites are around 280 MPa. However, more experiments are needed to confirm this observation.

Stereographic observations, however, show distinct differences in the modes of fracture of as received Ti/SiC and interface degraded composites above 45° crack angle [Fig. 9,10,11]. While for as received metal, transfibral fracture was observed at 45° and 60° angles, the predominant mode of fracture for the thermally fatigued and continuously heated samples appears to be interfacial failure. The crack doesn't seem to propagate at a preferred angle which was the case for two base composites. Excessive fiber damage is noticed on the interface degraded specimens. At all the angles some crazing is also noticed at the interface [Fig. 12]. However, above 45°, the initial crack propagation seems to be predominantly interfacial in thermally degraded composites. [Fig.10,11]. This, added to the fact that severe fiber damage has occurred, explains the sharp drop in fracture stresses for the thermally degraded composites. The formation and growth of brittle carbides, oxides and borides at the interfaces can serve as the source of fiber degradation.

Thus interfaces seem to play an important role in the mixed mode crack propagation of the Ti matrix composites. The fracture mode is controlled by both the mechanics and the interface. In order to model the mixed mode fracture behavior of the MMCs, it is essential to incorporate interfacial properties as one of the more important parameters.

#### SUMMARY

1. Ti-matrix composites specimens with different fiber orientations were tested in tension for notches oriented along the fiber direction and normal to the load axis at an angle to the fiber direction, for as received, thermally fatigued and isothermally heated samples.
2. For Ti/B<sub>4</sub>C-B composites fracture stress decreased with increasing crack angle  $\beta$ . However, the theoretical strain energy release rate mode only agrees with the data for angles greater than 45°.
3. The Ti-matrix/SiC specimens notched at an angle to the fiber direction showed a sharp drop in fracture stress for angles between 45° and 60°.
4. Thermally fatigued and isothermally heated Ti/SiC specimens showed a considerably lower fracture stress at higher angles and minimal change in fracture stress at lower angles.



5. The drop in strength at high angles is attributed to fiber and interface degradation while no change at lower angles may be due to the intrinsic toughness of the matrix.
6. Interfaces play an important role in mixed mode crack propagation and should be considered as a parameter in future mechanics analysis of the fiber reinforced composites.

#### ACKNOWLEDGEMENTS

This research was sponsored by U.S. Air Force Office of Scientific Research through grant No. 80-0052. We want to thank the Air Force Materials Laboratory for supplying the Ti composites, Drs. M. Schmerling and A. Rosen for discussion and N. Williams for his assistance in the experimental work.

#### REFERENCES

- [1] Kreider, K.G., "Introduction to Metal Matrix Composites," Composite materials, v. 4, Academic Press, pp. 1-34 (1974)
- [2] Metcalfe, A.G., "Introduction and Review," Composite Materials, v. 1, Academic Press, pp. 1-28 (1974)
- [3] Composite Materials, v. 1, "Interfaces in Metal Matrix Composites," ed. A.G. Metcalfe, Academic Press, (1974)
- [4] Metcalfe, A.G., 'Fiber Reinforced Ti Alloys,' Composite Materials, v. 4, Academic Press, pp. 269-318, (1974)
- [5] Dharan, D.K.H., J. Engineering Mat. & Techn., V. 100, pp. 233-247 (1978)
- [6] Corten, H.T., "Fracture Mechanics of Composites," Fracture V.VII, Academic Press, pp. 675-769, (1972)
- [7] Sih G. C., Paris P.C. and Irwin G.R., Int. J. Fract. Mech., v. 1 (3), pp. 189-203 (1965)
- [8] Wu E.M., Trans ASME, Ser. E. I. Applied Mechanics 34 (4) pp. 967-974 (1967)
- [9] K. Lauraitis, "Tensile Strength of Off-Axis Unidirectional Composites," University of Illinois, TAM Report No. 344 (1971)
- [10] K. Lauraitis, "Failure Modes and Strength of Angle Ply Laminates," University of Illinois TAM Report No. 345 (1971)
- [11] Wu E.m., Reuter R.C. "Crack Extension in Fiber Glass Reinforced Plastics", University of Illinois TAM Report No. 475, (1965)
- [12] Wu, E.M., "Strength and Fracture of Composites," in Composite Maters, V. 5, ed. I.J. Broutman, Academic Press, pp. 191-247 (1974)
- [13] Sih G.C., and Chen E.P., J. Comp Mat. V.7, pp. 230-244, (1973)
- [14] Sih G.C., Chen E.P. Huang S.L. and McQuillen, E.J., J. Composite Mat. v. 9, pp. 167,186 (1975)

- [15] Tirosh, J., Eng. Fract. Mech, V. 13, pp. 119-127 (1980)
- [16] Olsen, G. C. and Tompkins, S.S., "Continuous and Cyclic Thermal Exposure Induced Degradation in Boron Reinforced 6061 Aluminum Composites," in Failure Modes in Composites IV, J.A. Cornie (ed.), pp. 1-21, AIME (1979).
- [17] Grimes, H. H., Lad, R. A. and Maisel, J.E., Metall, Trans. A, 8A, pp. 1999-2005. (1977)
- [18] Riggs, D., "Prediction of the Transverse Strength of Aluminum/Graphite Composites," Army Materials and Mechanics Research Center Report, (1979)

### Ti-SiC ISOTHERMAL HEATING

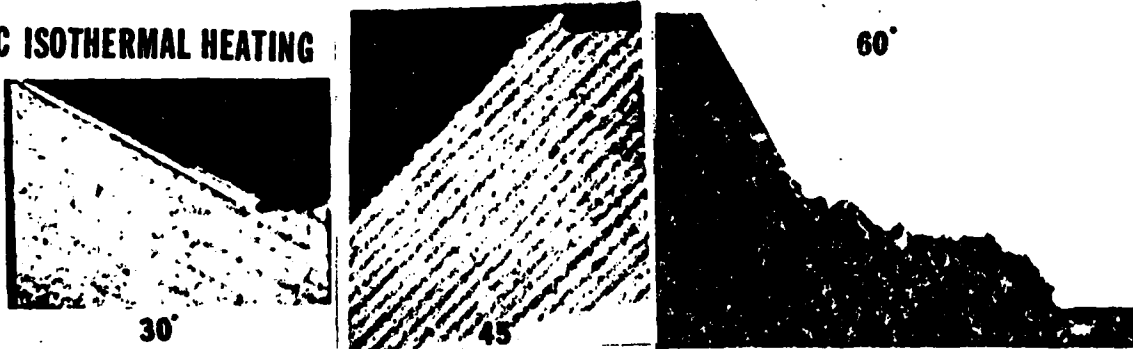


Fig. 11(a)

Optical Micrographs of the Fractured Specimen

### ISOTHERMAL HEATING Ti/SiC 100μ



Fig. 11(b)  
SEMs of the  
Initial  
Notch  
Region

### Ti-SiC INTERFACE 10μ

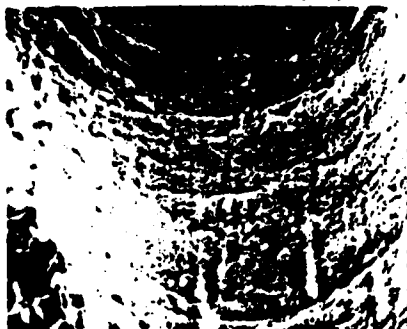


Fig. 12

SEM of the Fractured Interface Showing  
Some Crazing

### THERMAL FATIGUE

## APPENDIX B

### MIXED MODE FRACTURE IN TITANIUM METAL MATRIX COMPOSITES

Deepak MAHULIKAR \* and H.L. MARCUS

*Materials Science and Engineering, The University of Texas, Austin, Texas 78712, USA*

#### Introduction

The problem of mixed mode fracture in the isotropic as well as anisotropic materials has been receiving a considerable amount of interest lately [1-7]. The importance of studying the mixed mode fracture behavior for metal matrix composites [MMCs] has been recognized for a long time [8-13]. Due to the high degree of anisotropy and the presence of defect structures at the fiber/matrix interface, flaws do not tend to propagate in a controlled manner. Any change in the crack growth direction involves a mixed mode loading locally at the crack tip. Mixed mode loading is also experienced when a propagating flaw goes around a fiber. Study of the mixed mode fracture behavior for the MMCs, unlike isotropic materials, presents several problems. The MMCs are characterized by heterogeneity, anisotropy and interfaces. These factors can substantially influence the mixed mode behavior of the MMCs.

The purpose of this paper is to identify some of the problem areas in the studies of mixed mode fracture and fatigue crack propagation (FCP) of the MMCs and to report on some experimental results obtained. The evaluation is based on the work on continuous fiber reinforced titanium metal matrix composites [5-7]. Some of the areas to be considered are the application of fracture mechanics, presentation of FCP data, influence of fibers and interfaces, and the influence of various environments on the FCP.

#### Mixed mode static loading

The mechanics approach for mixed mode loading is based on either a) the crack propagation is

self-similar [12-3] or b) the crack extension is non-collinear [2,11]. Further assumption of orthotropic linear elastic plate is essential [8] for a composite material. Thus for self-similar crack propagation under mode I and II loading the failure criterion can be given by [8]:

$$G_c = G_I + G_{II} \\ = (S_{11} + S_{22}/2)^{1/2} [(S_{22}/S_{11})^{1/2} + 2S_{12} \\ + S_{66}/2S_{11}]^{1/2} [K_I^2 + (S_{11}/S_{22})^{1/2} K_{II}^2].$$

It was observed [10,14] in plexiglass, aluminum alloys and resin matrix composites that for mixed mode loading the crack does not necessarily extend in a self-similar way. Many approaches were proposed to analyze this problem [3,14-18]. Among those models, the *S* theory [16-18] states that the mixed mode crack extension will occur at a certain angle  $\theta$  decided by the strain energy density field around the crack tip. The model can be used effectively for the composite materials also.

Several problems are encountered when applying these models to a MMC. The crack propagation in MMCs is a complex process involving several failure mechanisms acting simultaneously [4]. Also one of the most important factors influencing the fracture mode is the fiber-matrix interface, which can provide an anisotropic least resistant path for crack growth during the mixed mode loading. In order to study the interface effect, tension testing was carried out on center notched off-axis as received as well as heat treated specimens [7]. The fiber orientations  $\theta$  with respect to the load axis were 0°, 35°, 60° and 90°. The notch was cut along the fiber direction. The fracture stresses are plotted in Fig. 1 against the fiber angle  $\theta$  for the as received condition. The data for the heat treated B<sub>4</sub>C-B as well as BORSIC/Ti-6Al-4V specimens is recorded in Table 1 and 2.

\* Presently at Olin Metals Research Laboratory, New Haven, CT 46511

The data in Fig. 1 is compared to calculated *S* theory and a simple strain energy model [7]. It was observed that above  $\theta = 45^\circ$ , the failure was along the fiber orientation and *not* at an angle as predicted by the *S*-theory.

From Fig. 1 it can be seen that the *S*-theory and strain energy release rate model agree with the data only for the higher values of  $\theta$ , i.e., above  $45^\circ$ . The reason for this is that above  $45^\circ$  fiber orientation the fracture is predominantly matrix and interface controlled. At lower angles however the fracture involves complex model of failure, such as fiber fracture, pullout etc. This fact is not taken into account by the models.

Table 1 lists the fracture strength data for the various heat treated  $B_4C-B/Ti-6Al-4V$  specimens, and compares it to the as received condition. It is evident from Table 1 that the heat treatments resulted in the reduction of the longitudinal strength while little change in the transverse strength is observed. The reduction in longitudinal strength is nominal for the  $500^\circ C$  vacuum heat treatment. But a substantial reduction in longitu-

Table 1

Fracture strength comparison for  $B_4C-B/Ti-6Al-4V$  as received and heat treated specimens

$\theta$	As received	7 Day in Vacuum	$500^\circ C$ in Air	6 hr. $885^\circ C$ in Vacuum
Deg.	MPa	MPa	MPa	MPa
0	1035	920	780	770
45	470	460	400	388
90	345	361	355	340

Table 2

Fracture strength data for  $BORSIC/Ti-6Al-4V$  as received and  $885^\circ C$  heat treatment

$\theta$	As received	6 hr. $885^\circ C$ Vacuum
Deg.	MPa	MPa
0	820	690
45	410	400
90	350	355

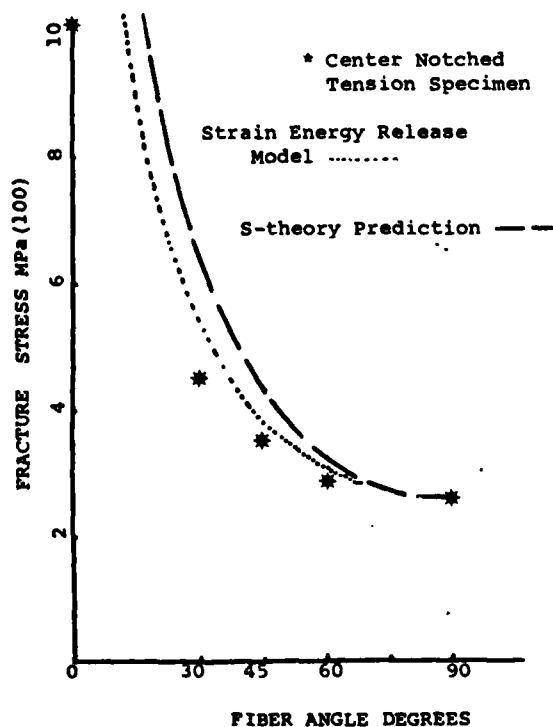


Fig. 1. The fracture strength variation of the as received  $B_4C-B/Ti-6Al-4V$  specimens versus the fiber angle  $\theta$ .

dinal strength is observed for the 7 day  $500^\circ C$  in air and the 6 hr  $885^\circ C$  vacuum heat treatment. Similar results are shown in Table 2 for  $BORSIC/Ti-6Al-4V$  composites. This suggests that these heat treatments resulted in interface modifications and fiber degradation which in turn showed a loss in longitudinal fracture strength. SAM studies [6] were therefore carried out to characterize the change in interface chemistry due to the heat treatments. These studies revealed formation of an oxide layer at the interface for the 7 day  $500^\circ C$  air heat treatment and a thick  $TiB_2$  layer for the  $885^\circ C$  6 hour vacuum heat treatment [6]. The reduction in longitudinal strength of the titanium MMCs was therefore attributed to the formation of the oxide layer in case of the  $500^\circ C$  air heat treated specimen and to the formation of  $TiB_2$  layer  $885^\circ C$  vacuum heat treatment. The interface modifications thus affected the mixed mode fracture behavior significantly.

#### Mixed mode FCP in laboratory air

The problems encountered in applying mechanics concepts to mixed mode behavior of titanium MMCs are further complicated in the mixed mode FCP studies. In order to derive useful data, a

proper  $K$ -calibration and a way to express the data is needed. The crack growth data obtained in the form of  $a$  against  $N$  can be either expressed as

$$da/dN \propto \Delta G^m,$$

if the FCP is self-similar, or

$$da/dN \propto gDS^m,$$

if the FCP is non-self-similar [16], provided a proper  $K$ -calibration for anisotropic materials is available. It was observed [6,7] that the mixed mode FCP with the initial notch parallel to the fiber orientation was self-similar. The fiber orientation was the weakest path for the FCP. This was confirmed by a couple of experiments [6]. In the first experiment, a  $45^\circ$  orientation compact tension specimen was fatigue tested. Here the initial notch was transverse to the load axis at  $45^\circ$  angle to the fiber direction. The FCP was along the fiber direction (Fig. 2a). The second experiment was

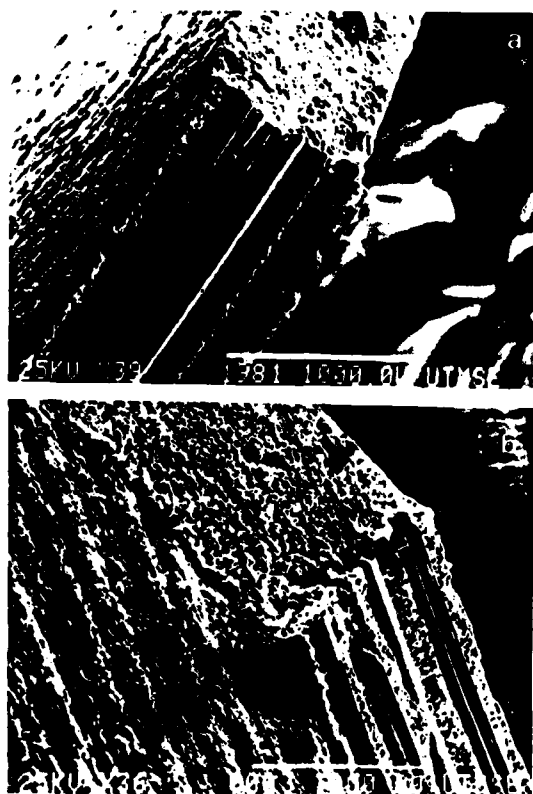


Fig. 2. (a) FCP for the  $\theta = 45^\circ$  B<sub>4</sub>C-B/Ti-6Al-4V specimen with initial notch transverse to the load axis. (b) FCP for the transverse specimen with initial notch at an angle to the fibers.

done on a transverse edge notched specimen with the notch cut at an angle to the fiber direction. Here also the FCP was along the fiber direction (Fig. 2b). This confirms the fact that the fiber direction was the least resistant path for the transverse and mixed mode FCP. Since the mixed mode specimens have their notches cut along the fiber direction, the FCP observed was self-similar, unlike that predicted by the  $S$ -theory [16]. Even for a  $\theta = 30^\circ$  mixed mode specimen, which had shown a non-self-similar crack growth during the tension testing [7], the FCP was self-similar. This fact enabled the monitoring of the FCP in the fiber direction. Because of the self-similar crack growth, the concept of the strain energy release rate was used to describe the mixed mode FCP of these composites. It should be noted, at this point, that the  $K$ -calibration used for the mixed mode composite specimens was that for the isotropic materials [17]. The composite materials are highly anisotropic and therefore it is expected that their fracture toughness would also be orientation dependent just like the modulus. The reason for this is the difference in the failure mechanisms for different orientations. For example, in longitudinal orientation, fiber fracture is a dominant failure mechanism which contributes to the strain energy release rate. In the transverse direction, however, matrix and interface failure contribute to the fracture toughness. Thus the fracture toughness for the MMCs is essentially an orientation dependent quantity. This presents some problems for the  $K$ -calibration of the composites. However, it was observed [18] that for the longitudinal orientation, the  $K$ -calibration curves obtained from global compliance measurements on aluminum/boron and BORSIC/titanium composites were the same as the isotropic materials. It was found that the local as well as the global compliances were predictable by using isotropic  $K$ -calibration. This is an important observation, since  $K$ -calibration for the longitudinal composite specimens can then be obtained from the isotropic materials. For mixed mode specimens, however, strain energy release rate approach was chosen.  $K$ -calibrations for the isotropic materials were used and were normalized by proper modulus value to obtain

$$(G = G_I + G_{II} \text{ where } G_I = K_I^2/E_I \text{ and } G_{II} = K_{II}^2/E_{II}).$$

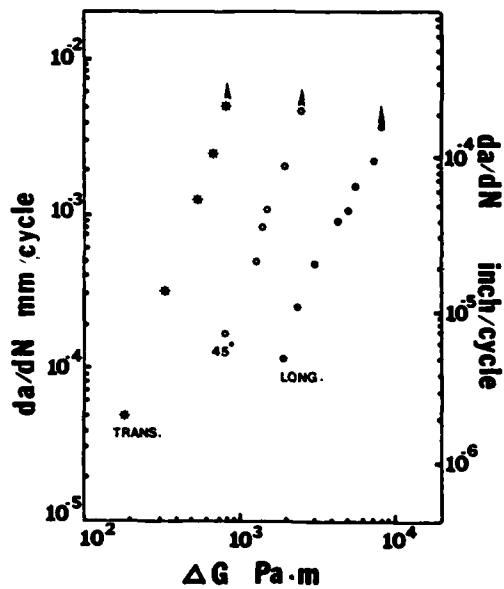


Fig. 3. Mixed mode FCP rates for the as received  $B_3C-B/Ti-6Al-4V$  composite in humid air.  $R = 0.1$ .

Thus in the absence of a rigorous  $K$ -calibration for the mixed mode specimens, use of the orientation dependent modulus to normalize the strain energy release rates was preferred.

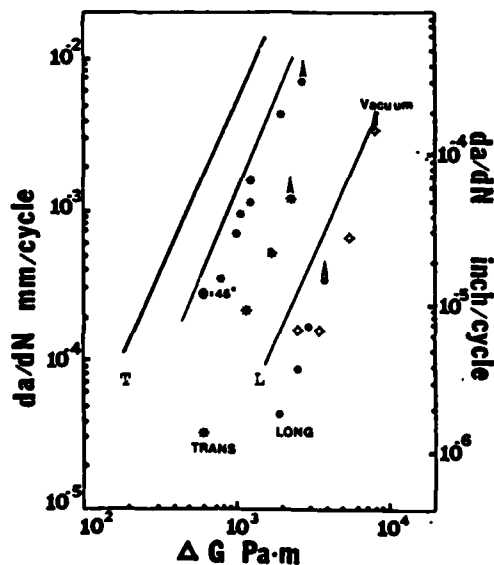


Fig. 4. (a) Mixed mode FCP for the 7 day  $500^\circ C$  heat treated  $B_3C-B/Ti-6Al-4V$  specimens in humid air at  $R = 0.1$ .  $\circ$  represents vacuum heat treatment. Full lines show the data for the as received specimens.

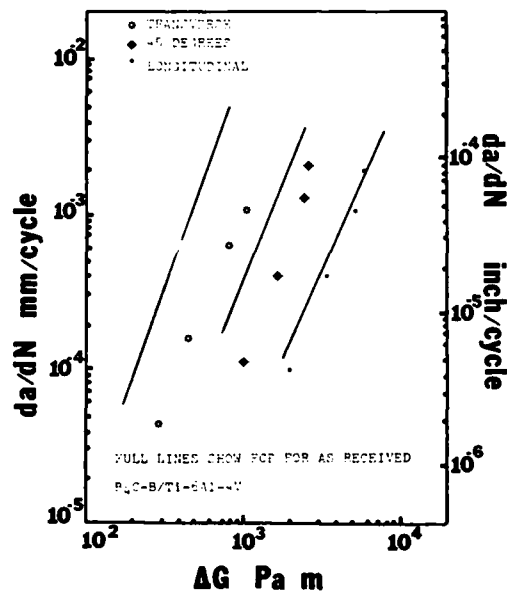


Fig. 4. (b) Mixed mode FCP for the  $885^\circ C$ , 6 hour, vacuum heat treated  $B_3C-B/Ti-6Al-4V$  specimens in humid air at  $R = 0.1$ .

Figure 3 shows the FCP data for the as received  $B_3C-B/Ti-6Al-4V$  specimens for the 0, 45 and 90 degrees fiber orientation [6]. It is evident from Fig. 3 that the as received composite's mixed mode FCP behavior can be expressed by the equation

$$da/dN \propto \Delta G^m, \quad m = 3 \quad \text{for a particular } \theta.$$

It is interesting to note that the slope  $m$  for all the curves is similar. As expected the curves represent the anisotropy of the composite, with the longitudinal specimen showing relatively slower FCP rate and a significantly higher value of the failure strain energy release rate ( $G_F$ ).

FCP curves for the heat treated  $B_3C-B/Ti-6Al-4V$  specimens are plotted in Fig. 4a and 4b. In general the heat treatments seemed to slow down the FCP rates. This slowing down effect was much more pronounced for the transverse specimens than the longitudinal ones. This was seen for the 7 day  $500^\circ C$  air and  $885^\circ C$  6 hour vacuum heat treatment (Fig. 4a and b). The slowing down of the FCP was also noticed for the vacuum,  $500^\circ C$  heat treated longitudinal specimens. The heat treated longitudinal specimens also recorded a lower value of  $K_{failure}$  than the as received longitudinal specimens. The  $K_{failure}$  for the other orientations changed only slightly. Fractography on the

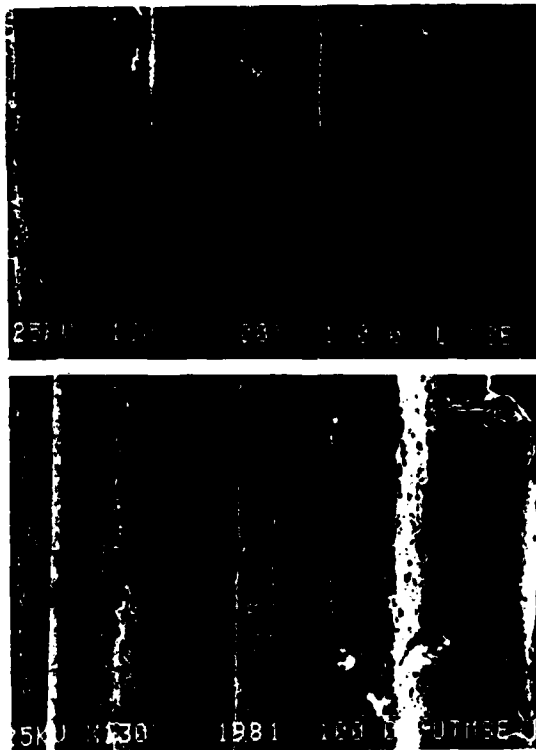


Fig. 5. (a) Mixed mode FCP in humid air for the as received  $B_4C-B/Ti-6Al-4V$  transverse (top) and  $\theta = 45^\circ$  (bottom) specimens.

longitudinal heat treated specimens showed fiber debonding and pull out [6]. Post pull out wear marks were noticed around the interfacial regions. Secondary cracking was observed near the main crack front of the heat treated specimens [7]. This secondary cracking and the debonding at the interface may be partly responsible for the slowing down of the FCP rates in the longitudinal specimens. The difference in the FCP rates of the as

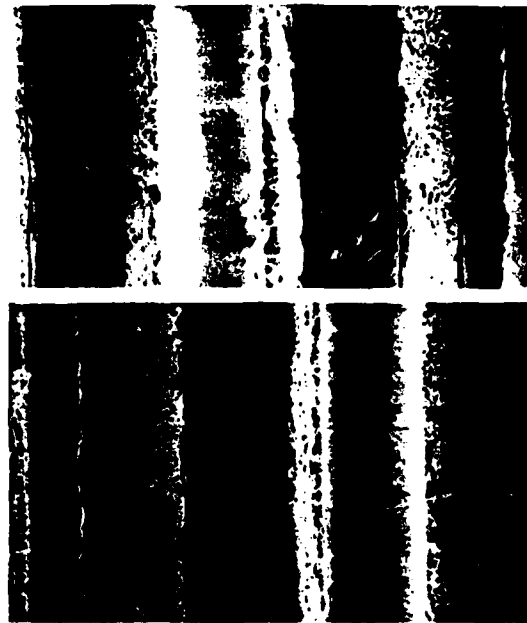


Fig. 5. (b) Mixed mode FCP for the 7 days 500°C air heat treated  $B_4C-B/Ti-6Al-4V$  transverse (top).

received and the heat treated specimens was significantly higher for the transverse and the  $45^\circ$  fiber direction specimens. Fatigue fractured surfaces at  $R = 0.1$  for those orientations are shown in Fig. 5. It is evident that for the as received condition the FCP in humid air at  $R = 0.1$  was by splitting the fibers to the core. In heat treated conditions, however, (Fig. 5b), the FCP was by interfacial splitting. No fiber splitting was seen. The  $\theta = 45^\circ$  specimens (heat treated condition) showed mode II cracking of fibers at distinct points (Fig. 5c). This change in failure mechanism from fiber splitting for the as received MMC to the interfacial splitting for the heat treated condi-

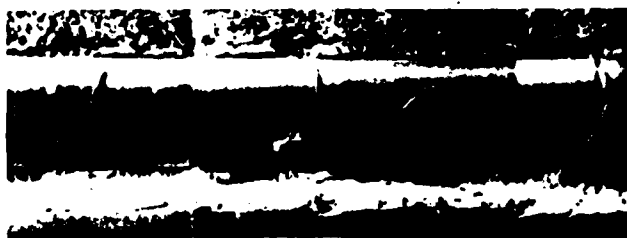


Fig. 5. (c) Fractured surface of the 7 day 500°C, air heat treated  $\theta = 45^\circ$  specimen for the mixed mode FCP, showing mode II cracking of the fibers.

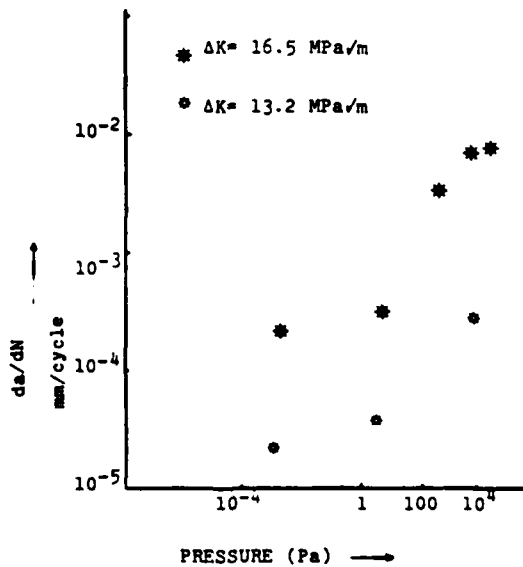


Fig. 6. Variation of the FCP rates for the BORSIC/Ti-6Al-4V transverse specimens with respect to the water vapor pressure at  $R = 0.1$  and constant  $\Delta K$ .

tion at  $R = 0.1$  is further discussed in the following section. These observations do point out that the mixed mode behavior of MMCs is strongly influenced by mechanical, metallurgical as well as environmental parameters.

#### Environmental influences: Effect of humid air and crack closure

The titanium MMC system with boron fiber reinforcement presents a unique system for studying environmental effects on its FCP. Although

the matrix Ti-6Al-4V is not sensitive to humid air embrittlement [21], it is expected that the brittle boron fiber, like many other ceramics, will get embrittled. Studies on Al-B composites [22] have shown that an increase in FCP rates results when humid air is introduced in the vacuum chamber. This effect was attributed to the weakening of boron fibers due to humidity.

Effect of humidity on mixed mode FCP rates was studied on titanium MMCs [7] by testing in environments of different relative humidities. It was observed that the FCP rates for dry environments (e.g., vacuum,  $N_2$  gas) were considerably slower than in humid air [7]. The effect was much more pronounced for the  $\theta = 45^\circ$  and  $90^\circ$  specimens where a FCP rate enhancement of up to 20 times was observed in humid air, at  $R = 0.1$ . Fractography showed that in humid air the mixed mode FCP was by fiber splitting while that in dry atmospheres was by interfacial splitting. This is surprising because one would expect that the interface will be weakened by the humid air preferentially. Further studies were carried out to investigate the water vapor pressure effect on FCP. Transverse BORSIC/Ti-6Al-4V specimens were tested. The crack was propagated at constant  $\Delta K$  and  $R = 0.1$  in a certain environment, and the loading was stopped. Another environment (e.g., humid air) was then leaked into the vacuum chamber of FCP was continued at the same  $\Delta K$  and  $R = 0.1$ . The results (Fig. 6) show that there is a steep rise in FCP rate at around 100 Pa water vapor pressure. Fractography at that point is shown in Fig. 7. It is clear that a transition from interfacial splitting to fiber splitting is visible at 100 Pa water vapor pressure. Since there is a steep rise in the FCP rate at this point, the fiber split



Fig. 7. Fatigue fractured surface of the transverse BORSIC/Ti-6Al-4V specimen showing the transition in failure modes. Interfacial splitting in vacuum to about 50% fiber splitting in 133 Pa water vapor pressure.



observed in humid air at  $R = 0.1$  can be linked to the increased FCP rate in humid air at  $R = 0.1$ .

It may be noted that all the above study was done at  $R = 0.1$  where fatigue crack closure is observed in isotropic materials. A brittle fiber reinforced ductile matrix system offers a unique characteristic for studying the fatigue crack closure. Fatigue crack closure is a result of plastic deformation left at the wake of the crack tip. In a composite system described above, only the matrix can deform plastically, not the fibers. Therefore, during the lower part of the tension to tension cycle, the deformed matrix can squeeze onto the fibers, setting up stress fields. For very thin specimens (approximately plane stress state), such as ones used in previous work [6,7], mode III type stresses can also be expected due to the specimen alignment problems. Thus it was proposed [7] that the fiber splitting observed in humid air at  $R = 0.1$  can be a result of an environmentally induced fatigue crack closure effect. Mixed mode FCP studies carried out at  $R = 0.5$  in humid air, showed that the FCP was by interfacial splitting [7] and thus supported the above-mentioned argument. However, the question of effect of humid air on fatigue crack closure remained unanswered. Fatigue crack closure measurements were therefore made in humid air and in dry  $N_2$  gas at  $R = 0.1$  and  $R = 0.5$ . The details are given elsewhere [7]. The results showed that the closure loads were higher in humid air than in dry  $N_2$  gas at  $R = 0.1$ . This may be due to an oxide formation mechanism [23]. In humid air an oxide scale develops on the crack surfaces which can preferentially strengthen the asperities. This results in increased closure loads in the plane stress region. Thus it was proposed [7] that the fiber splitting mechanism observed for the mixed mode FCP of the titanium MMCs is as a result of an environmentally induced fatigue crack closure. The squeezing effect during closure, mode III stresses along the humid air embrittlement of the boron fibers result in fiber splitting in the plastic zone ahead of the crack tip. The cracking of a substantial length of the fiber in the elongated plastic zone ahead of the crack tip results in enhanced mixed mode FCP rates in humid air at  $R = 0.1$ .

## Summary

The studies show that the mixed mode fracture and FCP behavior of MMCs is a complex phenomenon strongly affected by mechanical, metallurgical and environmental parameters. Any mechanics model should be used cautiously since interfaces, environments and stresses set up by mechanical constraints of a test affect the mixed mode fracture behavior significantly. Problems persist in the areas of K-calibration, representation of FCP data, and environmental interactions.

## Acknowledgment

This research was sponsored by AFOSR grant number 80-0052. The material was supplied by the AFML.

## References

- [1] *Proc. U.S.-Greece Symposium on Mixed Mode Fracture*, Athens, Greece, 1980.
- [2] G. Sih, *Int. J. Fract.* 10, p. 305 (1974).
- [3] J. Tirosh, *Eng. Fract. Mech.* 13, p. 119 (1980).
- [4] C. Dharan, *J. Eng. Mat. and Tech.* 100, p. 233 (1978).
- [5] D. Mahulikar, Y.H. Park and H.L. Marcus, in: *Proc. U.S.-Greece Symposium on Mixed Mode Fracture*, Athens, Greece, 1980.
- [6] D. Mahulikar, Y.H. Park and H.L. Marcus, in: *Proc. 14th National Symposium on Fracture Mechanics*, UCLA, 1981, ASTM STP.
- [7] Mahulikar, Deepak, Ph.D. Dissertation, The University of Texas at Austin, Austin, Texas (1981).
- [8] P. Paris and G. Sih, *ASTM STP* 381, p. 30 (1965).
- [9] E. Wu, *J. Applied Mech.* 34, p. 967 (1967).
- [10] E. Wu in *Composite Materials*, v. 5, Academic Press, p. 191 (1974).
- [11] G. Sih and E. Chen, *J. Comp. Mat.* 7, p. 230 (1973).
- [12] K. Lauraitis, University of Illinois, TAM Report 344 (1971).
- [13] E. Wu and R. Reuter, University of Illinois, TAM Report 275 (1965).
- [14] F. Erdogan and G. Sih, *J. Basic Eng.* 85, p. 519 (1963).
- [15] J. William and P. Ewing, *Int. J. of Fract. Mech.* 8, p. 441 (1972).
- [16] G. Sih, *Eng. Fract. Mech.* 5, no. 2, p. 365 (1973).
- [17] D. Rooke and J. Cartwright, *Compendium of Stress Intensity Factors*, The Hillingdon Press (1976).
- [18] J. Awerbuch and H. Hahn, *J. Composite Matls.* 12, p. 222 (1978).
- [19] G. Sih, in: *Methods, Analysis and Solution of Crack Problems*, vol. 1, Noordhoff Int. Publ., p. 21 (1973).
- [20] G. Sih, *Int. J. of Fract.* 10, p. 305 (1974).

*D. Mahulikar, H.L. Marcus / Mixed mode fracture in titanium metal matrix composites*

- [21] J. Chesnutt, A. Thompson and J. Williams, AFML-TR-78-68 (1978).
- [22] H. Smith and P. Shahinian, in: *Corrosion Fatigue*, Proc. Conf. by NACE, p. 499 (1972).
- [23] D. Mahulikar and H.L. Marcus, *Fatigue of Eng. Mat. and Structures* 3, p. 257 (1981).

ENVIRONMENTAL INFLUENCES ON THE FRACTURE AND  
FATIGUE PROPERTIES OF TITANIUM METAL MATRIX  
CONTINUOUS FIBER COMPOSITES

Deepak S. Mahulikar\*, Y.H. Park and H.L. Marcus  
Department of Mechanical/Materials Science Engineering  
The University of Texas  
Austin, Texas 78712

Abstract

Mixed mode tensile and fatigue crack propagation studies were carried out on  $B_4C/B$  fiber reinforced Ti-6Al-4V matrix composites for the as-received, vacuum heat-treated and air heat treated conditions. The vacuum heat treatment had minimal effect on the tensile properties of the composite but improved the fatigue crack propagation properties. The air heat treatment degraded the fibers and the interface resulting in loss of longitudinal strength, but improvement of fatigue crack propagation properties. The fatigue crack propagations for the mixed mode  $30^\circ$ ,  $45^\circ$ , and transverse specimens was self-similar. The as-received composites' mixed mode propagation is given by  $(da/dN) \propto (\Delta G/G_f)^m$  for all the fiber orientations showing self-similar crack propagation. Humid environments accelerated the fatigue crack growth considerably compared to the vacuum and inert gas environments. Failure stress intensity ( $K_f$ ) appeared to have a lower value in humid environments.

Key Words: Titanium metal matrix composite materials, Fracture, Fatigue crack propagation, Mixed mode loading, Gaseous environments.

\* Presently with Olin Metals Research Laboratory, New Haven, CT.

## INTRODUCTION

Because of their high strength to weight ratio, high modulus and toughness, titanium-metal matrix composites have long been considered for applications in dynamic structures. However, like other metal matrix composites, (MMCs) titanium-matrix composites are characterized by anisotropy, heterogeneity and interfaces. Tensile properties of titanium matrix composites reinforced with continuous SiC, Borsic, and  $B_4C/B$  fibers have been studied (1-4) and the results indicate that the mechanical properties of such composites are dependent on the interfaces or the reaction zone formed during fabrication. The off-axis properties have also been found to be highly influenced by the nature of the fiber matrix interface (4, 5).

Axial fatigue studies on the titanium-matrix composites have been carried out (6, 7) and it was suggested (6) that the fatigue processes in metal matrix composites are strictly matrix controlled. A titanium matrix composite by virtue of its relatively sound fiber matrix bonding permits very little fiber/matrix delamination for the as-fabricated specimens. However, if the interface could be weakened enough to permit debonding, the sharp cracks will blunt at the interface, resulting in higher fatigue strength (6). In addition to axial tensile and fatigue properties, mixed mode crack propagation behavior in MMCs is of extreme

importance. During transverse mode I loading, the crack propagating through a brittle interfacial region around the fiber experiences a mixed mode loading condition. Many attempts at modeling the mixed mode fracture in fibrous composites have been made (8-13). Initial theories were based on application of fracture mechanics to the anisotropic materials. For an orthotropic material, expressions were derived for the case of a crack lying along a plane of symmetry and were of the kind

$$G = G_I + G_{II}$$

for self-similar crack growth. It was assumed (8, 13) that the composite material is an orthotropic plate and therefore

$$G = G_I + G_{II} = \left( \frac{S_{11} + S_{22}}{2} \right)^{\frac{1}{2}} \left[ \left( \frac{S_{22}}{S_{11}} \right)^{\frac{1}{2}} + \frac{2S_{12} + S_{66}}{2S_{11}} \right]^{\frac{1}{2}} \\ [K_I^2 + \left( \frac{S_{11}}{S_{22}} \right)^{\frac{1}{2}} K_{II}^2]$$

where  $S_{11} = 1/E_{11}$ ;  $S_{22} = 1/E_{22}$ ;  $S_{12} = -\nu_{12}/E_{11} = \nu_{21}/E_{22}$ ;  $S_{66} = 1/G_{12}$ .

Based on the observation that most of the mixed mode crack propagation is not self-similar, a strain energy density theory was proposed (9, 10). This theory predicts that the mixed mode crack extension in composites will

occur at a certain angle  $\theta$  determined by the strain energy density field around the crack. A recent model (12) studies the condition under which a self-similar crack propagation due to critical strain energy release, changes to a trans-fibral path.

All these models, however, ignore several important factors which limit their applications. The crack propagation in MMCs is a complex process involving several failure debonding, fiber pull-out etc. It is difficult to have a generalized mechanics theory to include many of these mechanisms acting simultaneously. Also one of the most important things affecting the fracture modes is the interface. A weak interface can act as a crack arrester, and will also have detrimental effects on the off-axis tensile properties. It was shown (4) that at lower fiber angles most of the mixed mode theories cannot agree with the experimental data because of the influence of the interfaces.

Finally, fatigue crack propagation (FCP) behavior of titanium-matrix composites in environments of different humidities needs study. It is expected that because of different failure and crack arresting mechanisms, fatigue crack growth properties of the composite should be better than that of the matrix. Studies of FCP of such composites

in different environments and identification of failure modes is necessary.

The purpose of this paper is to study the fracture and fatigue crack growth properties of Ti-6Al-4V matrix continuous fiber composites. Tensile data on the as-received and heat treated conditions is presented along with the fracture modes. Mixed mode fracture is studied under both of these conditions and data is compared to available mixed mode theories. Fatigue crack growth studies are presented and modes of failure are studied. Mixed mode fatigue crack growth data is then presented for the as-received and isothermally heated condition, with the emphasis on the effect of the interface on the failure modes. The fatigue crack growth is then modeled in terms of the change in the strain energy release rate.

#### Material System

The composite system used in this study was continuous  $B_4C$  coated boron fibers in a Ti-6Al-4V matrix. A typical micrograph of the as-received condition of the composite is shown in Fig. 1(a). The fibers are approximately 150 microns in diameter. The  $B_4C$  coating is approximately 4 microns. The fibers represent a volume fraction of approximately 40% in a 4 ply composite sheet of 0.88 mm thickness. As evident from the micrograph, small radial cracks were noticed in the boron fibers.

## II. Fatigue Crack Growth and Mixed Mode Fatigue Crack Growth Testing

Fatigue crack growth experiments were done on a closed loop-electrohydraulic system. The test frequency was 1 Hz. Compact tension specimens ( $H/w=1$ ,  $a_o=2.5$  mm) were used for the longitudinal fiber orientation ( $\theta=0^\circ$ ), and edge notched specimens (15) ( $a_o/w=0.3$ ,  $w=25$  mm) were used for most of the mixed mode experiments\*. For the mixed mode fatigue crack growth experiments (i.e., for  $\theta=30^\circ$ ,  $45^\circ$ , and  $90^\circ$ ), the initial notches were cut along the fiber direction. Fig. 2 shows various specimen configurations. The crack growth was measured by an optical microscope. It should be noted at this point that for all the experiments the fatigue crack propagation was self-similar, i.e., along the direction of the initial notch. No gross delamination was observed for the longitudinal specimens. The majority of the experiments were done at constant load range ( $\Delta P$ ) and load ratio ( $R=0.1$ ) with the remaining experiments done at constant  $\Delta K$  and  $R=0.1$ . In order to determine the effect of degraded

---

\* CT specimens were not used for the off-axis orientation because the loads were too small to get the desired  $\Delta K$  and were in the error range of the FCP testing machine.



interface on the fatigue crack propagation (FCP) all the experiments were repeated for the specimens heat treated at 500°C in air. Here also the FCP was self-similar. The FCP data is plotted in Fig. 3 through Fig. 6.

In order to study the influence of gaseous environments, FCP experiments were done in a 100% RH environment, at  $10^{-6}$  torr vacuum and in dry  $N_2$  gas environment. Only longitudinal compact tension specimens were used. The tests were conducted at constant  $\Delta P$  and  $R$  and at a frequency of 1 Hz. The results are plotted in Fig. 6.

### III. Fractography and Interface Characterization

All the tensile and fatigue fractured surfaces were than viewed in a high resolution SEM to determine the failure paths and mechanisms. In addition, in-situ fractured specimens were studied in a Scanning Auger Spectroscope. Chemical and quantitative analysis of the fractured surface was carried out. The fractured surface was then inert ion sputtered by 3KeV argon ions at a  $0.4 \text{ mA/cm}^2$  ion current density. The chamber pressure was  $3.6 \times 10^{-5} \text{ Pa}$ . Chemical depth profiles for various elements were recorded. Fig. 7 gives the depth profile of oxygen for the as-received and heat treated condition.

## Results and Discussion

The fracture stress values for the unnotched as-received and heat treated specimens are given in Table 1. It can be seen that the heat treatment in vacuum has a minimal effect on the mechanical properties of the composite while the heat treatment in air has a considerable effect on the longitudinal strength of the composite and almost no effect on the transverse properties. The reduction in longitudinal strength is due to the interface degradation during the heat treatment. Little change in transverse properties indicates that the transverse strength is representative of the intrinsic strength of the matrix.

The fracture stresses for the notched, mixed mode type experiments are listed against the fiber orientation for the as-received and 500°C air heat treatment condition, in Table 1. Significant reduction in the longitudinal strength is observed and little change in transverse properties is seen. As stated in earlier work (4), the mixed mode theories (8-13) only agreed with the experimental data at angles  $> 35^\circ$ . At lower angles, however, different types of failure mechanisms are observed. Also, the interface influences the crack propagation significantly. Optical microscopy showed (4) that for the as-received condition, the crack propagation was predominantly along the

fibers, for angles above  $35^{\circ}$ . Below  $35^{\circ}$  however, the cracking was at a certain angle to the initial notch. For the  $500^{\circ}\text{C}$  air heat treated condition however, the crack extension was along the fiber orientation for all but the longitudinal measurements.

The reduction in the longitudinal strength by the heat treatment in air is due largely to the fiber and the interface degradation of the composite. In order to document the change in the chemical nature at the fractured surface, or the interface, SAM studies were done on the as-received as well as the heat treated specimens (4). It has been shown that a large concentration of brittle carbides, oxides, and chlorine and sulfur was found on the in-situ fractured surface of  $\text{B}_4\text{C}/\text{B} - \text{Ti-6Al-4V}$  composites for both conditions. However, an unusually high concentration of oxides was found for the air heated specimens. When inert ion sputtered into the fiber, the oxygen concentration decreased as shown in Fig. 7. Compared to the air-heat treated condition, the as-received specimen and the vacuum heat treated specimen showed much less oxygen at the interface. Thus increased oxide formation at the interface can be considered as a possible degrading mechanism.

### Fatigue Crack Growth: Longitudinal Fibers

As mentioned earlier, since the FCP for all the longitudinal specimens was mode I, it was possible to plot the data in a conventional ( $da/dN$  vs  $\Delta K$ ) was.

Fig. 3 shows the FCP curve for the as-received Ti-6Al-4V matrix composites. For comparison the data for Ti-6Al-4V (recrystallization annealed) is also plotted. It can be seen from the two curves, that the composite  $da/dN$  curve is much steeper ( $m_{\text{composite}} > m_{\text{matrix}}$ ) and the  $K_{\text{failure}}$  for the matrix is greater than the  $K_{\text{failure}}$  of the composites. The composite exhibits slower crack growth rates than the matrix at lower  $\Delta K$  values ( $\Delta K < 27.5 \text{ MPa}/\sqrt{\text{m}}$ ). Lower fiber fatigue strength can explain why the composite has a steeper  $da/dN$  curve and a lower  $K_{\text{failure}}$ . At lower  $\Delta K$  values, fiber matrix interfaces can act as crack bluntners, retarding the growth. However, as  $\Delta K$  is increased, the fibers cannot withstand the stress cycling and start fracturing providing crack initiation sites. At a certain  $\Delta K$  the matrix cannot withstand the stress and fractures showing much lower  $K_{\text{failure}}$ . SEM of the fractured surface reveal local debonding, fiber pullout and fiber cracking (Fig. 4).

### Mixed Mode Fatigue Crack Growth

FCP experiments were carried out on  $\theta=0^\circ$ ,  $30^\circ$ ,  $45^\circ$ , and  $90^\circ$  specimens for the as-received as well as air heat treated conditions. A very interesting observation was that for all the orientations, the crack extension was self-similar, unlike predicted in the strain-energy density theory (9, 10). Even for the  $30^\circ$  specimen, which has shown a non-self-similar crack propagation during tension testing, the FCP was self-similar. FCP, as opposed to high strain rate tension testing, is a slow incremental crack extension process, resulting in self-similar crack growth even at lower fiber angles. This observation enabled the monitoring of crack growth in the fiber direction. Because of the self-similar FCP, the  $da/dN$  was then plotted against  $\Delta G$ , the range in strain energy release rate, where  $\Delta G = \Delta G_I + \Delta G_{II}$ . I and II represent the modes of loading and  $\Delta G_I \propto \frac{\Delta K_I^2}{E_I}$ ,  $\Delta G_{II} \propto \frac{\Delta K_{II}^2}{E_{II}}$ . The critical fracture toughness of these composites is highly anisotropic, just as the modulus, which was the reason for selecting the above approach. Thus  $da/dN$  is plotted against  $\Delta G$  for  $\theta=0^\circ$ ,  $45^\circ$ , and  $90^\circ$  specimens as shown in Fig. 5 for the as-received and air heat-treated condition. Due to the lack of K-calibration, the data for  $30^\circ$  specimen is plotted as 'a' against N (Fig. 5(c)).

As can be seen from Fig. 5(a), the as-received mixed mode FCP data follow the law

$$\frac{da}{dN} \propto \Delta G^m \quad m \sim 3$$

The slope  $m$  for all the angles is the same. As expected, the longitudinal ( $\theta=0^\circ$ ) specimen shows slower crack growth and much higher  $G_{\text{failure}}$ .

FCP curves for the heat treated specimens are plotted in Fig. 5(b). In general, the FCP observed was slower than the as-received specimens. This slowing down effect was much more pronounced for the transverse ( $\theta=90^\circ$ ) specimen than the longitudinal one. The longitudinal specimens recorded a lower  $K_{\text{failure}}$  than the longitudinal as-received specimens. The  $K_{\text{failure}}$  for other orientations changed only slightly. The vacuum heat treated longitudinal specimen showed slower crack growth than the as-received condition.

The SEM fractographic studies on FCP fracture surfaces for the as-received transverse and  $\theta=45^\circ$  specimen are shown in Fig. 8(a) and those for the air heat treated specimens are shown in Fig. 8(b). It is evident that for the as-received condition the fatigue crack has propagated by splitting the fibers to the core. This means that the fiber/matrix interface was not the weak link. The reason may be partly due to the inherent radial cracks in the boron fibers seen in as-received micrograph (Fig. 1). These cracks can extend during cycling and split the fibers

radially providing the least resistant path for the main fatigue crack. In the air heat treated condition, however, the fatigue crack propagated through the fiber/matrix interface only, as seen in Fig. 8(b). This is explainable by the observation that the interfaces of the heat treated specimens were degraded by oxides as shown by the SAM studies. Therefore the interface provided the weakest path for fatigue crack propagation.

The failure strain energy release rate  $G_f$  for the composite is highly orientation dependent.  $G_f$  for the longitudinal specimen is almost an order of magnitude higher than transverse specimen (Fig. 5). The reason can be traced in the fact that for longitudinal specimens fiber breaking mechanism constitutes the resistance to fracture, while for the other orientations it is either radial crack extension, or interface splitting mechanism.

This observation is consistent with that predicted by several models (17, 18) which have estimated that the value of  $G_f$  for fiber fracturing mechanism is much higher than for debonding mechanisms. For fiber fracture  $G_f$  can be estimated as

$$G_f \propto \frac{\sigma_f^2}{E_{\text{long}}}$$

which can also explain the observation that the  $G_f$  for as-received composite has a higher value than that of the air heat treated. It should be noted here that the value

of  $G_f$  is not only indicative of the anisotropy of the material but also indicates the type of failure mechanism involved (i.e., fiber breaking, debonding, splitting, etc.) Therefore, if the mixed mode data for the as-received material is normalized by  $G_f$  one can plot  $da/dN$  against  $\frac{\Delta G}{G_f}$  for all the fiber orientations. This curve is shown in Fig. 9. It is an interesting fact that all the data in Fig. 5 for the as-received material collapses to form one single curve

$$da/dN \propto \left( \frac{\Delta G}{G_f} \right)^m \quad m \sim 3$$

for all the fiber orientations. This type of curve can be very useful in predictive analysis since it takes care of the anisotropy of the composite. Using the form

$$G_f \propto \frac{\sigma_f^2}{E} \quad \text{we can write}$$

$$da/dN \propto \left( \frac{\Delta G x E_\theta}{2 \sigma_f(\theta)} \right)^m$$

for all the fiber orientations showing self-similar crack growth.

#### Effect of Gaseous Environments on the FCP

Fig. 6 shows the FCP behavior of  $B_4C-B/Ti-6Al-4V$  longitudinal specimens in different environments. It can be noticed that at lower  $\Delta K$  values there is an order of



magnitude difference in FCP rates between vacuum and 100% RH. The fatigue crack growth rate tends to be greater in environments of increased humidity. The difference in FCP rates in dry  $N_2$  gas and vacuum were minimal. Vacuum and  $N_2$  gas FCP showed a higher value of  $K_{failure}$  than the wet air, suggesting an environmental effect on the  $K_C$  of the material. This effect is under further study.

Fractographic studies (Fig. 11) showed a considerable matrix damage and fiber cracking for the 100% RH FCP specimens. The fatigue in vacuum, however, showed a cleaner matrix with evidence of fiber breakage and pull out. The fracture surfaces for the  $N_2$  gas and vacuum were similar.

Finally, a note on the effect of heat treatment on the matrix. As shown earlier, the heat treatment transports some oxygen down the interface. Oxygen is also present in the matrix. Increasing oxygen content can lead to increasing the grain size (19). Although there is a slight increase in strength with corresponding reduction in fracture toughness, it was observed that increasing oxygen content did not affect the Stage II FCP properties of recrystallization annealed Ti-6Al-4V alloys (19). Therefore, it is concluded that it is the fiber/matrix interface which is degraded by the heat treatment rather than the matrix.

In summary, the tensile, mixed mode and fatigue crack propagation studies carried out on the as-received and heat-treated  $B_4C$ -B/Ti-6Al-4V composites resulted in the following conclusions:

1. The  $500^{\circ}C$ , 7 days in air heat treatment reduced the longitudinal strength by about 30%, but had no effect on the transverse strength. The vacuum heat treatment had minimal effect on the mechanical properties.
2. Mixed mode tensile crack propagation was self-similar except for the fiber angles below  $35^{\circ}$ .
3. SAM studies revealed increased oxide formation due to heat treatment in air at the fiber matrix interface.
4. The fatigue crack propagation for the longitudinal as well as off-axis specimens was self-similar. For the longitudinal specimens the slope of  $da/dN$  vs.  $\Delta K$  curve was much steeper than the Ti-6Al-4V matrix curve with a lower  $K_{failure}$ .
5. The mixed mode FCP was self-similar, and was found to follow the law  $da/dN \propto \Delta G^m$ , for the as-received and heat treated specimens.
6. For the as-received specimens, normalization by  $G_f$  led to a generalized curve

$$\frac{da}{dN} \propto \left( \frac{\Delta G}{G_f} \right)^m \quad \text{for } \theta = 0^\circ, 45^\circ, \text{ and } 90^\circ$$

specimens for self-similar crack growth.

7. Fractography revealed that the fatigue crack splits the fibers in the as-received off-axis specimens but follows an interfacial path in case of heat treated specimens. This could explain the slower crack growth rates in the heat treated samples.
8. Humid environments tend to accelerate the FCP of the longitudinal specimens. They also show a lower  $K_{\text{failure}}$  than the inert or vacuum environments.

#### Acknowledgements

This research was sponsored by the U.S. Air Force Office of Scientific Research through grant number 80-0052. We would like to thank the AFML for supplying the Titanium composites, and N. Williams, Dr. Michael Schmerling and Carlos Arias for experimental assistance, and Keller Towns for metallographic work.

References

1. Metcalfe, A.G. "Composite Materials," v. 4, Academic Press (1974) pp. 269-318.
2. Collins, B.R., W.D. Brentnall and I.J. Toth, "Failure Modes in Composites I," I.J. Toth, ed., TMS-AIME (1973) p. 103.
3. Brentnall, W.D. and I.J. Toth, "Failure Modes in Composites I," I.J. Toth, ed., TMS-AIME (1973), p. 129.
4. Mahulikar, D.S., Y.H. Park, and H.L. Marcus, Proceedings Greece/USA Mixed Mode Fracture Conference, Athens, Greece (1980).
5. Klein, M.H., "Interfaces in Metal Matrix Composites," Composite Materials, v. 1, A.G. Metcalfe, ed., Academic Press (1974), p. 169.
6. Shimmin, K.D. and I.J. Toth, Failure Modes in Composites I, I.J. Toth, ed, TMS-AIME (1973) p. 357.
7. Christian, J.L., "Fatigue of Composite Materials," ASTM STP 569, (1975), pp. 280-292.
8. Paris, P.C. and Sih, G.C., "Fracture Toughness Testing and its Applications," ASTM STP 381 (1965) pp. 133-196.
9. Sih, G.C. and Chen, E.P., J. Comp. Mat., v. 7 (1973) pp.230-244.
10. Sih, G.C., Chen, E.P., Huang, S.L. and McQuillen, E.J J. Comp. Mats. v. 9 (1975) pp. 167-186.
11. Corten, H.T. in "Fracture" volume VII, Academic Press (1972) pp. 675-769.
12. Tirosh, T., Eng. Fract. Mech. 13 (1980) pp. 119-127.
13. Konish, H.J. Jr, in Fracture Mechanics of Composites, ASTM STP 593 (1975) pp. 99-116.
14. Vega-Boggio, J. and Vingsbo, O., J. of Mat. Sci. 12 (1977), pp. 2519-2524.

15. Rooke, D.P. and Cartwright, D.J., Compendium of Stress Intensity Factors, The Hillingdon Press, Uxbridge (1976), pp. 96-97.
16. Tsai, S.W., "Mechanics of Composite Materials I," AFML-TR-66-149, June (1966).
17. Iremonger, M.J. and Wood, W.J., J. of Strain Analysis 5, no. 3 (1970), pp. 88-96.
18. Willimas, R.S. and Reifsnider, K.L., "Fracture Mechanics" ASTM STP 677 (1979), pp. 629-650.
19. Chesnutt, J.C., Thompson, A.W., and Williams, J.C., "Influence of Metallurgical Factors on the Fatigue Crack Growth Rates in Alpha-Beta-Titanium Alloys," AFML-TR-78-68, May (1978).

Nomenclature

$a$	Crack length
$da/dN$	Fatigue crack growth
$E_{\theta}$	Young's modulus in $\theta$ direction
$\theta$	Fiber orientation with respect to the load line
$G$	Strain energy release rates
$G_I, G_{II}$	Strain energy release rates for mode I and II loading
$\Delta G$	Range in the strain energy release rate
$G_F$	Failure strain energy release rate
$G_{12}$	Shear modulus
$H$	Half height of the compact tension specimen
$K$	Stress intensity factor
$K_I, K_{II}$	Stress intensity factor for mode I and II loadings respectively
$\Delta K$	Range in the stress intensity factor
$K_F$	Failure stress intensity factor
$m$	Exponent
$N$	Number of cycles
$P$	Load
$\Delta P$	Range in the load
$R$	Load ratio
$w$	Width of the specimens
$\sigma$	Stress
$\sigma_F$	Failure stress

Figure Captions

- Fig. 1 (a) The as-received  $B_4C$  coated boron/Ti-6Al-4V composite.
- (b)  $B_4C$ -B/Ti-6Al-4V heat treated at  $500^{\circ}C$  7 days in air.
- Fig. 2 (a) Longitudinal and off-axis FCP specimens.
- (b) A notched tension specimen.
- Fig. 3 Fatigue crack growth data for  $B_4C$ -B/Ti-6Al-4V longitudinal specimen, in comparison with Ti-6Al-4V recrystallization annealed (19) matrix.  $R=0.1$ .
- Fig. 4 Fatigue fractured surface of the longitudinal as-received  $B_4C$ -B/Ti-6Al-4V material.
- Fig. 5 Mixed mode fatigue crack growth of  $B_4C$ -B/Ti-6Al-4V composites; for (a) as-received (b) heat treated condition, and (c)  $30^{\circ}$  fiber angle specimen.
- Fig. 6 Effect on gaseous environment on the fcp of  $B_4C$ -B/Ti-6Al-4V longitudinal specimens.
- Fig. 7 Depth profile for the in-situ fractured surface of  $B_4C$ -B/Ti-6Al-4V composite. Depth calculated from sputtering at same parameters on standard titanium oxide.

Fig. 8 (a) Fatigue fractured surfaces for the as-received transverse and  $\theta=45^\circ$  orientation  $B_4C-B/Ti-6Al-4V$ .

(b) Fatigue fractured surfaces for the heat treated transverse and  $\theta=45^\circ$  orientation  $B_4C-B/Ti-6Al-4V$ .

Fig. 9  $da/dN$  against  $\Delta G/G_F$  data for longitudinal, transverse and  $\theta=45^\circ$  orientation specimens for as-received condition.

Fig. 10 Fatigue fractured surface of the air heat treated  $B_4C-B/Ti-6Al-4V$  longitudinal specimen.

Fig. 11 SEM fractography of the fatigue fractured surfaces in vacuum,  $N_2$  gas and 100% RH air.



Table 1

Fracture Strength of the As-received and  
the Heat Treated B<sub>4</sub>C-B/Ti-6Al-4V Specimens

Fiber Angle $\theta$ Degrees		As-received MPa	7 days 500°C Heat treated in vacuum	in air
0	Notched	1000	—	580
15	Notched	900	—	—
30	Notched	590	—	—
45	Notched	470	—	400
60	Notched	390	—	—
90	Notched	345	—	355
0	Unnotched	1035	920	780
15	Unnotched	900	—	—
30	Unnotched	610	—	—
45	Unnotched	490	460	480
60	Unnotched	390	—	—
90	Unnotched	350	361	345

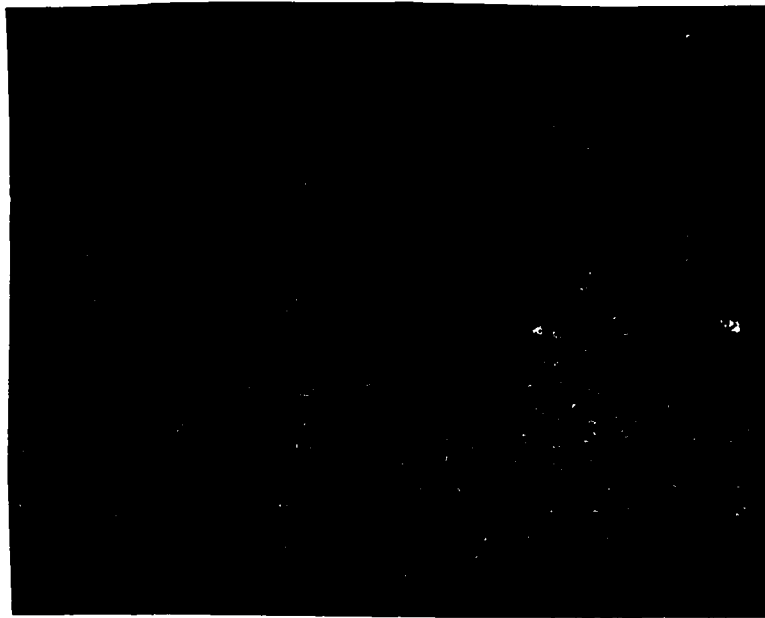
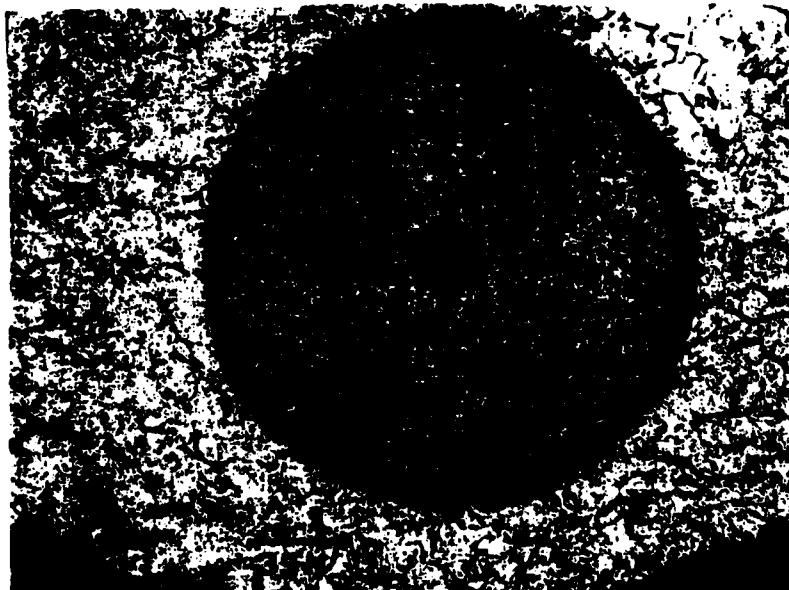
For the Composite System

$$E_1 = 240 \times 10^3 \text{ MPa}$$

$$E_2 = 170 \times 10^3 \text{ MPa}$$

$$G_{12} = 60 \times 10^3 \text{ MPa}$$

$$\nu_{12} = 0.28$$

**(a)****(b)****Figure 1**

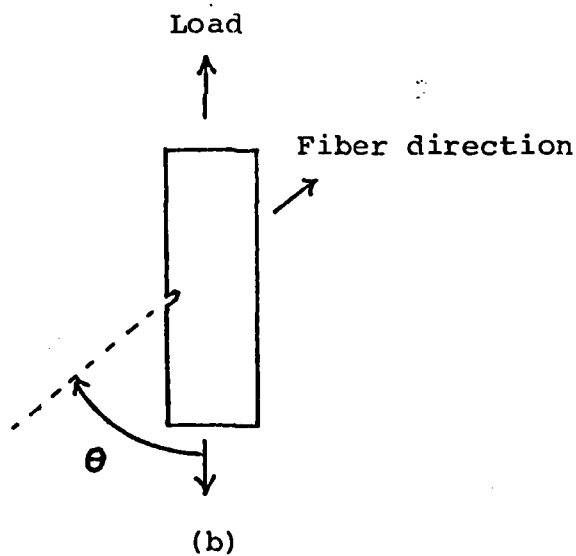
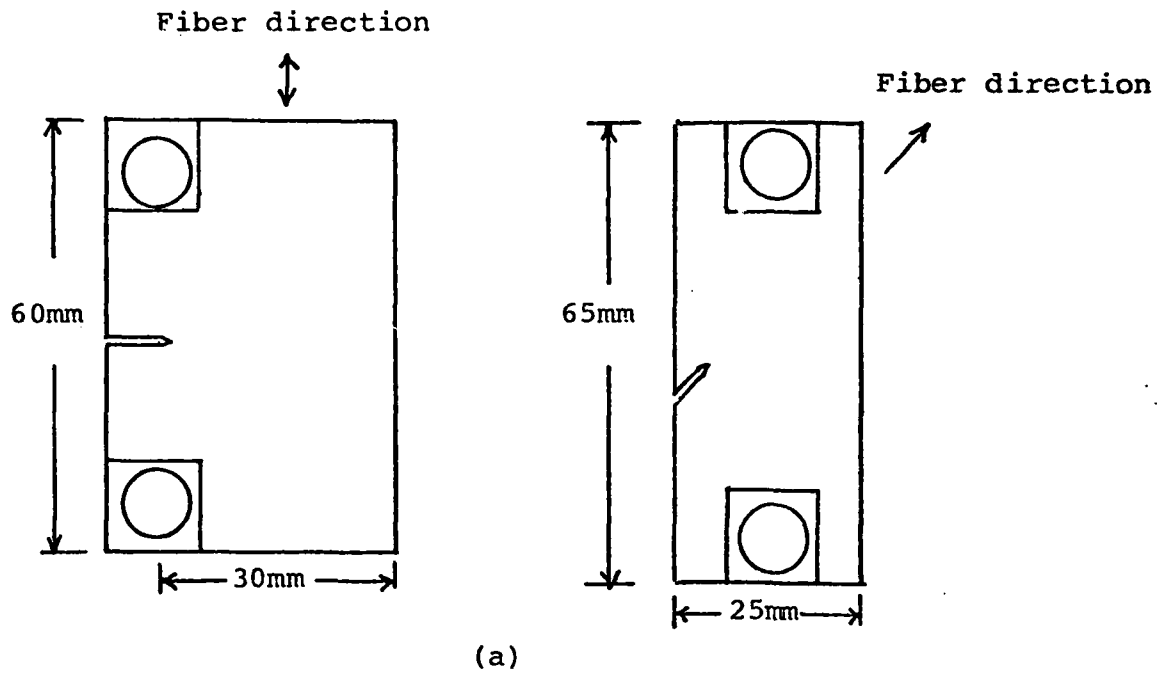


Figure 2 (a) Compact tension longitudinal and off-axis edge notched FCP specimens. Aluminum doublers are used to strengthen the pin points.

(b) Notched tension specimen.  $\theta$  is the fiber angle.

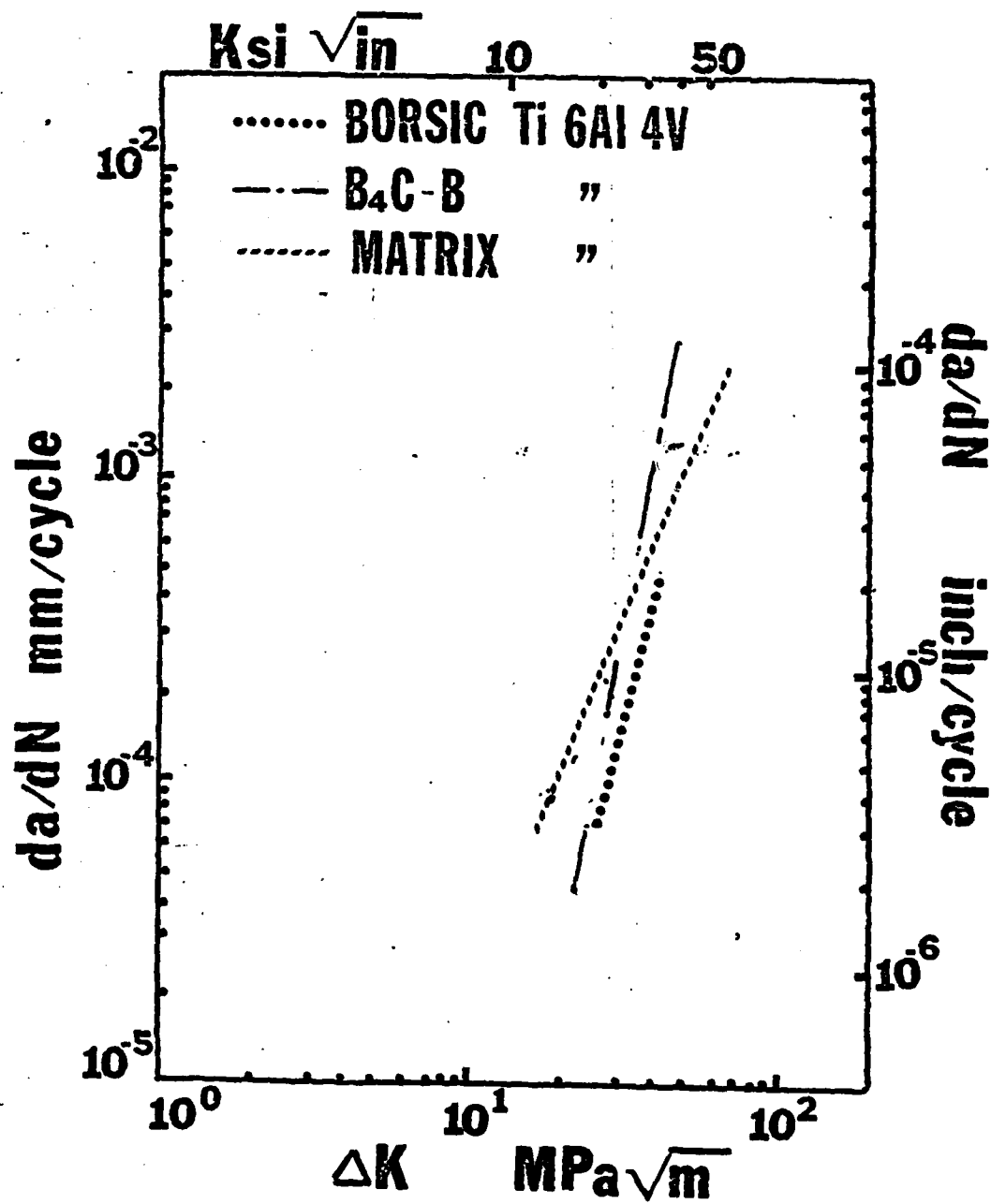


Figure 3

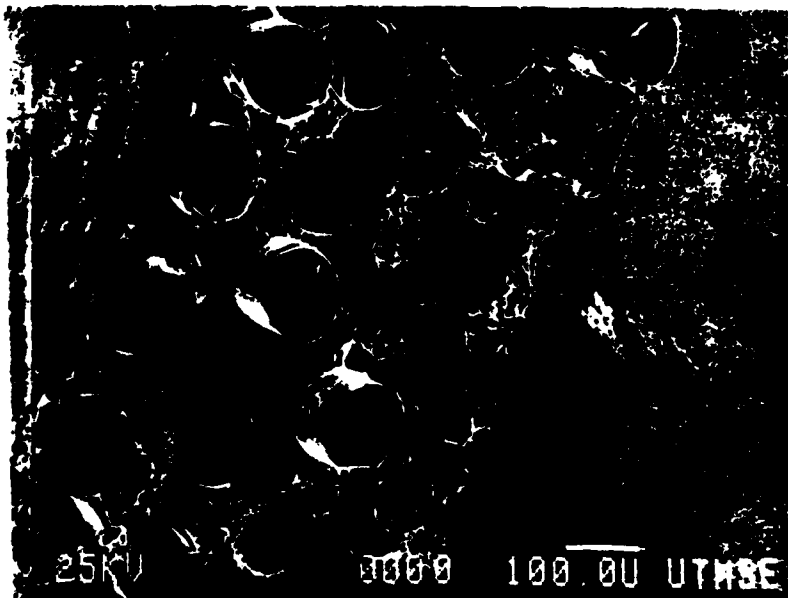


Figure 4

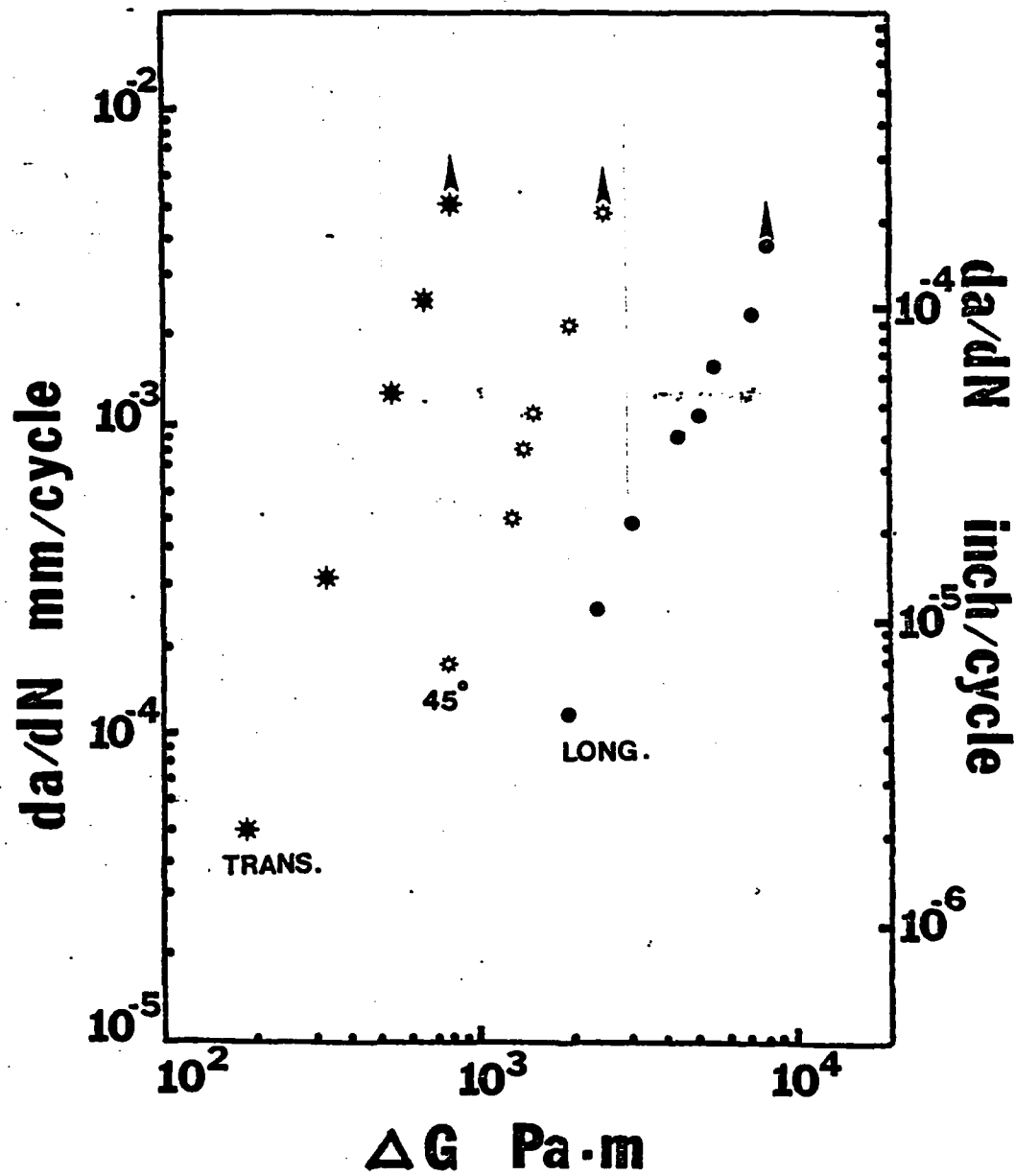


Figure 5(a)

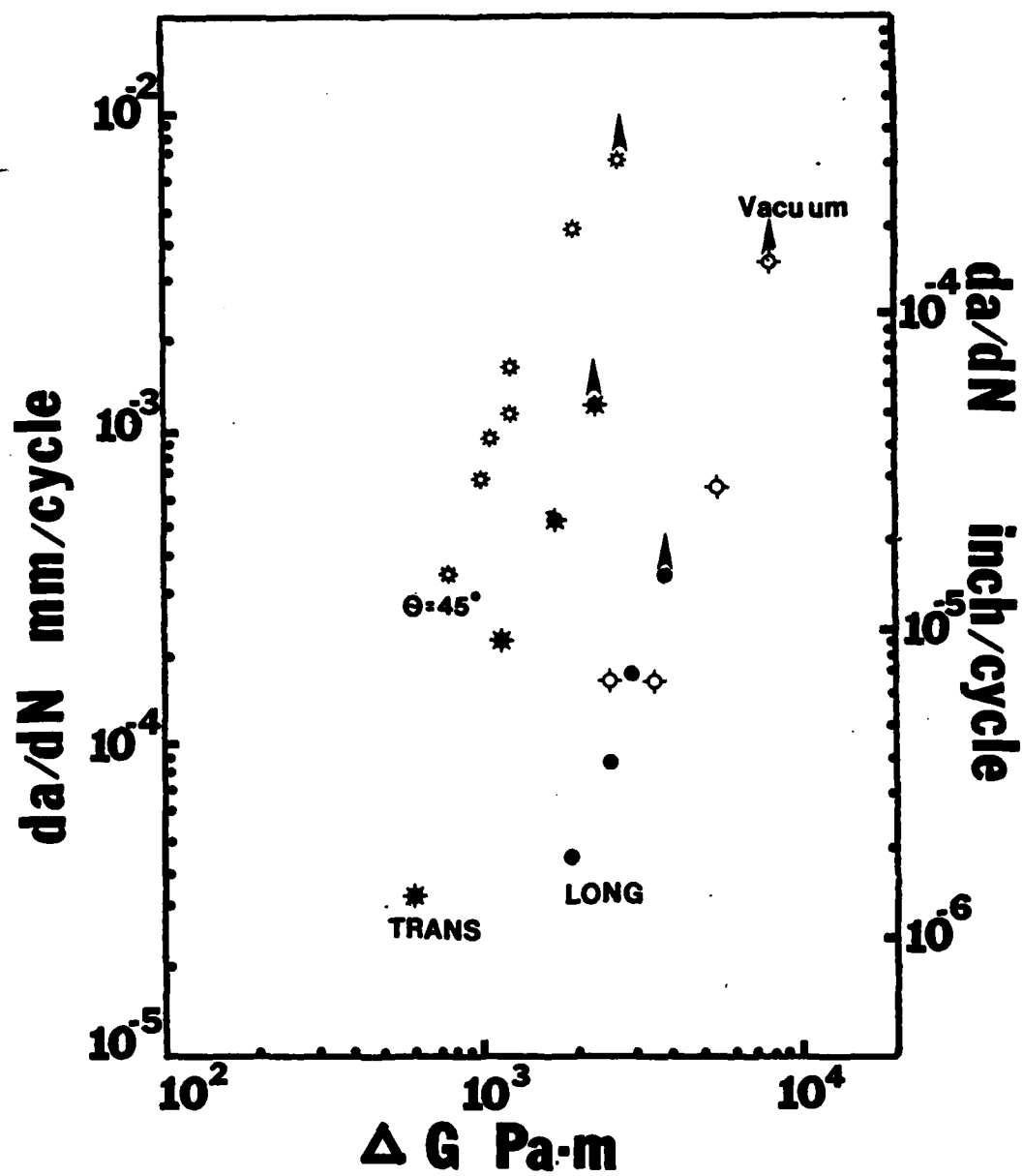


Figure 5(b)

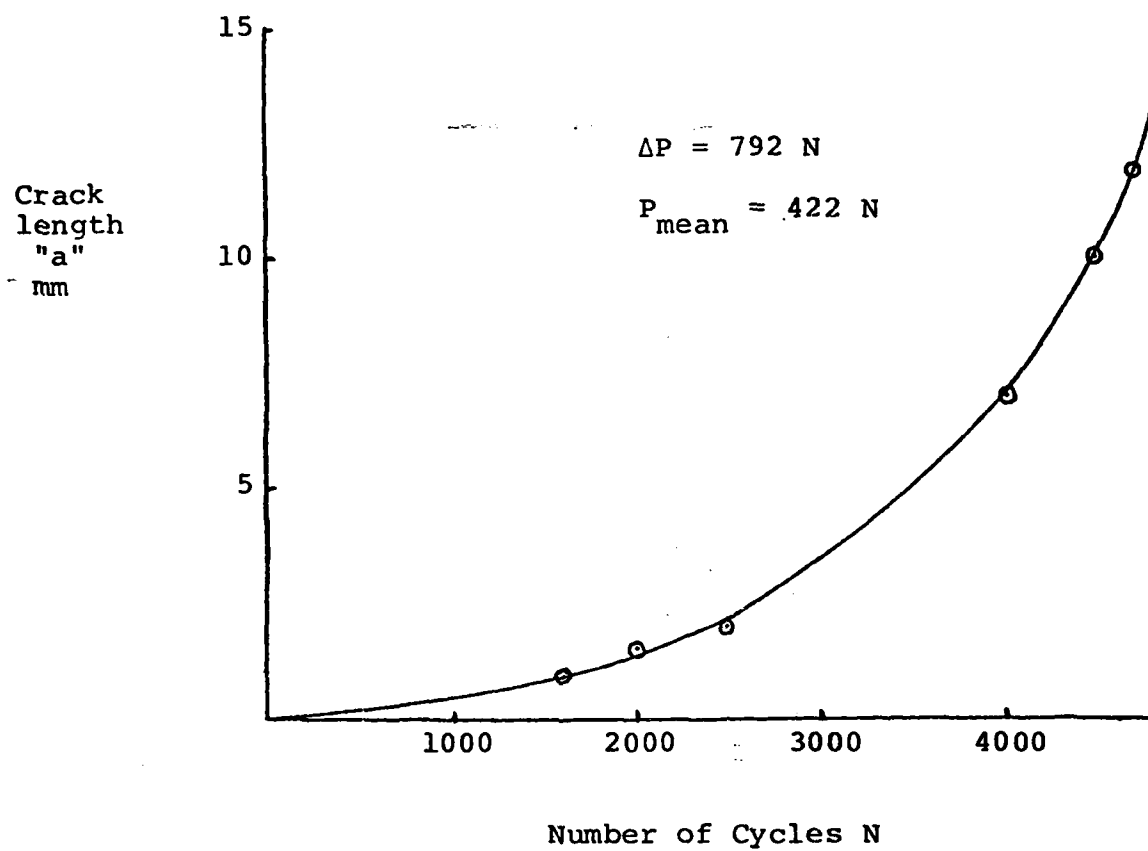


Fig. 5(c) FCP data for the  $30^\circ$  fiber angle  $B_4C-B/Ti-6Al-4V$  CT specimen.



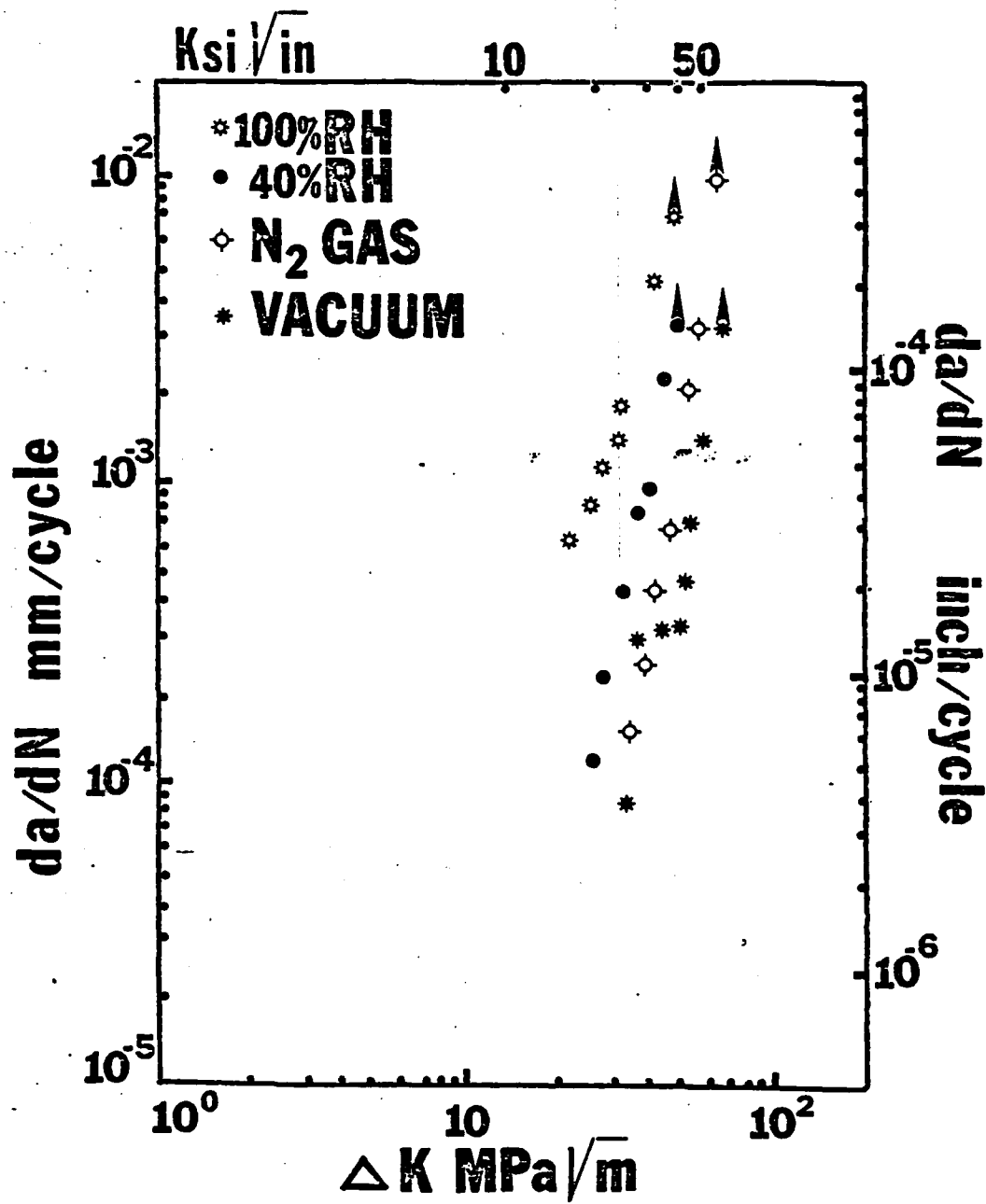


Figure 6

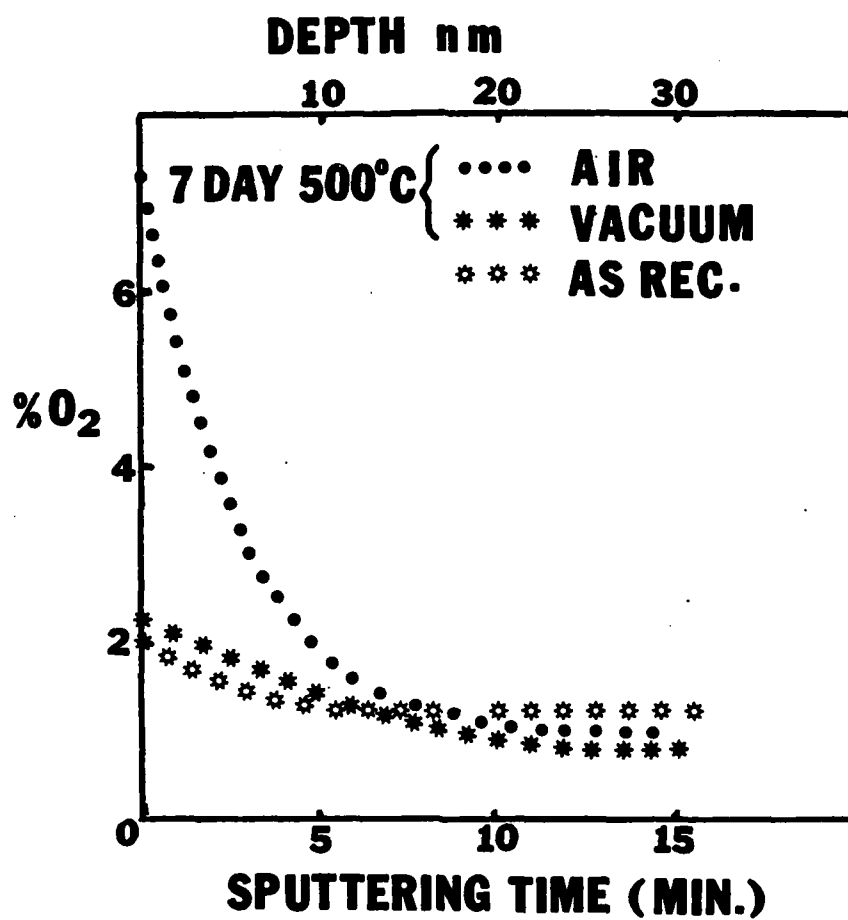
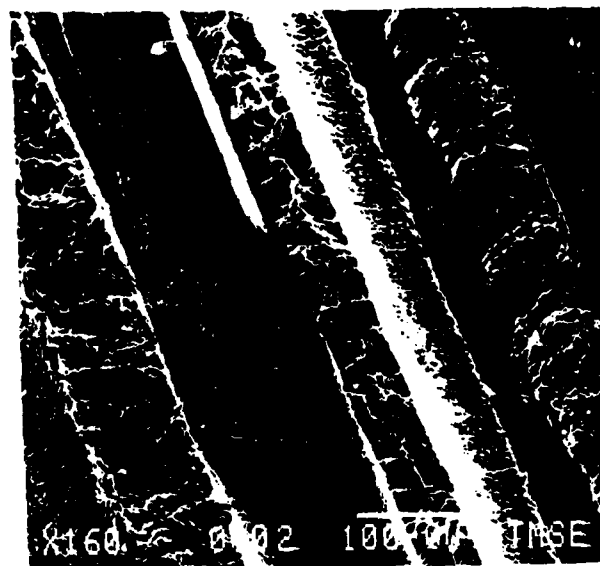
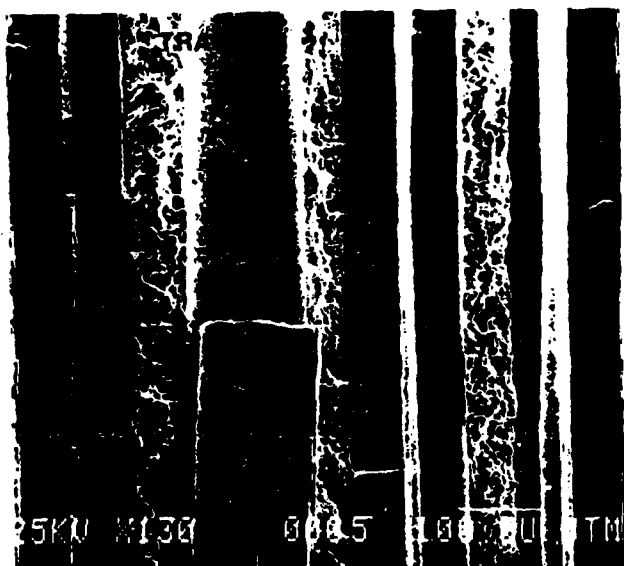
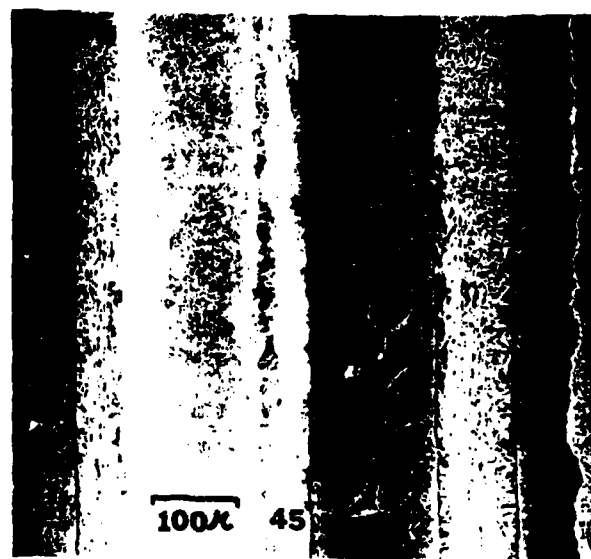
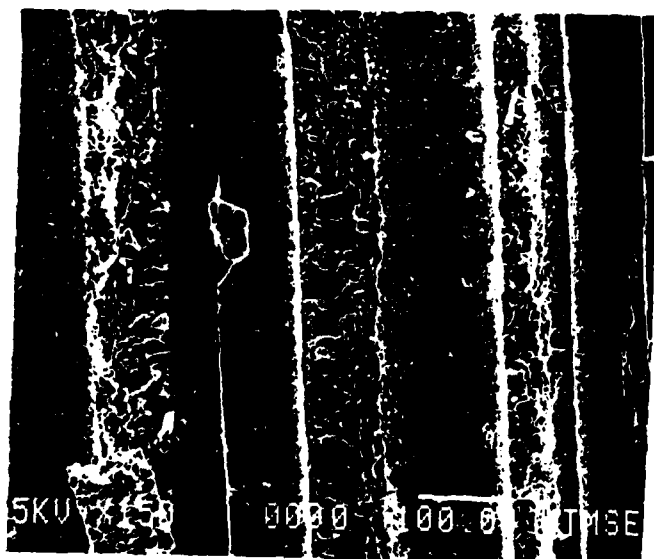


Figure 7



(a)



(b)

Figure 8

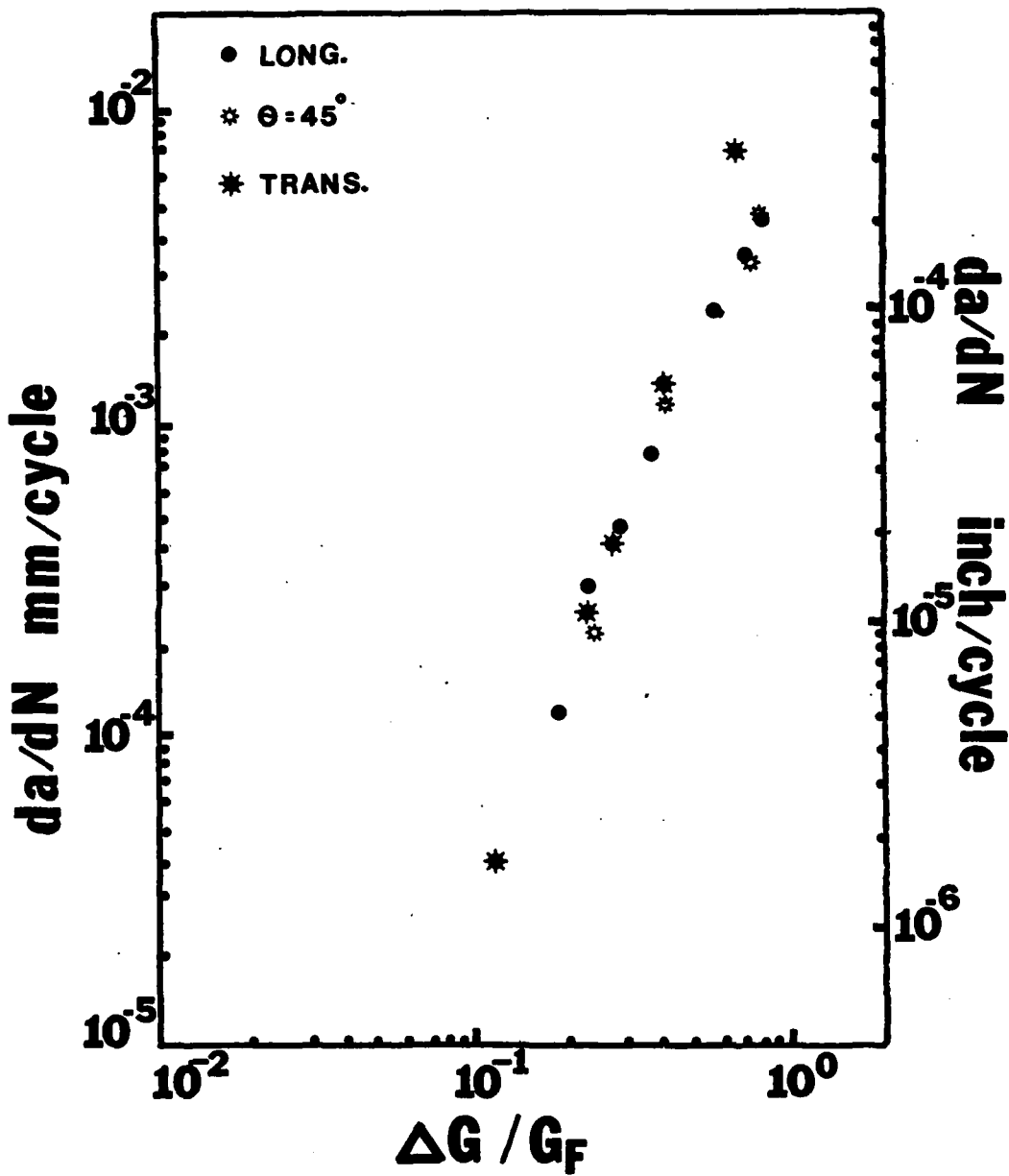


**Figure 9**

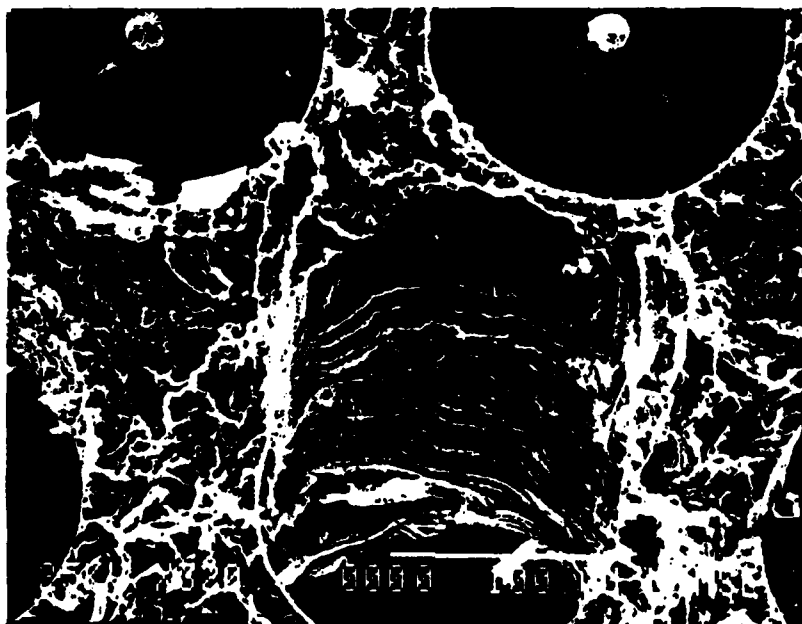


Figure 10

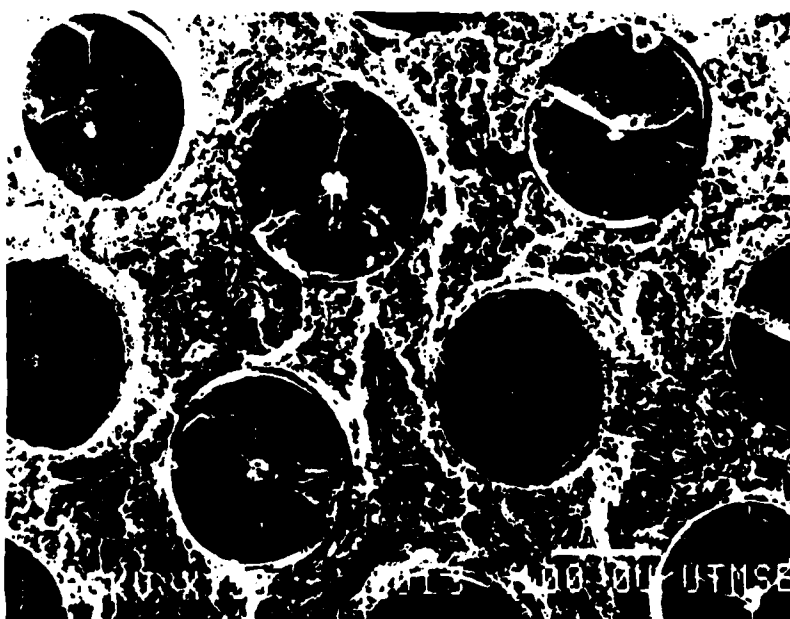


Figure 11

# Environmentally Influenced Mixed Mode Fatigue Crack Propagation of Titanium Metal Matrix Composites

DEEPAK MAHULIKAR and H. L. MARCUS

Effect of humid air environments on the mixed mode fatigue crack propagation behavior of B<sub>4</sub>C-B and BORSIC reinforced Ti-6Al-4V metal matrix composites was studied. Humid environments enhanced the mixed mode fatigue crack propagation rates in the as-received titanium matrix composites at  $R = 0.1$ . The effect was more pronounced in the transverse and 45 deg specimens. A transition in failure modes from fiber splitting in humid air to interfacial splitting in dry environments was observed at a load ratio of 0.1. The transition took place at around 100 Pa water vapor pressure, where a steep rise in fatigue crack propagation rate was noticed. At  $R = 0.5$ , however, no fiber splitting was observed in humid air. Fatigue crack closure load measurements revealed that closure loads were higher in humid air than in dry environments. The fiber splitting is suggested as an environmentally induced crack closure effect, where plastically deformed matrix sets up stress fields (radial and mode III stresses) on the brittle boron fibers weakened by the humidity.

## I. INTRODUCTION

UNIDIRECTIONALLY reinforced titanium metal matrix composites have long been considered for applications in dynamic structures.<sup>1,2</sup> However, little work is reported on some important properties such as mixed mode fracture and fatigue crack propagation (FCP) behavior of these composites. Because of the inherent anisotropy and the presence of fiber-matrix interfaces, understanding mixed mode fracture behavior of such composites is essential. Studies were, therefore, aimed at the mixed mode behavior of the as-received composites and the results have been reported elsewhere.<sup>3</sup> It was observed that the mixed mode fatigue crack propagation of the as-received B<sub>4</sub>C-B/Ti-6Al-4V composites was self-similar, *i.e.*, along the initial notch and parallel to the fiber orientation at all the fiber orientations.<sup>3</sup> The fiber orientation was the weakest path for the crack growth. It was shown that the mixed mode FCP for the composite can be expressed by

$$da/dN \propto (\Delta G)^m \quad m \sim 3$$

for a particular fiber orientation, and can be expressed by

$$da/dN \propto [\Delta G/G_F(\theta)]^m$$

for all the fiber orientations where  $G_F(\theta)$  represents the failure strain energy release rate for the composite which was analytically estimated with the help of a simple linear elastic fracture mechanics model.<sup>3,4</sup>

The influence of gaseous environments on the FCP of the longitudinal B<sub>4</sub>C-B/Ti-6Al-4V specimens was also studied.<sup>3,4</sup> It was shown that the humid air enhanced the FCP rates of the composites considerably.<sup>3</sup> It has been documented that a Ti-6Al-4V alloy showing similar microstructure as the matrix alloy in this investigation does not show appreciable difference in the stage II FCP rate for dry and wet air at  $R = 0.1$ .<sup>5</sup> The enhancement of the FCP rates in humid air for the longitudinal B<sub>4</sub>C-B/Ti-6Al-4V composite was there-

fore an interesting observation. The composite system has brittle boron filaments which contribute to the FCP behavior. It has been suggested<sup>6</sup> that humid air weakens the boron filaments in aluminum-boron composites similar to other ceramics. Boron is very much susceptible to humidity embrittlement. Considerable increase in FCP rates was observed for the Al/B composites when humid air was introduced in the vacuum chamber.<sup>6</sup> Since the fiber matrix interfaces and the boron fibers can provide embrittlement sites for the humidity, it is important to study the effect of humidity on the mixed mode FCP behavior of the titanium metal matrix composites.

The titanium metal matrix composite system consists of brittle boron filaments and ductile Ti-6Al-4V matrix. This presents a unique situation for the fatigue crack closure effect. Fatigue crack closure has been studied extensively for isotropic materials.<sup>7-12</sup> During the lower part of the tension-to-tension load cycle, the crack surfaces physically close due to the residual plastic deformation left at the wake of the crack tip. It has been shown for aluminum alloys<sup>12</sup> that in humid air an oxide layer builds up on the crack surfaces. This results in increasing the residual displacement at the edges of the specimen where a plane stress region exists. For the titanium matrix composites, this type of effect can be significant although the oxide formation is much slower. Since the filaments cannot deform plastically, only the matrix contributes to the fatigue crack closure. Thus, in humid air, this plastically deformed matrix can set up radial stress fields. This can result in fiber damage and, in turn, can affect the mixed mode FCP of the titanium metal matrix composites. The purpose of this paper is to study the stress field, fatigue crack closure, and humidity influences on the mixed mode fatigue crack propagation behavior of the titanium metal matrix composites.

## II. EXPERIMENTAL PROCEDURES

Experiments were done on the as-received B<sub>4</sub>C-B and BORSIC reinforced (Ti-6Al-4V) composite materials. The fiber volume fraction was 40 pct. The experimental set-up for the mixed mode fatigue crack propagation (FCP) testing has been described elsewhere.<sup>3,4</sup> Two types of experiments were conducted.

DEEPAK MAHULIKAR is a Research Scientist with Olin Metals Research Laboratories, New Haven, CT 06511. H. L. MARCUS is Harry L. Kent, Jr. Professor of Mechanical Engineering, Department of Materials Science and Mechanical Engineering, The University of Texas, Austin, TX 78712.

Manuscript submitted April 5, 1982.

### A. FCP in Gaseous Environments

To study the influence of gaseous environments on the FCP, experiments were done in environments of different relative humidities. For this purpose, use of a high vacuum system (sorption and ion pumps) connected to an environmental chamber was made. Three sets of experiments were done on B<sub>4</sub>C/B, BORSIC/Ti-6Al-4V composites to study the environmental effects.

In the first set, only longitudinal B<sub>4</sub>C/B(Ti-6Al-4V) specimens were tested in 100 pct RH, dry N<sub>2</sub> gas and  $3.6 \times 10^{-5}$  Pa vacuum environments. These were run at constant  $\Delta P$  with  $R = 0.1$ . The results have been reported.<sup>3</sup>

In the second set, mixed mode FCP in environments of different humidities was studied. Transverse ( $\theta = 90$  deg) and  $\theta = 45$  deg specimens were tested at constant  $\Delta P$  with  $R = 0.1$ , in vacuum, dry N<sub>2</sub> gas, and in humid air (approximately 50 pct RH).

In the third set of experiments on transverse specimens, the fatigue crack was first grown up to  $a/w = 0.4$  in a certain environment (e.g., vacuum) at constant  $\Delta K$  and  $R = 0.1$ . The cycling was then stopped and the specimen was held at the mean load. Another environment of different water vapor pressure was then leaked in with the help of a leak valve. The cycling was then continued in that environment at the same  $\Delta K$  and  $R$ . FCP rates in both environments were recorded along with the crack length at which the transition occurred. Fractography was then carried out to identify the failure mechanisms in the two environments of different relative humidities, and at the transition region. FCP rates were then plotted against the water vapor pressures.

### B. Fatigue Crack Closure and Load Ratio Effects

All the earlier mentioned FCP testing was done at a load ratio of 0.1. At this load ratio considerable amount of fatigue crack closure has been observed in the isotropic materials.<sup>7-12</sup> Fractography of the mixed mode fatigue fractured specimens in humid air revealed some fiber damage in the form of chipping suggesting a squeezing effect of the matrix on the fibers. This strongly suggested a crack closure effect at  $R = 0.1$ . In order to study the crack closure effect and its influence on the failure mechanism in the off-axis specimens, FCP experiments were carried out at the  $R$  value of 0.5 on the transverse as well as the 45 deg specimens in humid air. FCP rates were recorded, and fractography was carried out to identify the failure mechanisms. In a second set of experiments on the B<sub>4</sub>C-B/Ti-6Al-4V transverse specimens the fatigue crack was first grown at a certain load ratio (e.g., 0.1), in humid air. The cycling was then stopped and resumed at a different  $R$ . Fractography was performed on each sample after fracture.

Finally, the fatigue crack closure loads were measured in different environments and at different load ratios. The experimental set-up to measure the crack closure loads is shown in Figure 1. A sensitive clip-on gage was attached on the side of the specimen to record the crack opening displacement. The load displacement curve was recorded at a frequency of 0.02 Hz. Crack closure was measured in two different experiments. In the first experiment, the fatigue crack was initially grown at  $R = 0.1$  in humid air. The cycling was then stopped and the load displacement curve

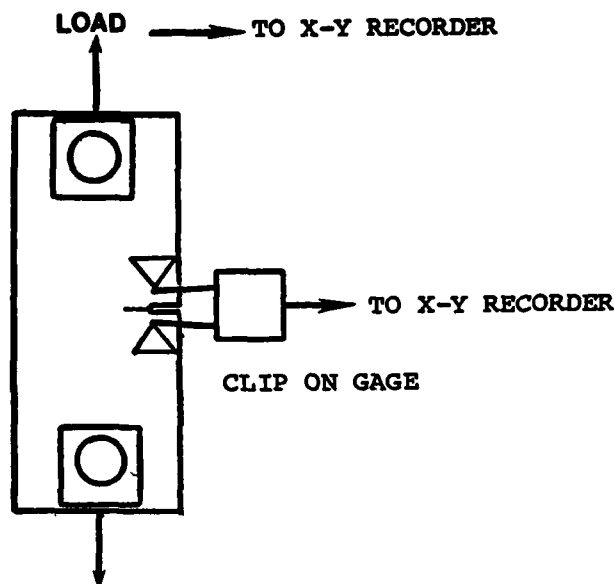


Fig. 1—Experimental set-up for the fatigue crack closure measurements.

recorded at 0.02 Hz. The cycling was then resumed at an  $R$  value of 0.5 and the crack was grown by an increment of 2.5 mm. Crack closure measurements were then carried out. In the second experiment on a transverse specimen, the fatigue crack was initially grown in dry N<sub>2</sub> gas at  $R = 0.1$  and the closure curve was recorded. The cycling was then stopped and humid air was introduced in the chamber. A crack closure measurement was taken at the same crack length. The cycling was then continued in humid air, and another crack closure measurement was made after a crack growth of 0.7 mm.

It should be noted here that the mixed mode FCP data are plotted as  $da/dN \approx (\Delta G)^m$  where  $\Delta G = (\Delta G)_{\text{mode I}} + (\Delta G)_{\text{mode II}}$  and  $\Delta G_I \sim \Delta K_I^2/E_I$  and  $\Delta G_{II} = \Delta K_{II}^2/E_{II}$ .

The  $K$ -calibration used was that for the isotropic materials.<sup>13</sup> It has been shown<sup>14</sup> that the  $K$ -calibration for isotropic materials can be used for longitudinal BORSIC/Ti-6Al-4V specimens. For off-axis specimens, normalization by the anisotropic modulus was done in order to correct for the anisotropic  $G$ -calibration. The details are given in Reference 4.

## III. RESULTS AND DISCUSSIONS

### A. Effect of Humidity on the Mixed Mode FCP

The results for the FCP experiments in environments of different relative humidities on the transverse and  $\theta = 45$  deg specimens are presented in Figures 2 and 3. Figure 2 gives the FCP data for the as-received B<sub>4</sub>C-B/Ti-6Al-4V specimens in vacuum and humid air at  $R = 0.1$ . It is apparent that the FCP rates tend to be higher in humid environments. The FCP rate is significantly higher for the transverse and  $\theta = 45$  deg specimens than the longitudinal specimens. In fact, for the transverse specimen, the FCP rate for the humid air is almost 20 times the FCP rate for the dry N<sub>2</sub> gas at  $R = 0.1$ . Also, humid air FCP recorded a lower value of  $K_{\text{failure}}$  than the dry environments for all



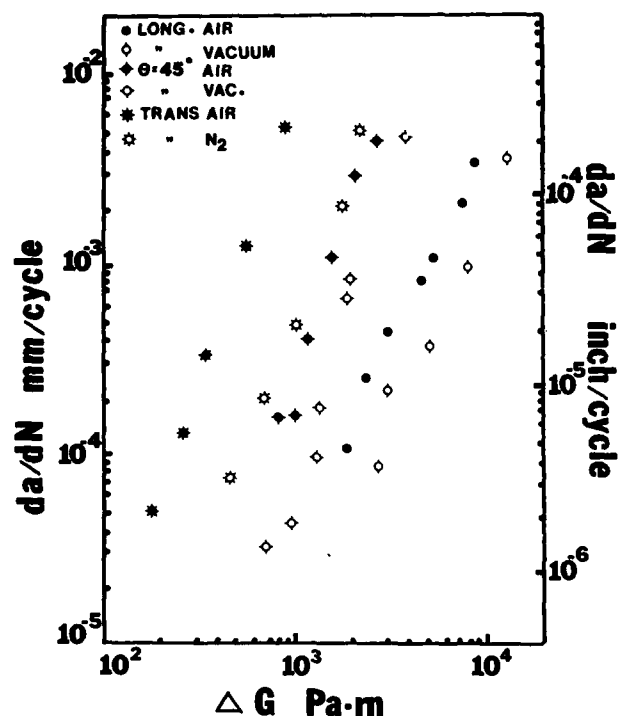


Fig. 2—Mixed mode FCP for the as-received B<sub>4</sub>C-B/Ti-6Al-4V composite in environments of different relative humidities at  $R = 0.1$ .

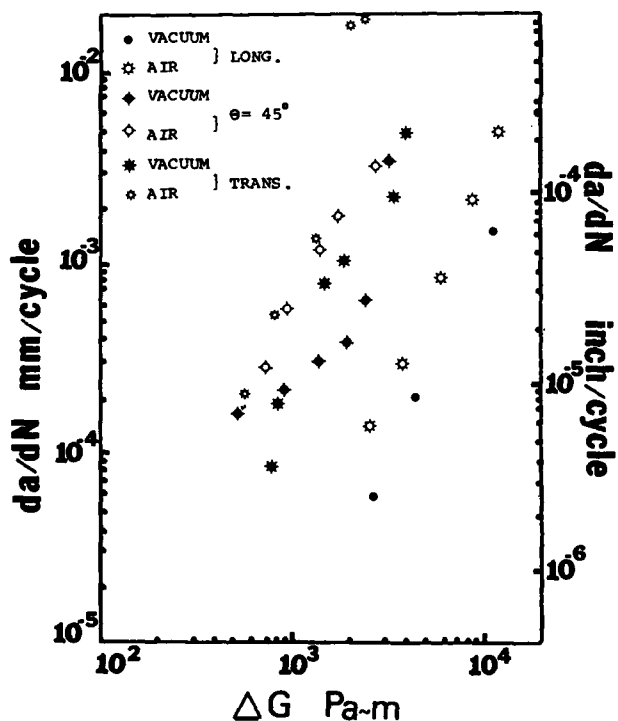


Fig. 3—Mixed mode FCP for the as-received BORSIC/Ti-6Al-4V composite in humid air and vacuum at  $R = 0.1$ .

the orientations. Again, the effect was significant for the transverse and the  $\theta = 45$  deg specimens. Similar observations were made for the BORSIC/Ti-6Al-4V composites



(a)



(b)

Fig. 4—Mixed mode FCP for the as-received B<sub>4</sub>C-B/Ti-6Al-4V specimens: (a) transverse in dry N<sub>2</sub> gas and (b)  $\theta = 45$  deg specimen in vacuum.  $R = 0.1$ .

(Figure 3). FCP rates for both the composite systems in vacuum and dry N<sub>2</sub> gas were similar.

In order to study the humidity effect on the FCP of the titanium MMCs, fractography was carried out on the transverse and 45 deg specimens (Figure 4). The FCP in humid air at  $R = 0.1$  was by fiber splitting, as reported earlier.<sup>3</sup> Some specimens also showed fiber damage in the form of chipping. Since interfaces are the weak links in these composites, it is expected that the humidity would weaken the interfaces in preference to the fibers. The FCP in the dry environments, on the other hand, was by interfacial splitting (Figure 4). This surprising result was also observed for the BORSIC composites.<sup>4</sup> Thus, for  $R = 0.1$  loading the vacuum and the N<sub>2</sub> gas FCP specimens showed predominantly interfacial splitting, and humid air specimens showed predominantly fiber splitting.

If there was a transition in the failure modes from interfacial splitting in dry environments to the fiber splitting in the humid environments, it is expected to occur at a certain water vapor pressure. The third set of experiments was,

therefore, carried out to investigate the water vapor pressure effect on the FCP rates. The data are shown in Figure 5. The  $da/dN$  variation, with respect to the water vapor pressure, shows a rise in the FCP rate at around 100 Pa water vapor pressure. The fractured surfaces of the particular test specimens were examined in an SEM (Figure 6). It is quite evident that a transition in failure mode is present. The vacuum FCP was by interfacial splitting, while at the point of introduction of humidity, a tendency toward fiber splitting is visible. The fiber splitting process is not total, but represents approximately 50 pct of the fracture surface. Since there is a rise in the FCP rate at the transition point, the fiber splitting can be linked to the increased FCP rate in humid air at  $R = 0.1$ . This possibility will be discussed further.

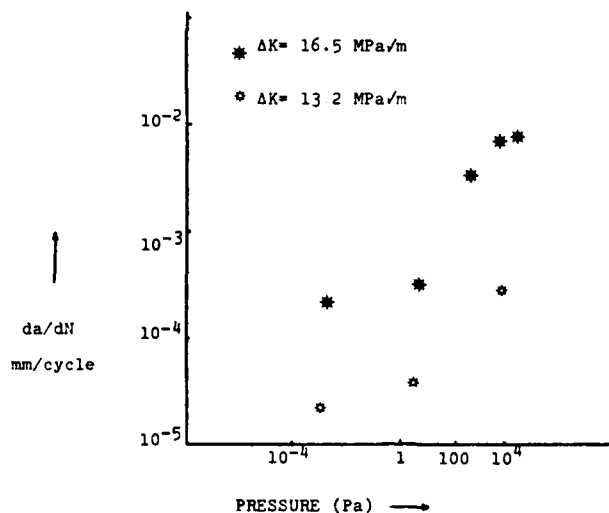


Fig. 5—Variation of the FCP rates for the BORSIC/Ti-6Al-4V transverse specimens with respect to the water vapor pressure at  $R = 0.1$  and constant  $\Delta K$ .

## B. Fatigue Crack Closure: The Load Ratio Effect

Although the strong humidity effect on the FCP behavior of the titanium MMCs was confirmed by fractographic analysis, some interesting questions remained unanswered. It has been stated earlier that some humid air FCP specimens showed fiber chipping in addition to fiber splitting. This suggested a possible hammering or a crack closure effect. Fatigue crack closure is a result of the residual plastic deformation left at the wake of the crack tip. This closure effect can set up stress fields on the fiber. Also, since the specimens were very thin, some mode III stresses are expected to act on the fibers during the lower part of the fatigue cycle during closure. In other words, the fiber splitting mechanism seen for FCP in humid air at  $R = 0.1$  could be a result of an environmentally induced fatigue crack closure.

In order to verify this possibility, FCP experiments were done in humid air at an  $R$  of 0.5. At this load ratio the crack closure effect is minimal. Fractography showed that (Figure 7) although the  $R = 0.5$  FCP was in humid air, the failure was predominantly by interfacial splitting and not by fiber splitting. This pointed to the possibility of an environmentally induced fatigue crack closure effect influencing the mode of failure.

In order to confirm the  $R$  effect, experiments were done in humid air on a single transverse specimen at two different  $R$  values. The fatigue crack was initially grown at  $R = 0.1$  and then at  $R = 0.5$ . Fractography was then carried out to check for the transition in failure modes (Figure 8). Although a clear-cut fiber splitting to interfacial splitting transition is not seen, the two different failure modes (fiber splitting at  $R = 0.1$  and interfacial splitting at  $R = 0.5$ ) are visible. Another experiment was done on a transverse specimen where the fatigue crack was initially grown at  $R = 0.5$  and then at  $R = 0.1$ . Here again, the two different failure modes are seen (Figure 8(b)). An interesting thing can be observed in Figure 8(b). The fibers in the  $R = 0.5$  region

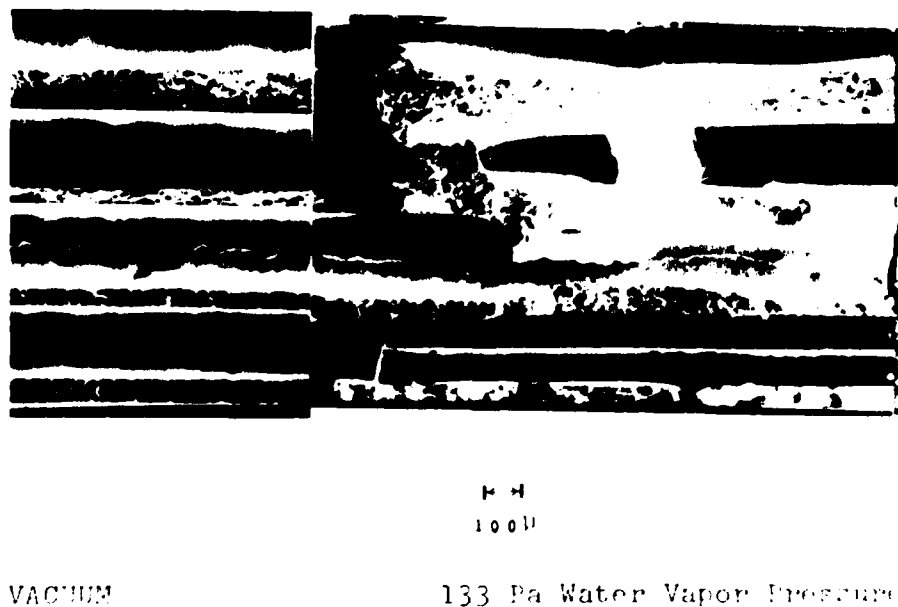


Fig. 6—Fatigue fractured surface of the transverse BORSIC/Ti-6Al-4V specimen showing the transition in failure modes. Interfacial splitting in vacuum to about 50 pct fiber splitting in 133 Pa water vapor pressure.

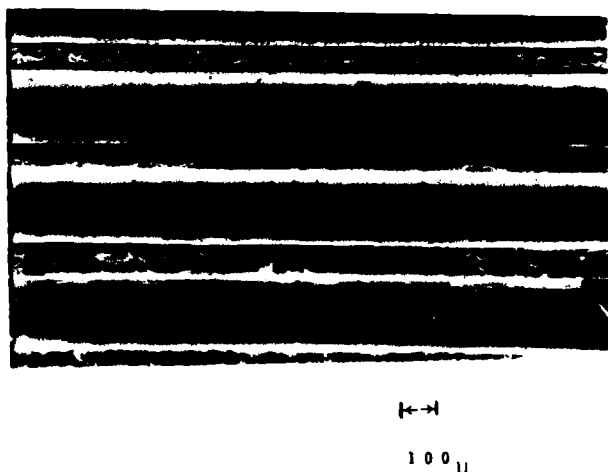


Fig. 7—Fatigue fractured surface of the BORSIC/Ti-6Al-4V specimen at  $R = 0.5$ . The FCP was in humid air.

are cracked (not split), unlike the case when the FCP was entirely at  $R = 0.5$ . This suggests that when the loading was changed to  $R = 0.1$ , the fibers started fracturing. The crack closure-induced mode III stresses started acting on the fibers resulting in the fiber cracking near the crack tip.

The fatigue crack closure measurements at  $R = 0.1$  showed substantial crack closure load (Figure 9), while one at  $R = 0.5$  showed little closure. The effect of humid air at

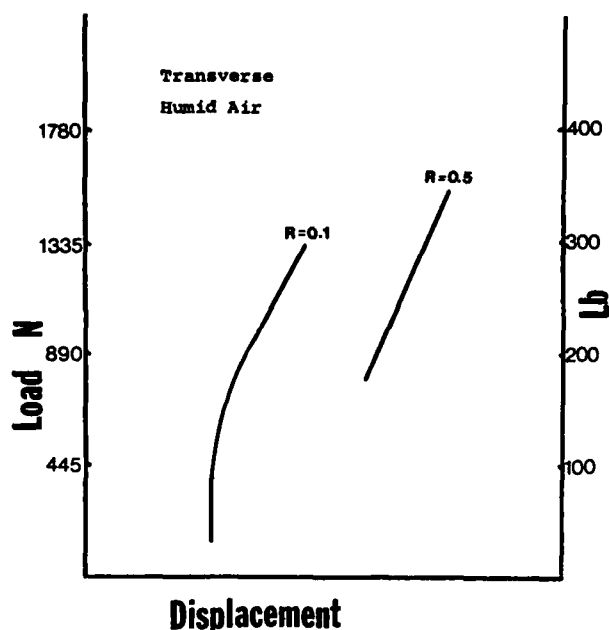


Fig. 9—Fatigue crack closure curves for the as-received B<sub>4</sub>C-B/Ti-6Al-4V transverse specimens.

$R = 0.1$  is established in Figure 10. A very small amount of closure was noticed for  $N_2$  gas environment while introduction of humid air in the environment chamber increased

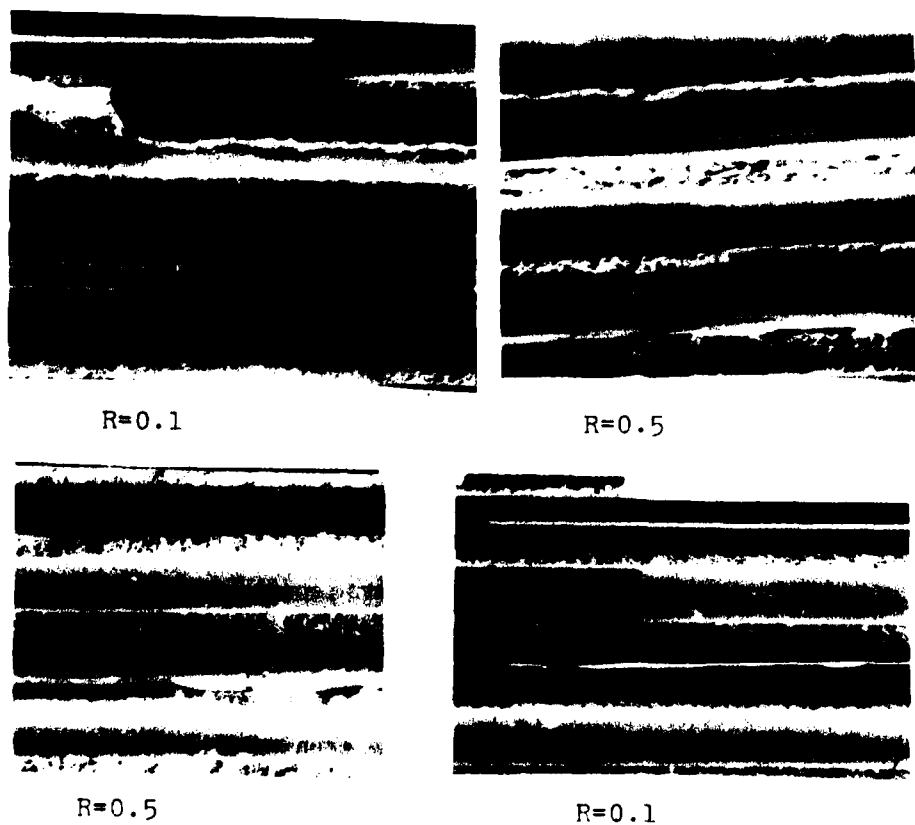


Fig. 8—Fatigue fractured surfaces of the B<sub>4</sub>C-B/Ti-6Al-4V specimens at  $R = 0.1$  and  $0.5$  in humid air. Magnification 47 times.

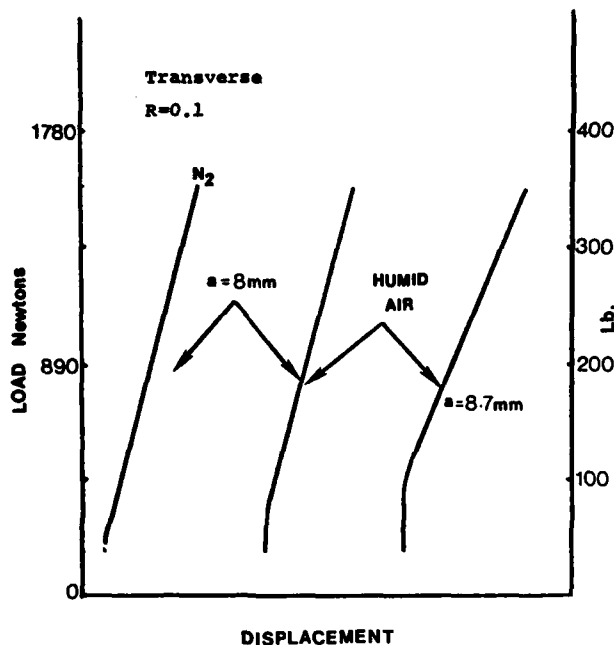


Fig. 10—Fatigue crack closure curves for the B<sub>4</sub>C-B/Ti-6Al-4V transverse specimen in dry N<sub>2</sub> gas and humid air at  $R = 0.1$ .

the closure load. A further increase was noticed when the crack was grown. These experiments confirmed that significant amount of crack closure is observed at  $R = 0.1$  and in humid air. This can be due to the formation of the oxide layer and the mechanical strengthening of the asperities.<sup>12</sup> Therefore, a combination of humidity, high closure loads, and mode III stresses seems to be responsible for the fiber splitting in humid air at  $R = 0.1$ .

From the earlier discussion, it is evident that depending on the loading conditions and environments, either fiber splitting or interfacial splitting is observed in the titanium MMCs. Those conditions and the corresponding failure mechanisms are listed in Table I. Fiber splitting is observed when a combination of humid air, mode III stress, and  $R = 0.1$  loading is present. If any one of these conditions (*i.e.*, crack closure, humid environment, or mode III stresses) is missing, interfacial splitting is observed. It's important to note that the relative ability of these individual conditions to influence the failure mode is not known. It is suggested that the interfacial path of the crack is changed when a combination of humidity, crack closure, and mode III stresses is introduced. The fracture of the brittle fiber will be followed by the surrounding matrix and the FCP will be faster.

#### IV. SUMMARY AND CONCLUSIONS

Room temperature mixed mode fatigue crack propagation studies were carried out on the as-received B<sub>4</sub>C-B and BORSIC fiber reinforced Ti-6Al-4V matrix composites. Effects of gaseous environments on the FCP properties were investigated. Load ratio and fatigue crack closure effects during mixed mode fatigue crack propagation were also studied. The following conclusions were reached:

Table I. Modes of Failure Observed for the Mixed Mode ( $\theta = 45$  and  $90$  deg) B<sub>4</sub>C-B and BORSIC Reinforced Ti-6Al-4V Specimens for Different Environmental and Loading Conditions

Specimens →	As-Received	*Heat Treated
Testing method		(from References 3, 4)
TENSION	Interfacial splitting	Interfacial splitting
Humid air $R = 0.1$	Fiber splitting	Interfacial splitting
Humid air $R = 0.5$	Interfacial splitting	
FCP		
Dry N <sub>2</sub> or Vacuum $R = 0.1$	Interfacial splitting	
Fast fracture	Interfacial splitting	

\*A 500 °C-7 day heat treatment was given to the as-received specimens. The treatment was done for vacuum, as well as for the air environment.

1. Humid air mixed mode FCP rates for the titanium MMCs were greater than the dry environment (vacuum and dry N<sub>2</sub> gas) FCP rates at  $R = 0.1$ . The effect was substantial for the transverse and the 45 deg specimens.
2. The variation of the FCP rate at constant  $\Delta K$  and  $R = 0.1$  with respect to the water vapor pressure showed a rise in the FCP rates at about 100 Pa water vapor pressure. A transition in failure mode was seen from interfacial splitting in the vacuum to fiber splitting in the humid air at 100 Pa water vapor pressure.
3. At  $R = 0.5$  in humid air, the FCP was by interfacial splitting.
4. Significant fatigue crack closure was observed for the humid air FCP at  $R = 0.1$ . Small amounts of crack closure were measured for the FCP in dry N<sub>2</sub> gas at  $R = 0.1$  and for the  $R = 0.5$  FCP in the humid air.
5. The failure mechanism for the mixed mode FCP of the as-received titanium matrix composites in humid air at  $R = 0.1$  was fiber splitting. For all the other conditions (heat treatments, dry environments,  $R = 0.5$ , and the tensile fracture) the failure was by interfacial splitting.
6. The fiber splitting resulted in faster FCP rates.
7. The relative abilities of fatigue crack closure, humidity, and mode III-type of stresses to influence the failure mode are not understood.

#### LIST OF SYMBOLS

$a$	crack length
$d$	diameter or residual displacement
$da/dN$	fatigue crack growth rate
$E$	Young's modulus
$E_I, E_{II}$	axial and transverse modulus, respectively
$G$	strain energy release rate
$G_I, G_{II}$	$G$ for mode I and mode II loading, respectively
$G_c$	critical strain energy release rate
$G_f$	failure strain energy release rate
$\Delta G$	range in strain energy release rate

$K, k$  stress intensity factor  
 $K_I, K_{II}$   $K$  for mode I and II loading, respectively  
 $K_{failure}$  failure stress intensity factor  
 $\Delta K$  range in the stress intensity factor  
 $l, L$  length  
 $m$  exponent  
 $N$  number of cycles  
 $P$  load  
 $\Delta P$  range in the load  
 $r$  radius  
 $R$  load ratio ( $P_{min}/P_{max}$ )  
 MMC metal matrix composites  
 FCP fatigue crack propagation  
 $\theta$  fiber orientation with respect to load axis

#### ACKNOWLEDGMENTS

This research was sponsored by AFOSR Grant #80-0052. Experimental assistance by Norman Williams, Carlos Arias, and Hank Franklin is appreciated. The composite materials were supplied by AFML.

#### REFERENCES

1. A. G. Metcalfe: *Composite Materials*, Academic Press, Broutman and Krock, eds., 1974, vol. 4, pp. 269-318.
2. K. G. Kreider: *Composite Materials*, Academic Press, Broutman and Krock, eds., 1974, vol. 4, pp. 399-471.
3. D. Mahulikar, Y. Park, and H. L. Marcus: *Proceedings of 14th National Symposium on Fracture Mechanics*, ASTM STP 791, J. Lewis and Geo. Sines, eds., Los Angeles, CA, June 1980, p. 579.
4. Deepak Mahulikar: Ph.D. Dissertation, University of Texas at Austin, TX, 1981.
5. J. Chesnutt, A. Thompson, and J. Williams: AFML-TR-78-68, 1978.
6. H. Smith and P. Shahinian: *Corrosion Fatigue*, Proc. Conf. by NACE, O. Devereux and A. J. McEvily, eds., 1972, p. 499.
7. W. Elber: *Damage Tolerance of Aircraft Structures*, ASTM STP 486, 1971, p. 230.
8. A. McEvily: *Met. Sci.*, 1977, vol. 11, p. 274.
9. O. Buck, C. Ho, and H. L. Marcus: *Eng. Fract. Mech.*, 1973, vol. 5, p. 23.
10. V. Bachman and D. Munz: *Eng. Fract. Mech.*, 1979, vol. 11, p. 61.
11. D. Mahulikar, W. Slagle, and H. Marcus: *Scripta Met.*, 1979, vol. 13, p. 867.
12. Deepak Mahulikar and H. L. Marcus: *Fatigue of Eng. Mat. and Structure*, 1981, vol. 3, p. 257.
13. D. Rooke and J. Cartwright: *Compendium of Stress Intensity Factors*, D. P. Rooke and D. J. Cartwright, eds., Hillingdon Press, Uxbridge, 1976, pp. 96-97.
14. J. Auerbuch and H. J. Hahn: *Composite Mat.*, 1978, vol. 12, p. 222.

## APPENDIX E

INFLUENCE OF INTERFACE DEGRADATION AND ENVIRONMENT  
ON THE THERMAL AND FRACTURE FATIGUE PROPERTIES OF TITANIUM  
MATRIX/CONTINUOUS SiC FIBER COMPOSITES

Y.H. Park and H.L. Marcus

Mechanical Engineering/  
Materials Science and Engineering  
The University of Texas  
Austin, Texas 78712

Summary

Interface degradation from thermal cycling in the environments such as vacuum, air and sulfur was investigated using SEM fractography and AES. SEM fractography shows that thermal fatigued specimens produce more damage to the fiber interface than isothermally treated specimens. Liquid nitrogen treatment before thermal treatment gave a consistent result due to the reproducibility of the initial condition of the samples. Based on an elastic solution, the interface stress was estimated and at room temperature, the stress state was tensile with a value of approximately 100 ksi after thermal cycling between 550°C and RT. From the sulfur environment experiments, the interface diffusion coefficient was found to be about  $10^{-8}$  cm<sup>2</sup>/sec and the sulfur concentration vs. distance is expressed as  $\ln C_s = kx$ .

## Introduction

Filamentary metal-matrix composites have generated a considerable amount of interest in the materials field because of their potential applications in dynamic structures. A metal-matrix composite system (MMC) carries certain potential advantages over other non-metal containing composite systems. High strength, modulus, toughness, reproducibility of properties, surface durability, and low notch sensitivity when compared to non-metal matrix composites are just a few of these potential advantages. The MMC systems are characterized by heterogeneity, anisotropy, strengthening by load transfer and interfaces. In order for the full potential of these systems to be used, a better understanding of the above-mentioned effects must be acquired. While analytical tools like stress analysis and linear elastic fracture mechanics are useful in understanding the mechanical properties of matrix and reinforcement together, they cannot be used directly to find out the effect of interface properties on the mechanical response of the system.

Studies have been done to obtain tensile, toughness, and fatigue properties of various MMC systems. Early investigations in fatigue were limited to cyclic stress strain behavior (1). Limited studies have been done on fatigue behavior in environments as a function of temperature. Composite materials present a variety of complex problems in thermomechanical behavior due to differences in properties of matrix and reinforcement. Recently published work (2-7) has treated the case of thermal cycling of composites consisting of elastic reinforcement and a plastic matrix in order to analyze the distribution of stress and strain, obtain expansion properties and investigate possible damage mechanisms. Thermal cycling will obviously be important in many elevated temperature applications. It is, therefore, necessary to know more about the thermal fatigue properties of MMCs and to relate them to the interface chemistry. Better understanding of this relationship can assist in improved composite design and advancement in processing of composites.

The purpose of this investigation is to study the interaction between environment and the metal matrix-fiber interface in MMCs and how this interaction influences the overall performance of the materials under thermal cycling.

A group of the most promising of the current MMCs are SiC, B<sub>4</sub>C and Borsic continuous fibers in the Ti-6Al-4V titanium alloy (8-9). The problems associated with the interface are some of the more significant in the potential application of these MMC systems.

## Experimental

### Materials

The material used in this study is the SiC fiber reinforced titanium alloy (Ti-6Al-4V) matrix composite system. Some of the SiC was on a graphite substrate fiber. Fiber volume fraction was nominally 40%. The diameter of the fibers was about 150  $\mu$ . Four ply panels of 0.033 inches (0.86 cm) were used in the mechanical test. Tensile test and Auger electron microscopy (AES) specimens were cut from the panels by electro-discharge machine (EDM) and polished 1.25 inch (3.2 cm) long by 0.25 inch (6.4 mm) or 0.125 inch (0.32 cm) wide. Samples were tested in both the longitudinal and transverse mode.

## Experiments

1. Isothermal and Thermal Fatigue Tests. Specimens were either isothermally aged at 550°C or thermally cycled between RT and 550°C. The maximum temperature of 550°C was chosen because this approximately represents the upper potential temperature for application of titanium matrix composites. Heating was done in the electrically heated alumina fluidized bath and cooling by removal of the sample from the furnace combined with forced air cooling. A complete cycle was 12 minutes with five minutes for heating or cooling and the remainder for transport. (See Figure 1.)

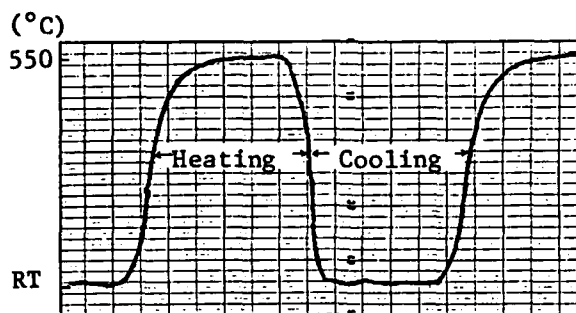


Figure 1 - Typical temperature change during thermal cycle.  
(5 min for heat or cool)

Experiments were also made on samples sealed in a pyrex glass tube in the presence of sulfur vapor and in vacuum. These samples were also thermally fatigued as described above. The possibility of sulfur degradation of the titanium metal matrix composite was investigated to simulate an aggressive operational environment containing sulfur. The oxygen containing environment was established by cycling in air.

2. Tensile Test. All mechanical tensile tests were performed on an Instron at a cross-head speed of 0.5 mm/min. Titanium alloy tabs were glued to both ends of the specimen to prevent premature fracture of the specimen. The samples were smooth and unnotched. A minimum of two specimens were tested for each condition and the results are the average.

3. AES Analysis. The MMC composites were fractured in-situ in a vacuum of  $10^{-10}$  torr ( $1.3 \times 10^{-8}$  Pa). Auger mapping of the fracture surface was made to see the elemental distributions. Several points on the interface were selected for AES and then the surface was Argon-ion sputtered to determine the depth profile of the various elements at the interface.

## Results and Discussion

In an air environment, the longitudinal fracture strength was lower for the thermal cycling specimen than for the as-received or isothermally aged specimen (10). (See Figure 2.) Metallography shows a thicker interface reaction layer for thermal cycling a specimen for a ten day exposure in air resulting in the formation of an alpha case in the titanium matrix around the fibers. An effort was made to minimize the composite degradation due to long thermal treatments in air. The fracture morphologies of the matrix from all conditions were similar.



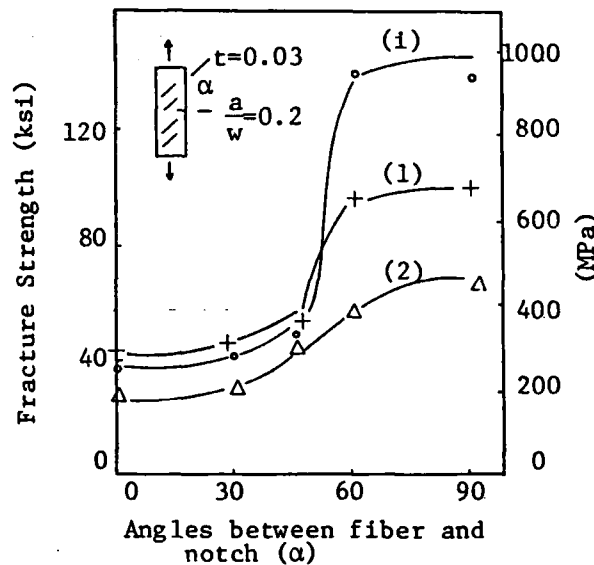


Figure 2 - Fracture strength vs. angles between fiber and notch ( $\alpha$ ) for thermal fatigued at 550°C and 750°C. (1) As-received; (1) TF 550, 10d; (2) TF 750, 10d.

The interface fracture mode showed differences in different environments and thermal conditions (Fig. 3a, b, c). For some cases, the fibers were broken and the interface was branch-cracked. The interface was investigated by AES to see how the interface chemistry is modified and it was found that the oxygen was present over the interface (Fig. 4).

To establish if there was a variation in oxygen distribution due to cyclic or isothermally treated fracture surfaces, Auger mapping techniques were employed. It was shown that oxygen in the specimen thermal fatigued in vacuum was distributed throughout the fracture interface on the matrix side. In the vacuum isothermally treated case a low oxygen content was observed over the fracture surface. Similar Auger maps were obtained for samples thermally cycled in the air. Much higher concentrations of oxygen

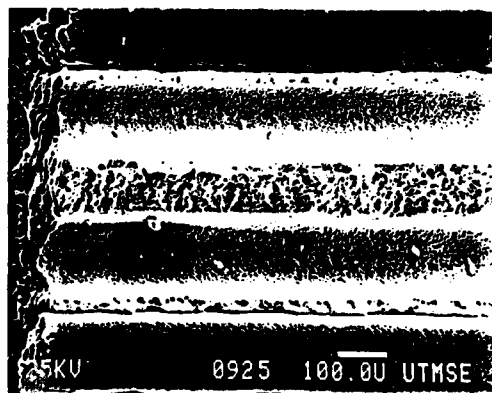


Figure 3(a) - As-received Ti-6Al-4V/SCS (transverse) SEM fractography, unnotched.

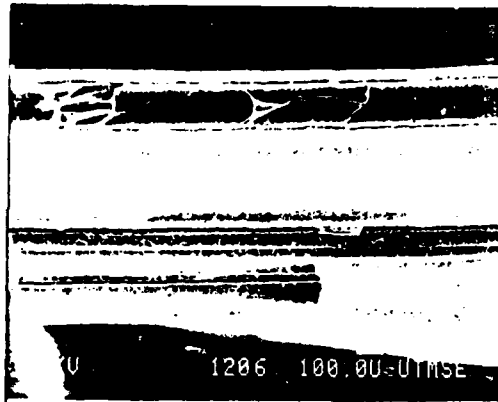


Figure 3(b) - Thermal cycled in sulfur environment Ti-6Al-4V/SCS (transverse) for one day, unnotched.

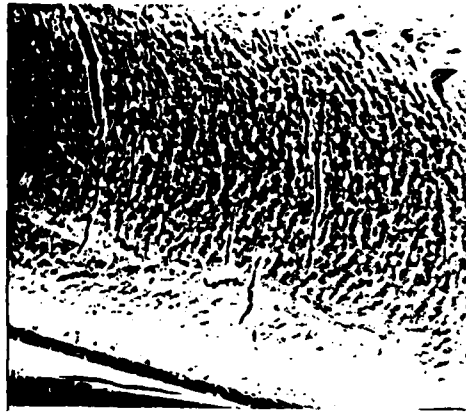


Figure 3(c) - Thermal cycled in sulfur environment Ti-6Al-4V/SCS (longitudinal); unnotched.

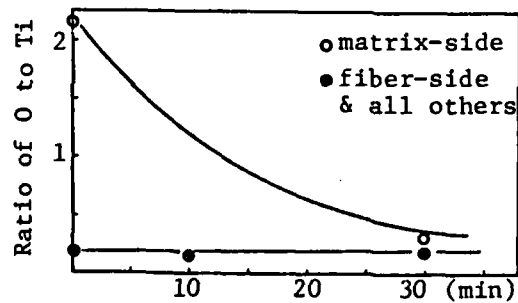


Figure 4 - AES sputtering results on matrix-side and fiber-side interfaces for thermal fatigued samples ( $550^{\circ}\text{C}$ -RT, 10 days). All others include isothermal heat treatment.

were found in the broken fibers and in some matrix areas. Oxygen was present on the interface portion of the fracture surface for the isothermal case but not on the fracture surface through the matrix. It was at lower levels than for the thermal fatigued samples. This increase in fiber and matrix damage indicates that thermal cycling is much more deleterious than isothermal exposure.

It is, therefore, concluded that the interface degradation is mainly due to the diffusion of oxygen down the interface. Damage enhanced diffusion by thermal cycling is also supported from the fact that the oxide thickness of thermal cycling is larger than that of isothermal treatment.

The room temperature fracture surface of the transverse direction sample thermal fatigued in a sulfur environment showed the crack propagated along the interfaces. Branch cracks into the matrix side of the interface were observed in the presence of sulfur. When the extent of the branch cracking is measured relative to the free end and compared to the sulfur analysis, it was found that the sulfur rich area along the interface extended as far as the branch cracks. Those branch cracks were not found for isothermally exposed specimens or for the thermal fatigued specimens beyond the sulfur diffusion distance.

To determine the origin of the enhanced degradation of the interface from thermal cycling, the thermally induced stress state due to the difference of thermal expansion coefficient between the Ti-6Al-4V matrix and the SiC fibers was analyzed as follows. A plane strain elasticity analysis (11) that had been derived earlier (12) to explain the matrix deformation due to thermal stresses is used as a basis for the model. The model, shown in Fig. 5, treats the fiber of radius  $a$  and its surrounding shell of matrix of outer radius  $b$  as an independent entity. The subscripts  $m$  and  $f$  denote the matrix and the fiber respectively.  $\nu$  is the poisson's ratio,  $\alpha$  the coefficient of expansion,  $E$  the Young's modulus and  $\Delta T$  the temperature cycling range.

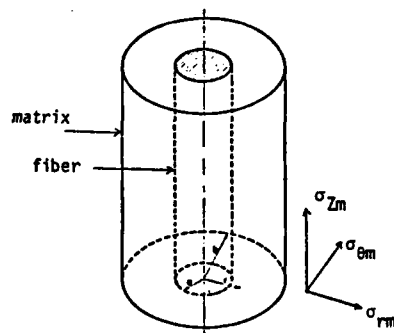


Figure 5 - The model of a unit composite of a fiber and a matrix shell.

Poritsky's elastic solution gives the principal thermal stresses in the matrix as:

$$\sigma_r = \Gamma \left( 1 - \frac{b^2}{r^2} \right) \quad (1)$$

$$\sigma_{\theta} = \Gamma \left(1 + \frac{b^2}{r^2}\right) \quad (2)$$

$$\sigma_z = K \quad (3)$$

where

$$\Gamma = - \left[ \frac{E_m (\alpha_m - \alpha_f) \Delta T \left(\frac{a}{b}\right)^2}{1 + \left(\frac{a}{b}\right)^2 (1 - 2\nu) \left\{ \left(\frac{b}{a}\right)^2 - 1 \right\} \frac{E_m}{E_f}} \right]$$

and

$$K = \frac{\Gamma}{\left(\frac{a}{b}\right)^2} \left[ 2\nu \left(\frac{a}{b}\right)^2 + \frac{1 + \left(\frac{a}{b}\right)^2 (1 - 2\nu) + \left(\frac{a}{b}\right)^2 (1 - 2\nu) \left\{ \left(\frac{b}{a}\right)^2 - 1 \right\} \frac{E_m}{E_f}}{1 + \left\{ \left(\frac{b}{a}\right)^2 - 1 \right\} \frac{E_m}{E_f}} \right]$$

The room temperature stresses due to the thermal cycling of a Ti-6Al-4V/SiC composite system between RT and 550°C are calculated to be  $\sigma_r = -56.3$  ksi,  $\sigma_{\theta} = 101.4$  ksi, and  $\sigma_z = 102$  ksi. During thermal cycling it is the cooling cycle that produces the major thermal fatigue damage. The reason is that the cooling cycle induces longitudinal and tangential tensile stress in the matrix. During the heating cycle, the stress states are reversed and are small due to the elastic behavior (Fig. 6).

From the above argument, it is reasonable to propose that tensile stress states are induced for every cycle in the matrix side of the interface whose magnitudes are estimated from Poritsky's elastic analysis.

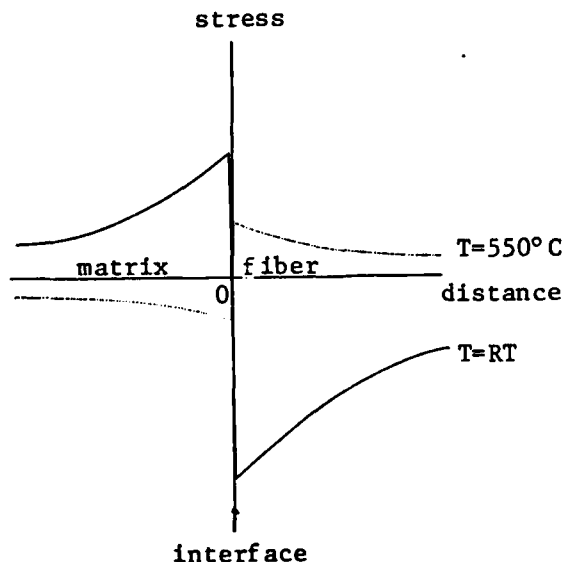


Figure 6 - Schematic representation of stress variation with temperature near the interface.

Cyclic tensile stress, now, combines with environment to speed up the formation of oxide or sulfide and degrade the interface.

To ensure a reproducible stress state during the thermal cycling, the specimen was quenched to LN<sub>2</sub> temperature for five minutes. From the calculation based on thermal expansion difference with Poritsky's solution and the composite fabrication temperature of 800°C with no stress at the interface at 800°C, the room temperature interface stress was estimated and shown in Fig. 7 (14).

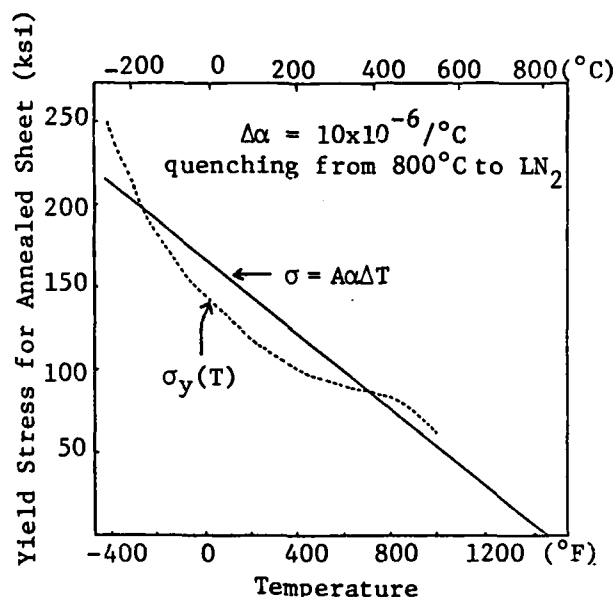


Figure 7 - Effect of temperature on the tensile yield strength of annealed Ti-6Al-4V sheet (dotted) (14).

The diffusion of sulfur can be formulated as follows. The distance from the end of the specimen to the limit of detectable sulfur down the interface is the diffusion distance of sulfur (Fig. 8). The sulfur was detected along the interface using AES. The measured diffusion distance was approximately 400 $\mu$  after 24 hrs thermal treatment. A diffusion coefficient was estimated from the one-dimensional diffusion equation with an infinite source at the boundary (13). This gives a characteristic diffusion distance,  $x = \sqrt{Dt}$ . Diffusivity was then calculated to be on the order of 10<sup>-8</sup> cm<sup>2</sup>/sec implying interfacial diffusion. In the isothermal experiment with the sulfur environment at temperature for four times the temperature period in the thermal fatigued case much less S is diffused down the boundary as shown in Fig. 9. SEM fractography also confirms the sulfur effect by showing the branch cracks. The branch cracks extend an equivalent distance to the AES sulfur detection distance as discussed earlier.

When the sulfur analysis was made its concentration decreases monotonically as the distance from the edge. The plot of logarithm of sulfur concentration vs. distance gave a straight fitting, shown in Fig. 10 and the following expression is appropriate.

$$\ln C_s = kx$$

This is the expression for diffusion in a semi-infinite medium,  $x > 0$ , when the boundary is kept at a constant concentration and the initial concentration throughout the medium is zero.



Figure 8 - Thermal cycled in sulfur environment Ti-6Al-4V/SCS (transverse) for one day; magnified the cracks from thermal fatigue, unnotched.

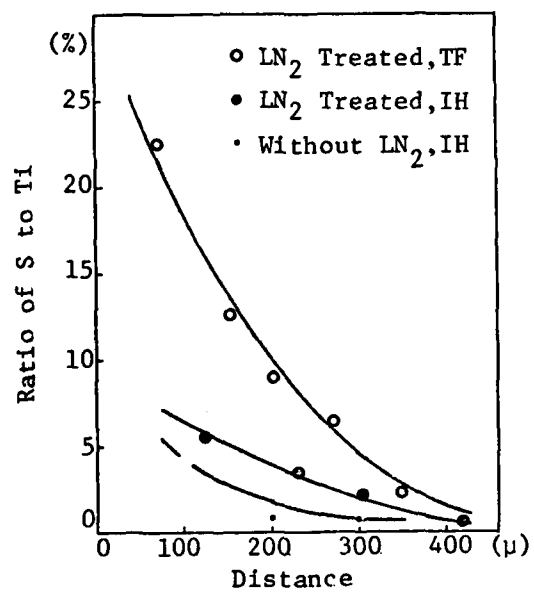


Figure 9 - AES analysis of sulfur along the matrix-side interface.

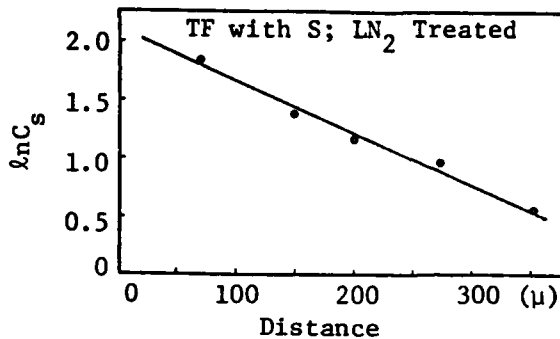


Figure 10 - Logarithmic fitting of sulfur concentration along the matrix side interface.

- More rigorous analysis is now in progress. In the literature, no quantitative analysis of the thermal cycling and its effect on the interface damage in the MMC system is available.

### Conclusions

Interface degradation from thermal cycling in the environments such as vacuum, air and sulfur was investigated using SEM fractography and AES. SEM fractography shows that thermal fatigued specimens produce more damage to the fiber interface than isothermally treated specimens. Liquid nitrogen treatment before thermal treatment gave a consistent result due to the reproducibility of the initial condition of the samples. Based on an elastic solution, the interface stress was estimated and at room temperature, the stress state was tensile with a value of approximately 100 ksi after thermal cycling between 550°C and RT. From the sulfur environment experiments, the interface diffusion coefficient was found to be about  $10^{-8}$  cm<sup>2</sup>/sec and the sulfur concentration vs. distance is expressed as  $\ln C_s = kx$ .

### Acknowledgments

The authors would like to acknowledge discussions with Deepak Mahulikar and Michael Schmerling. This research was supported by the Air Force Office of Scientific Research under grant AFOSR 80-0052.

### References

1. J.R. Hancock, Composite Materials (Fracture and Fatigue), vol. 5, pp. 371-412; Academic Press, 1974.
2. G. Garmong, Metallurgical Trans. 5A (1974) pp. 2183-2190.
3. G. Garmong, Metallurgical Trans. 5A (1974) pp. 2191-2197.
4. G. Garmong, Metallurgical Trans. 5A (1974) pp. 2199-2205.
5. G.C. Olson and S.S. Tomkins, Failure Modes in Composites IV, TMS-AIME, pp. 1-21, 1979.

6. K.K. Chawla, Journal of Materials Science 11 (1976) pp. 1567-1569.
7. J. Billingham and S.P. Cooper, Metal Science 15 (1981) pp. 311-316.
8. A.G. Metcalfe, Composite Materials (Metallic Matrix Composites), vol. 4, pp. 269-327; Academic Press, 1974.
9. I. Ahmad, D. Hill and W. Heffernan, Proceedings of International Conference on Composite Materials, TMS-AIME, p. 85, 1976.
10. Y.-Park, D. Mahulikar and H.L. Marcus, "Mixed Mode Crack Propagation," pp. 385-395, in Mixed Mode Crack Propagation, G.C. Sih and P.S. Theocaris, eds.; Sijthoff & Noordhoff, Rockville, MD, 1981.
11. H. Poritsky, Physics 5 (1934) p. 406.
12. K.K. Chawla, Proceedings of Fourth Bolton Landing Conference, p. 435, 1975.
13. J. Crank, The Mathematics of Diffusion, Oxford Press, 1979.
14. Titanium Handbook, 1972, MCIC.



## APPENDIX F

FATIGUE CRACK GROWTH BEHAVIOR OF Ti-6Al-4V METAL  
MATRIX/CONTINUOUS SiC AND B<sub>4</sub>C/B FIBER COMPOSITES

Y.H. Park<sup>1,2</sup>, D. Narayan<sup>1</sup>, M. Schmerling<sup>3</sup> and  
H.L. Marcus<sup>4</sup>  
Dept. of Mechanical Engineering/Materials Science  
and Engineering, The University of Texas at Austin

1. Graduate Students, 2. now with Materials Research  
Corporation, Orangeburg, N.Y., 3. Senior Research  
Scientist and 4. Harry L. Kent Professor of Mechanical  
Engineering.

### Abstracts

The fatigue crack growth (FCG) behavior of SiC and  $B_4C/B$  reinforced Ti-6Al-4V metal matrix composites loaded in the transverse direction as a function of modifications of the interface between the fiber and matrix was studied. The interface chemistry, modified by sulfur diffusion during thermal cycling treatment, changed the FCG in air, dry  $N_2$  and hydrogen environments when compared with the as-received specimens.

The FCG rates tend to be higher in humid environment. The SEM fractography indicates that the FCG in humid air was by an increased amount of fiber splitting. The FCG in dry  $N_2$  environment was more often by interface debonding with some fiber splitting and fiber fracture. The FCG rates in dry hydrogen for both as-received and heat treated specimens were intermediate between the observed rates for dry  $N_2$  and humid air.

During FCG in lab air, the sulfur enriched interface of the specimens thermal cycled in a sulfur environment reacts with the humidity in air to degrade the interface cohesion resulting in complete separation of the interface from the matrix and the fiber at low strains. This inability of the interface to sustain any strain further increases the FCG rates in the matrix. The results demonstrate the interface does transfer load during fatigue cycling in either an inert environment or if the interface has a minimal amount of impurities.

## Introduction

The fatigue behavior of metal matrix composites (MMCs) differs from that of unreinforced metals in several ways. MMCs exhibit various failure modes such as debonding of the interface between the fiber and the metal matrix, fiber splitting, fiber fracture, matrix fracture, which occur independently or interdependently.

Because of their high strength to weight ratio, high modulus and toughness, titanium MMCs have long been considered for applications in dynamic structures. However, like other MMCs titanium MMCs are characterized by anisotropy, heterogeneity and interface. Tensile properties of titanium MMCs reinforced with continuous SiC, Borsic and  $B_4C/B$  fibers have been studied<sup>1-3</sup> and the results indicated that the mechanical properties are dependent on the interface or the reaction zone between the fiber and the metal matrix.

In this study, various experiments were performed to study the effect of temperature and other environments on the interfaces and the mechanical properties of the titanium metal matrix composites reinforced with SiC and  $B_4C/B$  fibers.

The mechanical properties studied are transverse loading residual strength after thermal exposure and fatigue crack growth (FCG) under Mode I loading after thermal treatment. The condition of the matrix-fiber interface as a function of the above treatments was characterized with both scanning Auger microscopy (SAM) and scanning electron microscopy (SEM). The fiber interface chemistries were modified by thermal treatment in oxygen and sulfur bearing environments.

## Experimental

### Materials

The metal matrix composite (MMC) systems used in this study were SiC or B<sub>4</sub>C/B continuous fiber in a Ti-6Al-4V alloy matrix. The composite panel was four ply, approximately 0.84 mm thick. The composite has a fiber volume fraction of about 40 % with a diameter of 150  $\mu$ m. Detailed specimen preparation appears in Ref. 4.

### Heat Treatments

With the intention of studying the effect of a modified interface on the fatigue behavior and failure modes of the titanium MMCs, heat treatment in the sulfur environment was employed. Specimens were thermal cycled in a sulfur rich atmosphere between 25°C and 550°C in a fluidized bath furnace filled with alumina particles<sup>4</sup>. An automatic timing device was used to maintain heating and cooling periods of five minutes at each temperature. All specimens were placed in pyrex tubes with dry powder sulfur, evacuated to a pressure of 10<sup>-5</sup> torr and sealed. Thermal cycling was carried out for a period of 84 hrs. for a long sulfur diffusion distance<sup>4</sup>.

### Fatigue Crack Growth (FCG) Testing

All FCG testing was performed on transverse specimens. Edge notched specimens with an initial notch length, the specimen width and the specimen length of 6, 25 and 62.5 mm, respectively, were used. Aluminum doublers were glued at the ends using an epoxy glue to prevent load point failure. Fatigue cycling was performed on an MTS closed loop electrohydraulic system in the tension-tension mode, between 20 lb and 200 lb at a frequency of 2 Hz. Fatigue crack growth was monitored

visually with the aid of several equidistant vertical lines normal to the notch inscribed on the specimen surface. Stress intensity calculations<sup>5</sup> showed the thickness requirements for the plane strain FCG testing, as specified in the ASTM Standards<sup>6</sup>, could only be satisfied up to a  $K$  value of  $11 \text{ MPa(m)}^{\frac{1}{2}}$ . Actual  $K$  values ranged from about 0.9 to  $27 \text{ MPa(m)}^{\frac{1}{2}}$  with a load ratio of 0.1.

The first set of experiments was performed on both as-received and heat treated transverse specimens in laboratory air of approximately 50 % R.H. In addition, to study the effects of gaseous environments on the FCG, experiments were also performed in atmospheres of dry nitrogen and dry hydrogen. For this purpose, a high vacuum system (sorption and ion pumps) connected to an environment chamber was employed. The chamber was evacuated to  $5 \times 10^{-4} \text{ Pa}$  ( $4 \times 10^{-6} \text{ torr}$ ) and backfilled with the gas of interest.

Finally, all the fatigue fractured surfaces were viewed in a JEOL 35 SEM to determine the failure paths and mechanisms and the effects of interface modification and gaseous environments on the failure mode. Multiple specimens were run in each set of experiments to permit duplication of results.

## Results and Discussion

### FCG for SiC/Ti-6Al-4V Composites

The first set of experiments was carried out on both as-received and thermal cycled SiC/Ti-6Al-4V specimens in lab air of 50 % R.H. It was observed that the rate of crack growth in the heat treated specimens exceeded that of the as-received specimens slightly, indicating that the thermal cycling in sulfur environment may be instrumental in degrading the fatigue resistance. The as-received specimen showed the presence of both fiber splitting and interfacial debonding while the heat treated specimens exhibited only interfacial debonding. These observed fracture modes are in agreement with Mahulikar's<sup>5</sup> results for Borsic/Ti-6Al-4V composites, where he noticed a transition from fiber splitting for the as-received condition to interfacial splitting for the heat treated condition.

To investigate the effect of different gaseous environments on the FCG and failure mode, room temperature experiments were performed in dry N<sub>2</sub> gas. Both the as-received and thermal cycled specimens showed considerably lower FCG rates in N<sub>2</sub> than in humid air (Figs. 1 and 2). This observation indicates that it is the reaction of sulfur with humid air, more than likely the dissociated hydrogen, that results in further degradation of the fiber matrix interface and consequent reduction in fatigue crack growth resistance. The presence of an inert atmosphere such as nitrogen renders the sulfur from the thermal cycling treatment relatively ineffective in increasing the FCG rates (Fig. 2). Fractography on both sets of fracture surfaces revealed the presence of fiber splitting. This is in contrast to Mahulikar's<sup>5</sup> results for Borsic/Ti-6Al-4V where fiber splitting was seen only in humid air. The difference can be attributed to better fiber matrix bonding in the SiC composites or that the SiC are more brittle than the Borsic fibers, causing fiber splitting in

preference to debonding from the matrix.

The third set of experiments was performed in dry gaseous  $H_2$  to evaluate the hydrogen effect. The FCG rates of both the as-received and thermal cycled specimens were intermediate between the observed rates for dry  $N_2$  and humid air. (Figs. 1 and 2). The heat treated specimens slightly exceeded that of the as-received. Fractography revealed the presence of some fiber splitting in each case, which can be explained by reasoning similar to the dry  $N_2$  case.

In all cases the fiber direction along the interface or through the split fibers was found to be the least resistant path for the FCG in the transverse specimens. In the case of mixed mode loading<sup>5</sup>, the FCG was in the direction of the fiber, indicating that the direction of the fiber-matrix interface was the least resistant path for crack propagation.

#### FCG for $B_4C/B/Ti-6Al-4V$ Composites

Figure 3 shows the results for the FCG tests in a transverse direction for as-received  $B_4C/B/Ti-6Al-4V$  specimens and then cyclically loaded at a load ratio of 0.1, in lab air and in gaseous nitrogen. FCG data for the annealed  $Ti-6Al-4V$  alloy in air is also included for comparison. The FCG of  $Ti-6Al-4V$  alloy in air and inert dry argon at room temperature yield almost identical cyclic crack growth rates<sup>7</sup>.

When the data are presented in a  $da/dN$  vs.  $\Delta K$  plot, as shown in Fig. 3 it is clear that the stage II FCG of the composites along with a  $Ti-6Al-4V$  alloy can be expressed by Paris' law

$$da/dN \propto \Delta K^m$$

The slope (m) is identical for the  $Ti-6Al-4V$  alloy and the composites

tested in the transverse direction. The results for composites show little difference in FCG between this study and Mahulikar's<sup>5</sup>.

The fractography, shown in Fig. 4, indicates that the FCG in humid air was by an increased amount of fiber splitting as reported here and from Mahulikar's<sup>5</sup>. FCG in dry  $N_2$  environment, on the other hand, was more often by interface debonding with some fiber splitting and fiber fracture (Fig. 5)

Specimens thermal cycled in sulfur show higher FCG rates in lab air than the as-received sulfur free specimens. The slope (m) is greater for those specimens. When sulfur is at the interface following thermal cycling in the sulfur environment, the FCG rate in humid air increases and is accompanied by interface debonding. SEM fractography in Fig. 6 shows well-defined interface debonding.

The FCG results for the samples thermal cycled in a sulfur environment and tested in dry  $N_2$  gas indicated a slight decrease in growth rate with the same slope as the dry  $N_2$  FCG rates of the as-received specimens. The fractography of  $N_2$  tested sulfur enriched  $B_4C/B/Ti-6Al-4V$  composites, shown in Fig. 7, shows fracture modes such as fiber splitting, fiber fracture and matrix fracture similar to those for FCG in  $N_2$  of as-received specimens. This similar fracture mode correlates with the similar value of m with the as-received specimen.

When  $\Delta K$  is normalized using the rule of mixtures with the elastic modulus of the respective materials ( $E_{\text{composite}} = 140 \text{ GPa}$  ( $20 \times 10^6 \text{ psi}$ ),  $E_{Ti} = 116 \text{ GPa}$  ( $16.8 \times 10^6 \text{ psi}$ )) to have comparable crack opening displacement (COD)<sup>8</sup>, the composite FCG is even greater than that of Ti-6Al-4V matrix with the slopes (m) virtually unchanged, as shown in Fig. 8. The fiber directions along the interface or through split fibers are the least resistant path for the transverse FCG. This can be explained that the brittle fiber and interface is not carrying much of the stress. If it is assumed that all the cyclic stress and COD are accommodated by the matrix material the equivalent  $\Delta K/E$  would translate the results to closely match the Ti-6Al-4V results



with the exception of the sulfur/humid air measurements. The amount of translation of  $\Delta K_{tr}$  will be  $1.74K_{composite}$  since the load is carried by matrix with a volume fraction of 60 % for the transverse specimen (Fig. 9).

The sulfur enriched interface of the specimen thermal cycled in sulfur reacts with the humidity in the air during FCG in lab air to degrade the interface cohesion resulting in complete separation of the interface between the matrix and the fiber at low strains. This inability of the interface to sustain any significant strain further increases the fatigue crack growth rate in the matrix. The increase in the value of the slope may be due to the degradation of the interface by titanium sulfides creating a volume of brittle materials.

#### A Model of the Failure Mechanism for the Transverse FCG.

The results presented here demonstrate that the interface between the matrix and the fiber does transfer load during fatigue cycling in either an inert environment or if the interface has a minimal amount of impurities. On the basis of the results of the experiments described above, a model for the failure mechanism for the FCG of the transverse titanium MMCs can be proposed. The model is schematically shown in Fig. 10. Only the matrix deforms plastically. Due to the high degree of anisotropy for the MMCs, the plastic zones are elongated in the direction of the fibers. Thus the fibers in front of a sharp crack can be assumed to be surrounded by a plastic sheath of the matrix. During cycling loading of as-received materials in humid air, the matrix plastically deformed under tension closes over the fibers which do not deform plastically ( $\epsilon_{fiber} = 0$ ). When the interface transfers the load the fibers split as described earlier (Fig. 10).

In the case of the sulfur enriched specimen, fatigue cycling in humid air reduced the cohesion of the interface due to hydrogen-sulfur interactions. The stress is then totally carried by the matrix and necking forms in the matrix along side of the interface between

between the two adjacent fibers. This could be initiated from the rough crack surface due to the interaction of the titanium sulfide and the humidity in air. Such rough surfaces come from the radial and branch cracks, as shown in Fig. 11. The fracture mode in the vicinity of the fibers is totally interface debonding and the fibers are undamaged as shown in Fig. 6.

### Summary and Conclusion

The effect on the fatigue crack growth (FCG) behavior of the SiC and B<sub>4</sub>C/B reinforced Ti-6Al-4V metal matrix composites (MMCs) by the modification of the interface between the fiber and the matrix by isothermal and thermal cycled treatments was studied. The thermal cycling and isothermal treatments were carried out in environments of air, sulfur and vacuum.

The FCG results demonstrated that the interface transferred the load during fatigue cycling in either an inert environment or if the interface has a minimal amount of impurities. In the case of the sulfur enriched interface, the humid air FCG environment reduced the cohesion of the interface resulting in the applied load being totally carried by the matrix. This led to an increased FCG rate with a higher value of the Paris exponent (m). Without the enhanced sulfur at the interface the Paris exponent remained constant although the FCG rate nominally increased in humid air environment.

The nonenvironmental FCG rate change is largely explainable in terms of the volume fraction of the matrix relative to FCG of the monolithic Ti-6Al-4V matrix material.

### Acknowledgement

This research was sponsored by AFOSR, under contract 80-0052. The titanium metal matrix composites were supplied by the AFML.

References

1. A.G. Metcalfe, in Composite Materials, vol.4., Academic Press, 1974, p. 269.
2. B.R. Collins, et al., in Failure Modes in Composites I, I.J. Toth, et al., (eds), AIME, 1973, p. 103.
3. D.S. Mahulikar, Y.H. Park and H.L. Marcus, in Proceedings Greece/U.S.A. Mixed Mode Fracture Conference, Athens, Greece, 1980.
4. Y.H. Park, PhD Dissertation, at the University of Texas at Austin, May 1983.
5. D.S. Mahulikar and H.L. Marcus, to be published in Metall. Trans. A.
6. W. Brown and J. Srawley, ASTM STP 410, ASTM, 1969.
7. R.J. Bucci, et al., ASTM STP 513, ASTM, 1972, p. 125.
8. R.W. Hertzberg, in Deformation and Fracture Mechanisms of Engineering Materials, John Wiley, 1976, p. 514.

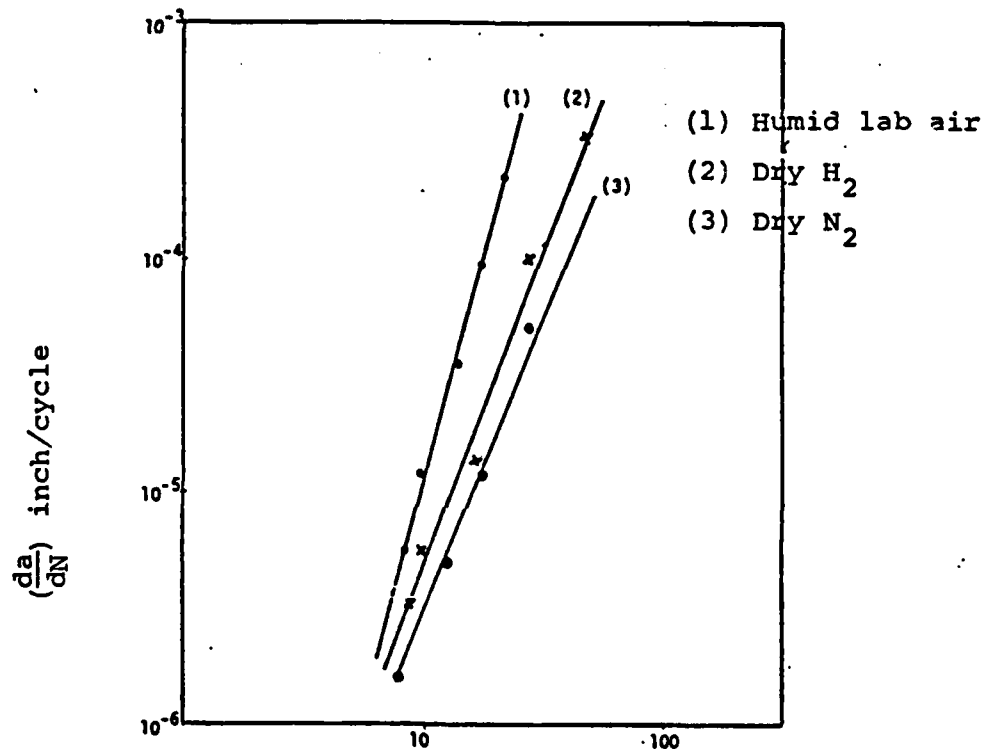


Figure 1. FCG of as-received transverse SiC/Ti(6Al-4V) specimens in various gaseous environments.

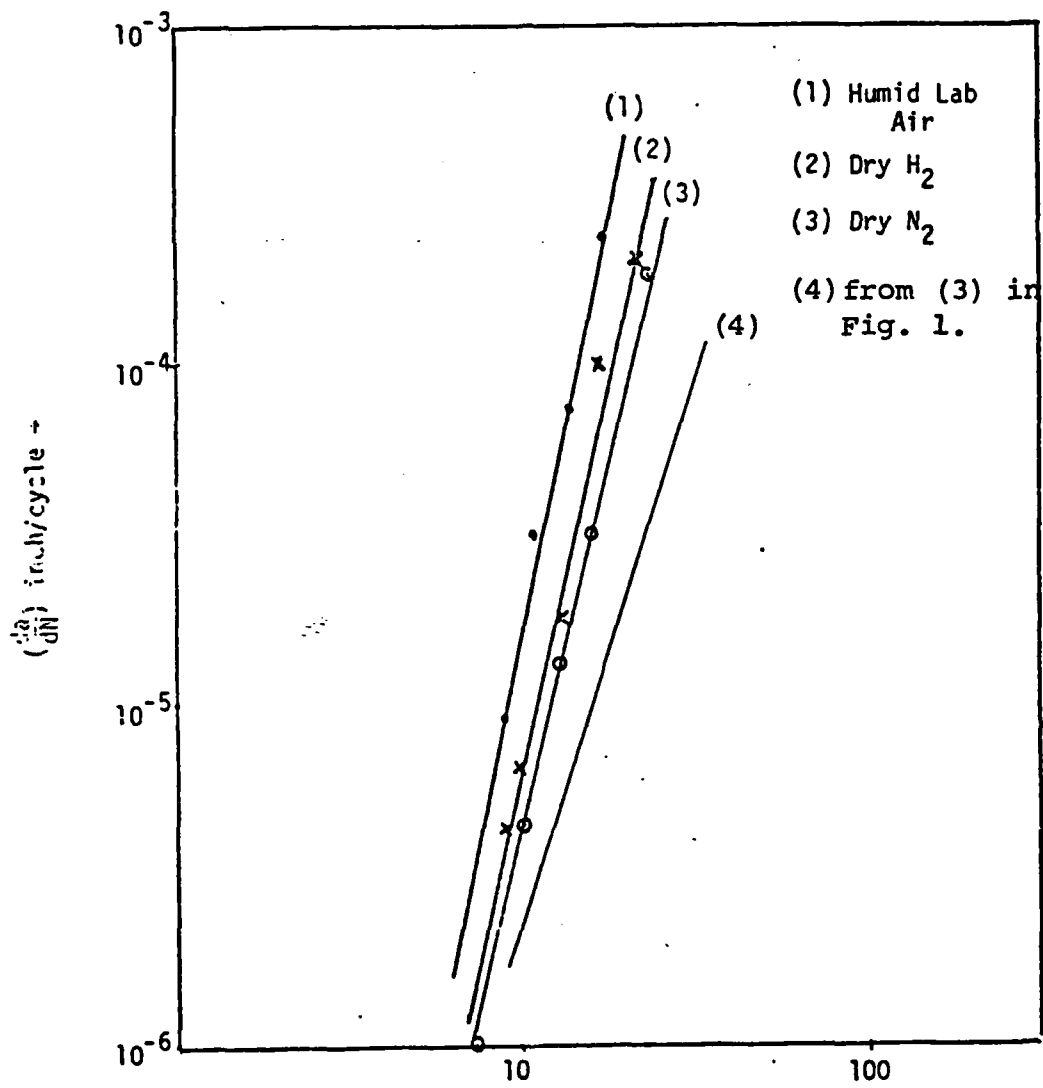


Figure 2. FCG of thermal cycled transverse SiC/Ti(6Al-4V) specimens in various environments.

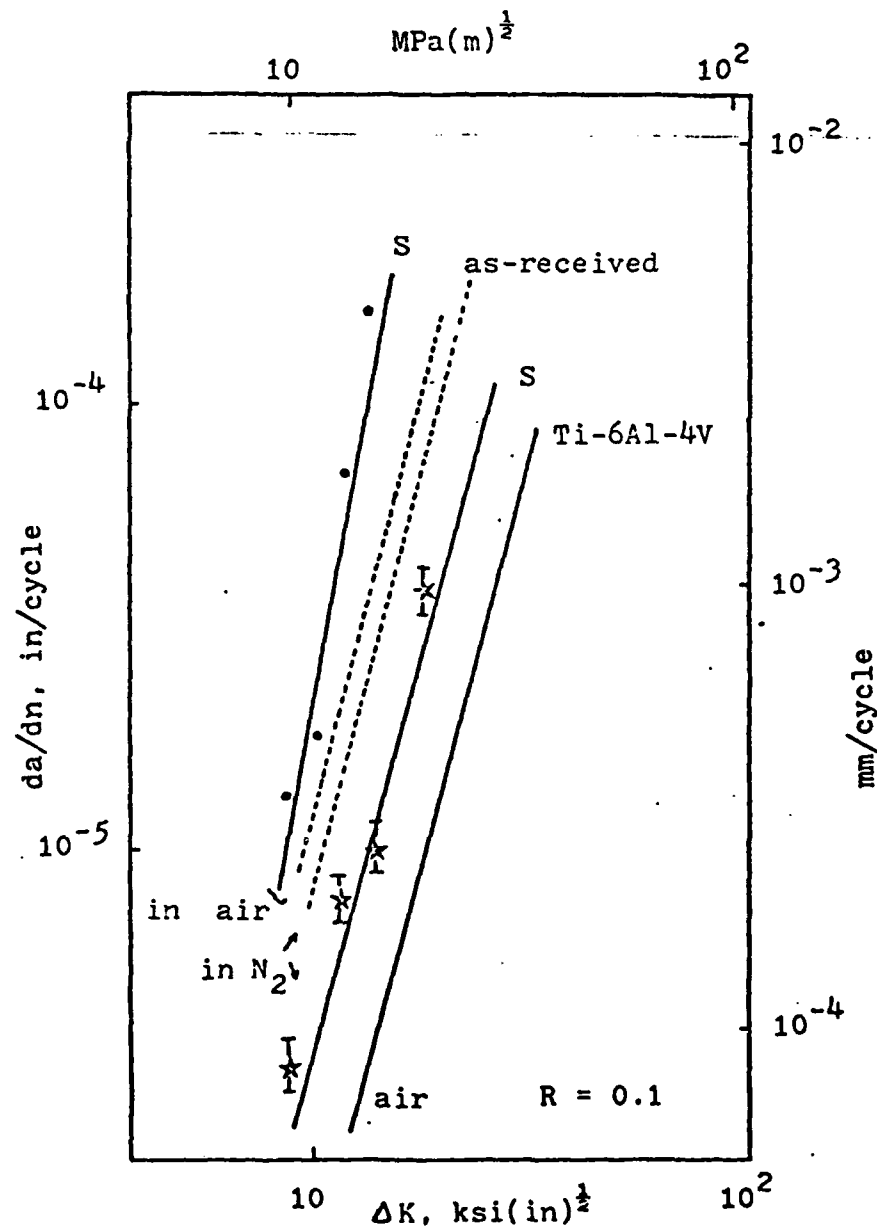


Fig. 3. Transverse FCG rates for B<sub>4</sub>C/B/Ti-6Al-4V thermal cycled in sulfur compared with the initial condition and Ti-6Al-4V plate.

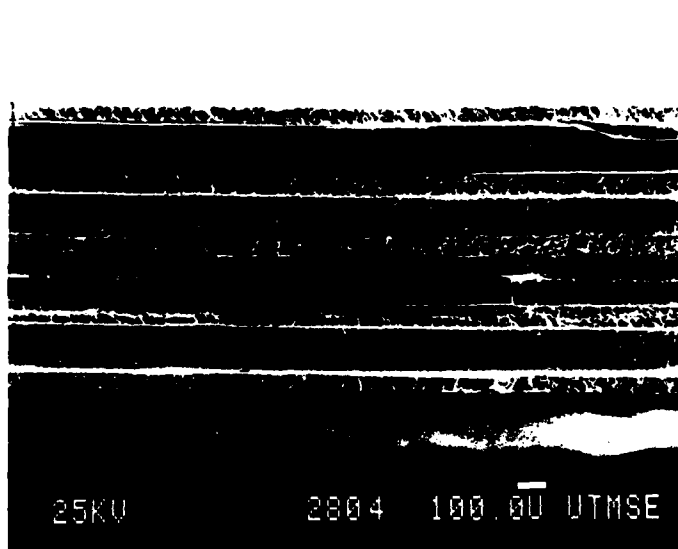


Fig. 4. SEM fractograph of FCG in air for as-received  
B<sub>4</sub>C/B/Ti-6Al-4V, transverse.



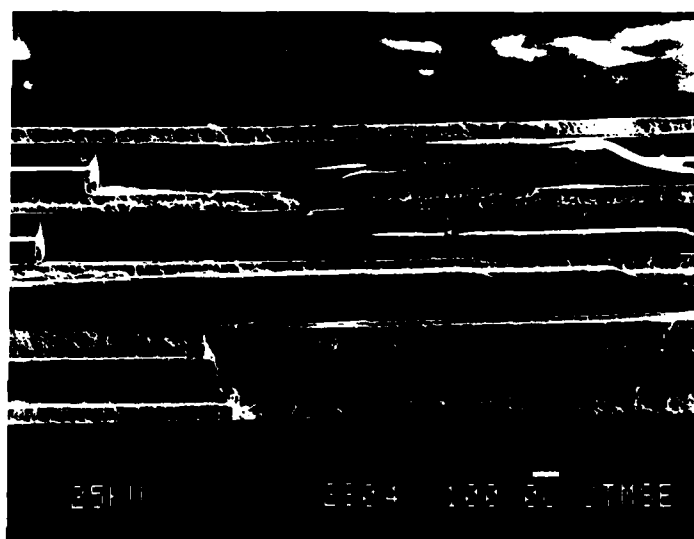


Fig. 5. SEM fractograph of FCG in dry  $N_2$  for as-received  $B_4C/B/Ti-6Al-4V$ , transverse.

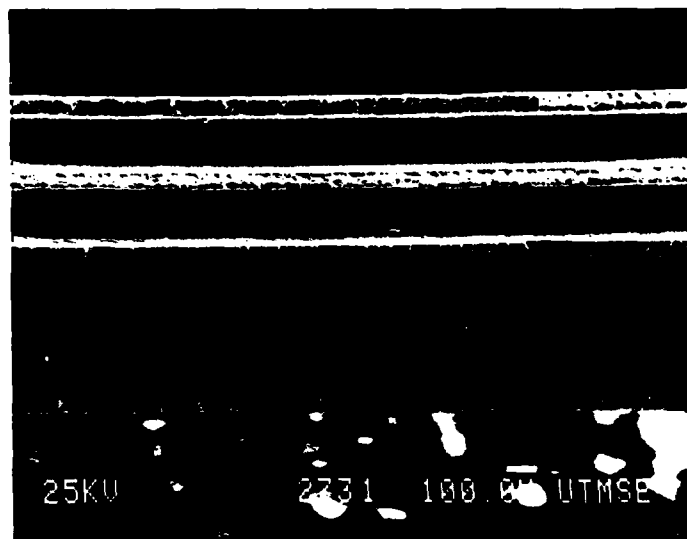


Fig. 6. SEM fractograph of FCG in air for B C/B/  
Ti-6Al-4V thermal cycled in sulfur, transverse. 4

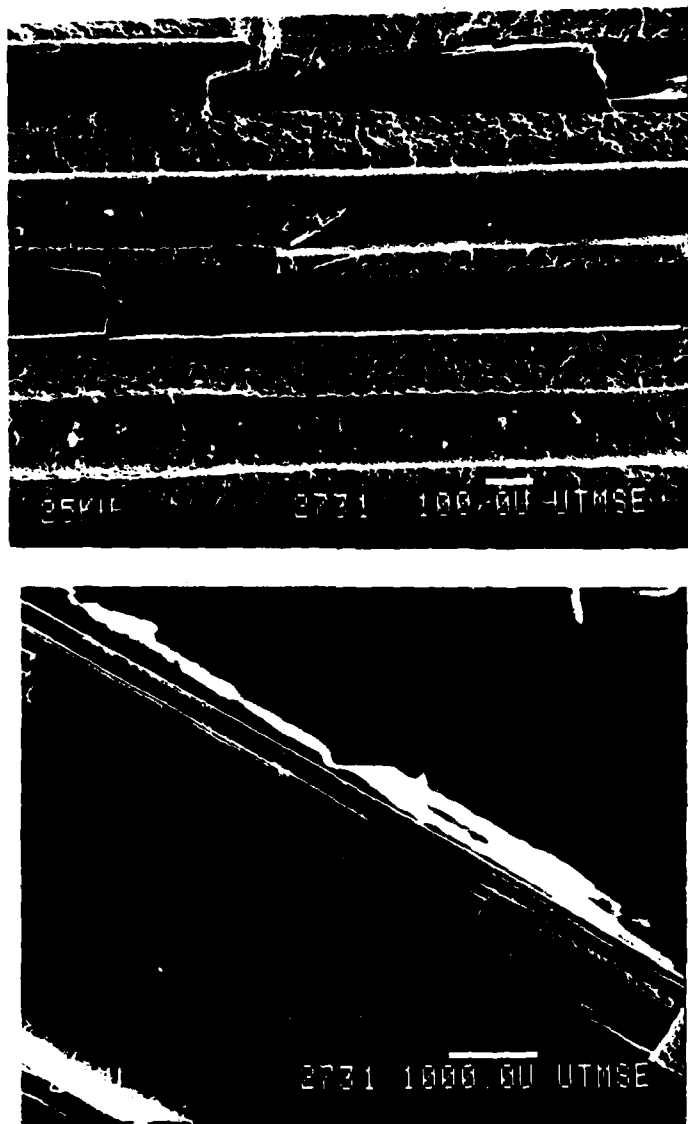


Fig. 7. SEM fractographs of FCG in dry  $N_2$  for  $B_4C/B/Ti-6Al-4V$  thermal cycled in sulfur, transverse.

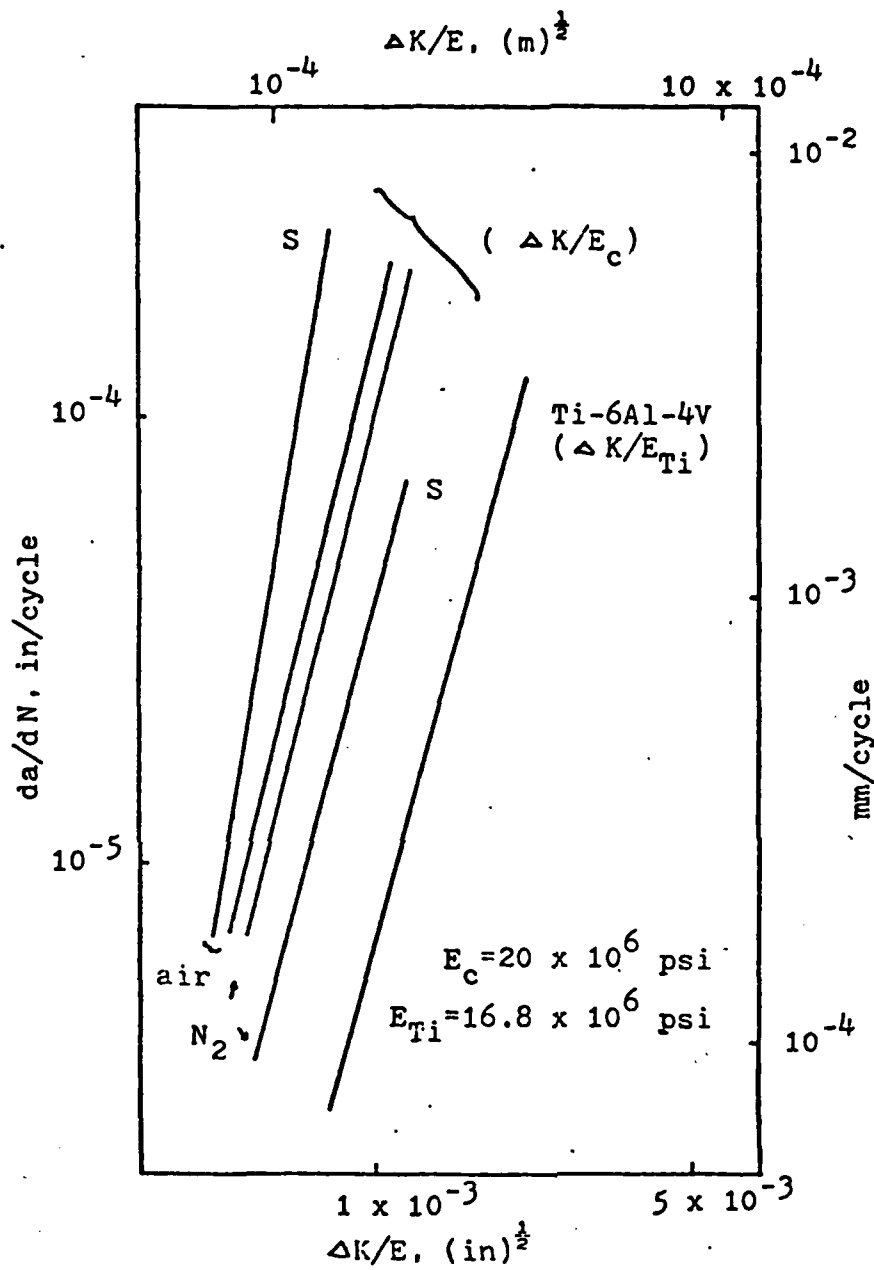


Fig. 8. FCG rates after the normalization of  $\Delta K$  by the elastic modulus, for  $B_4C/B/Ti-6Al-4V$  composite.

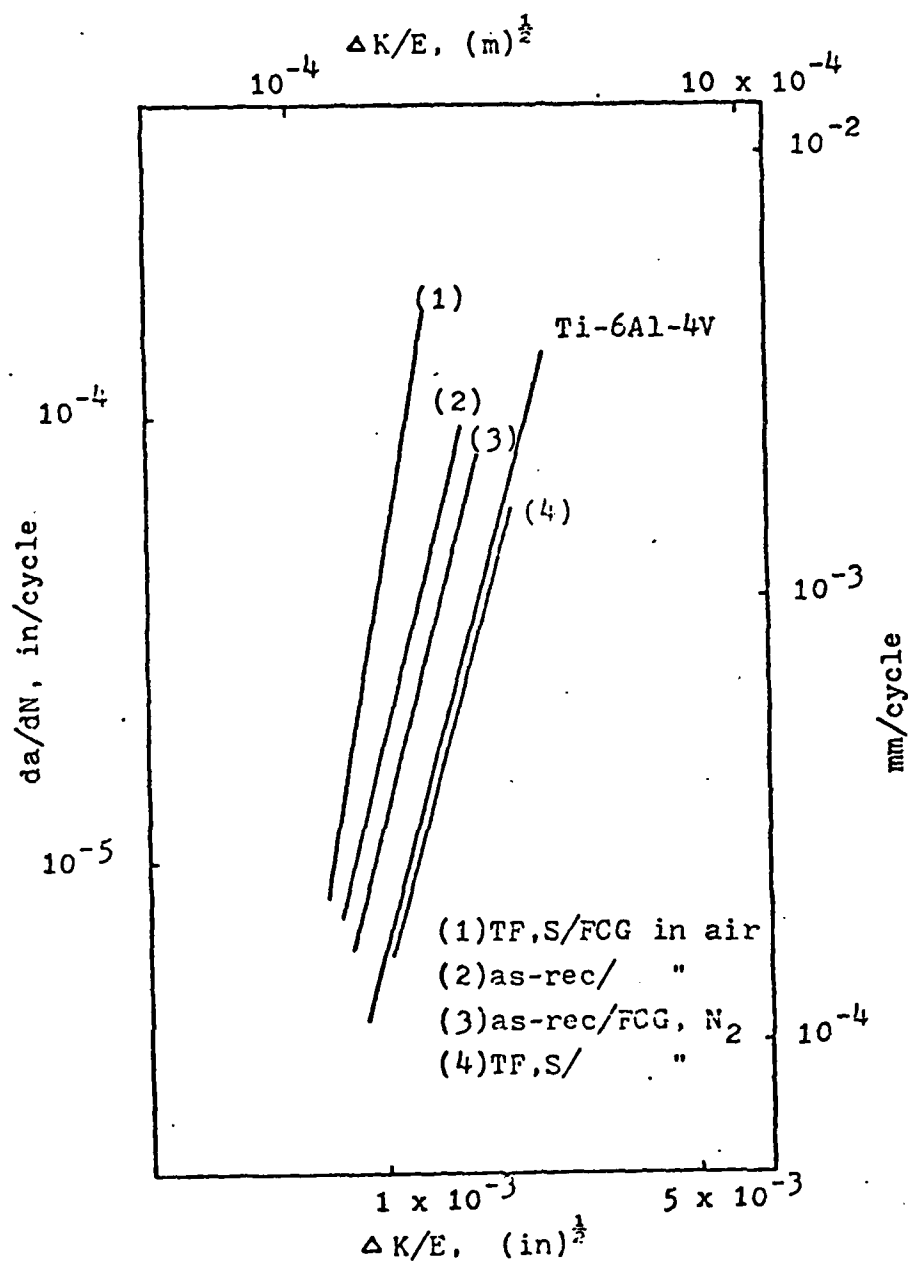
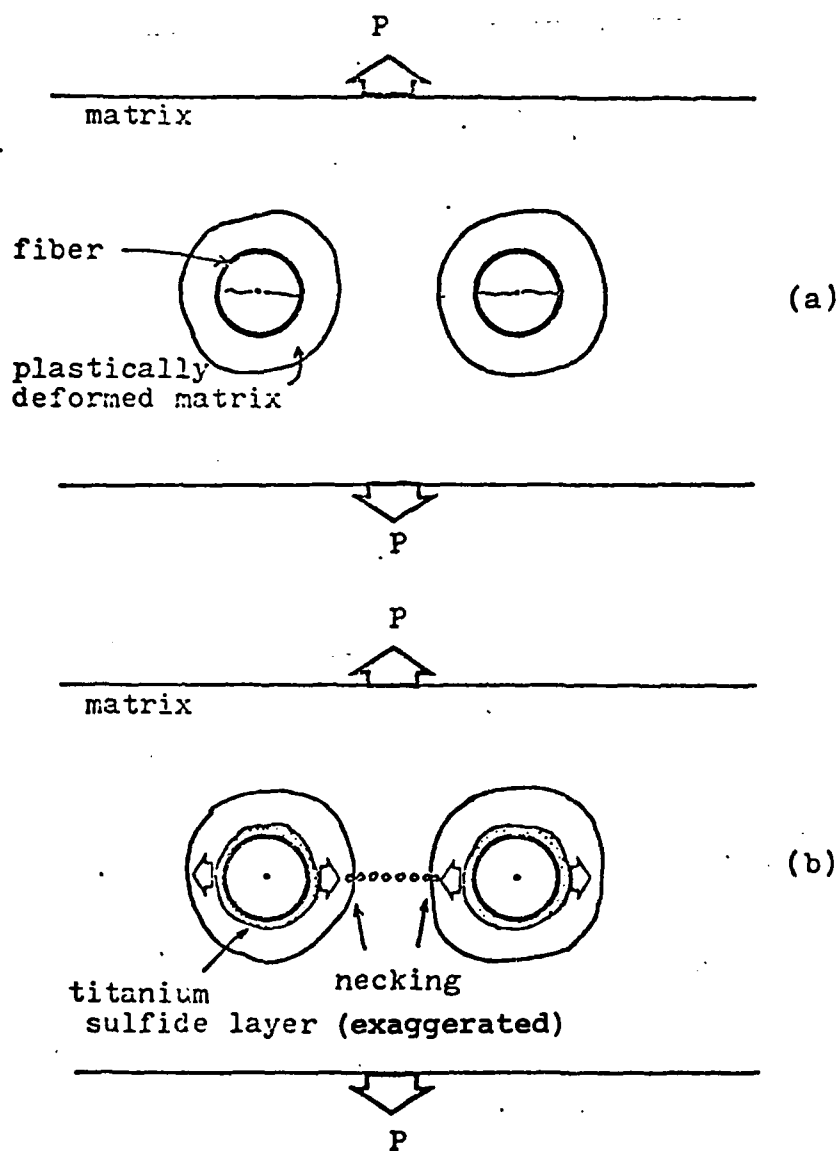


Fig. 9. FCG rates after the translation by a factor of  $1/0.6$ , for B<sub>4</sub>C/B/Ti-6Al-4V.



**Fig. 10** A model for FCG fracture modes in lab air; (a) in as-received; (b) thermal cycled conditions.

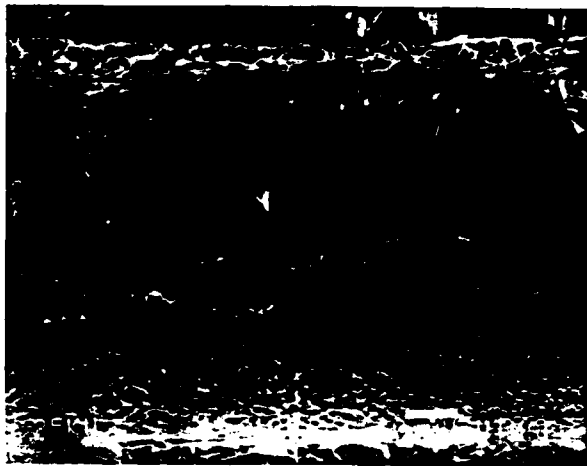


Fig. 11. SEM fractograph of SiC/Ti-6Al-4V composite thermal cycled in sulfur for one day up to 550°C, showing branch cracks along the matrix side interface.

APPENDIX G

Interface Diffusion Studies in Titanium  
Metal Matrix/Continuous SiC and  $B_4C$ /B Fiber Composites

Y.H. Park\* D. Narayen and H.L. Marcus  
Dept of Mechanical Engineering/Materials Science  
Engineering  
The University of Texas at Austin, Texas 78712

\* now with Materials Research Corporation,  
Orangeburg, New York.



### Abstracts

This paper reports results of the interface modifications due to thermal cycling treatments between room temperature and 550°C and isothermal treatments at 550°C in gaseous sulfur and air environments. The interaction between the sulfur environment and the titanium metal matrix (Ti-6Al-4V)/SiC and B<sub>4</sub>C/B fiber interface was evaluated in terms of interface diffusion. The diffusion down the interface was enhanced under the thermal cycling conditions. The 550°C sulfur interface diffusion coefficient was found to be  $5 \times 10^{-9}$  cm<sup>2</sup>/sec for the SiC composites and  $7 \times 10^{-9}$  cm<sup>2</sup>/sec for the interface diffusion in B<sub>4</sub>C/B composites.

In addition to the diffusion down the interface, diffusion into the matrix was studied with combined scanning Auger microscopy and inert ion sputtering. The rapid diffusion down the boundary was separated from the slow diffusion into the bulk resulting in two one-dimensional analyses. The sulfur diffusion down the interface was much larger than that into the bulk, a  $10^5$  difference in diffusion distance.

## Introduction

Unidirectionally reinforced metal matrix composites (MMCs) have generated a considerable amount of interest in the materials field because of their potential applications in dynamic structures. Ultra-high strength metals cannot supply the improved high strength, rigidity, light weight and heat resistant properties that are increasingly being required. A metal matrix composite system (MMC) carries certain potential advantages over other non-metal containing composite systems. High strength, modulus, toughness, reproducibility of properties, surface durability and low notch sensitivity when compared to non-metal matrix composites are just a few of these potential advantages. The MMC systems are characterised by heterogeneity, anisotropy, strengthening by load transfer and interfaces. In order for the full potential of these systems to be used, a better understanding of the above-mentioned effects must be acquired.

Studies<sup>1-4</sup> have been done to obtain tensile, toughness and fatigue properties of various MMC systems. Limited studies<sup>5</sup> have been done on the interface between the metal matrix and the fiber in environments as a function of temperature. Composite materials present a variety of complex problems in thermomechanical behavior due to differences in properties of matrix and fibers. Recent work<sup>6-11</sup> has treated the case of thermal cycling of composites consisting of elastic fibers and a metal matrix in order to analyze the distribution of stress and strain, obtain expansion properties and investigate possible damage mechanisms. Thermal cycling in various environments will obviously be important in many elevated temperature applications. It is, therefore, necessary to know more about the thermal fatigue properties of MMCs and to relate them to the nature of the interface.

Better understanding of this relationship can assist in improved composite design and advancement in processing of composites.

The purpose of this investigation is to study the interaction between environment and the metal matrix-fiber interface in titanium MMCs and the diffusion behavior of the environmental elements under thermal cycling and isothermal treatment conditions.

### Experimental Materials

The metal matrix composite (MMC) systems used in this study were 40 % by volume of SiC or B<sub>4</sub>C/B continuous fibers (diameter of 150  $\mu$ m) in a Ti-6Al-4V alloy matrix. The composite panel was four ply, approximately 0.84 mm thick. The samples were evaluated in the as-received conditions and after the thermal cycling for various time over the temperature ranges of room temperature to 480, 530 and 590°C, or 480, 510 and 540°C.

### Experimental Evaluation of the Interface Chemistry

In order to investigate the chemistry of the interface between the matrix and the fiber the Physical Electronics 590 scanning Auger microscopy (SAM) operating at a base vacuum of  $2.6 \times 10^{-8}$  Pa ( $2 \times 10^{-10}$  torr) was used.

The specimens were fractured in-situ in the vacuum chamber and several points in the fracture surface were selected, both on the matrix and on the fiber side of the fractured interface. The selected points were then argon ion sputtered to determine the sputtered depth profiles for the elements identified at the boundary. Auger profiles for the sputtered select points were recorded and analyzed. The sputtering was done by 3 KeV argon ion at 24 mA ion current with a raster size of 2 mm x 2 mm and at  $3.3 \times 10^{-5}$  Pa ( $2.5 \times 10^{-7}$  torr) pressure in the sample chamber. The sputter depths were calculated by comparison with standard sputtering rates for titanium oxide which sputtered at approximately 2 nm/min (  $8 \times 10^{-8}$  in/min) for the sputtering parameters used. Using the combined Auger and sputtering data, diffusion and kinetics studies were made for the specimens thermal cycled in the air and in the sulfur environments and for samples isothermally aged. The points were chosen from the exposed edge of the specimen into the interior of the specimen on the matrix and fiber sides of the interface. This allowed the interface diffusion kinetics to be determined. The Auger data was quantified using the method<sup>12</sup> described in the Appendix A.

## Interface Diffusion Analysis

### One-dimensional Diffusion Analysis

The sulfur peak-to-peak height on the matrix side of the interface vs. distance from the end of the specimen for SiC/Ti-6Al-4V composites is plotted in Fig. 1. As discussed in Appendix A peak-to-peak (p/p) height,  $S_s(z)$  at  $y=0$  should be converted to true concentration,  $C_s(z)$  at  $y=0$ . Since the sputtering was carried out at only one location into the bulk, that is, at  $z = z_1$ , the concentrations along the interface were obtained from the calculations using elementary sensitivity factors<sup>13</sup>. All profiles show ever decreasing amounts of sulfur toward the inside of the specimen. The profile of the specimen thermal cycled for one day shows a high concentration of sulfur near the end of the specimen. The plot of the logarithm of sulfur concentration vs. distance displayed a linear dependence of the data for the thermal cycled specimens as shown in Fig. 2. Therefore, the experimental results can be expressed as

$$\ln S_s = kz, \quad (1)$$

where  $S_s$  is the concentration of sulfur in the interface,  $z$  diffusion distance and  $k$  the proportionality constant. When the concentration of oxygen from samples thermal cycled in air is plotted as logarithm  $S_o$  against the distance from the end, the results show a similar trend. Fig. 3 shows the combined results from

sulfur and oxygen experiments. The slope is steeper for the sulfur environment, indicating enhanced sulfur reaction which is expected due to the higher vapor pressure and corresponding activity in the sealed pyrex tube, about 3.9 atm, at the maximum cycling temperature of 550°C. It is also noted that the diffusion rate of sulfur associated with thermal cycling is higher for the SiC fiber composite when compared with the B<sub>4</sub>C/B fiber composite results.

The characteristic diffusion coefficient of sulfur down the interface was estimated based on the diffusion problem for a semi-infinite solid<sup>14</sup>. In this case the solution will have the form

$$S_s(z,t) = S_{s, \text{ at } z=0} (1 - \text{erf}(z/2(Dt)^{1/2})). \quad (2)$$

The diffusion distance of sulfur is defined as the distance from the end of the specimen to the location where the sulfur concentration drops to half the initial concentration<sup>15</sup>. From Fig. 2, the diffusion distance is, then, 140 μm from the end of the free surface.

$$\text{Again, } \frac{C}{C_s} = [1 - \text{erf}(z/2(Dt)^{1/2})].$$

$$\text{Then } \text{erf}(z/2(Dt)^{1/2}) = 1,$$

$$\text{Therefore, } \frac{z}{2(Dt)^{1/2}} = 0.477, \text{ giving } z \approx (Dt)^{1/2}.$$

With  $z = 140 \mu\text{m}$  and  $t = 4.3 \times 10^4 \text{ sec}$ ,  $D$  is calculated to be  $5 \times 10^{-9} \text{ cm}^2/\text{sec}$  at a maximum temperature of 550°C during thermal cycling for SiC/Ti-6Al-4V composite. The oxygen diffusivity was

also calculated, based on the same argument, to be  $7 \times 10^{-9} \text{ cm}^2/\text{sec}$  for  $\text{B}_4\text{C/B/Ti-6Al-4V}$  composite having  $z = 170 \mu\text{m}$ . The bulk diffusion coefficient of oxygen in titanium is about  $10^{-14} \text{ cm}^2/\text{sec}$ <sup>16</sup>.

SEM fractography shows the presence of branch cracks on the matrix side of the interface. The branch cracks extend an equivalent distance to the AES sulfur detection distance (Fig. 4). This implies that the interface cracking normal to the propagating main crack is associated with the thin but finite sulfide layer at the interface as well as the sulfur enriched matrix.



### Two-dimensional Diffusion Analysis

In the last section, the diffusion phenomena was considered as a unidirectional flow of sulfur through the interface from the end of the specimen. The resultant diffusion expression was the logarithm of sulfur concentration at the interface proportional to the diffusion distance measured from the end of the specimen. On the other hand, the sulfur diffuses into the titanium matrix bulk normal to the interface. Therefore, the problem is a two-dimensional diffusion of sulfur.

The interface is considered to be a thin layer of high diffusivity area between the titanium matrix and the fiber. The problem is to determine the concentration of solute in a semi-infinite solid having a semi-infinite slab as the interface of highly permeable material imbedded in it. The analysis in the z-direction (along the interface) was made by getting Auger spectrum on several points selected along the interface. The y-direction was made by argon ion sputtering one of select points ( at  $150\text{ }\mu\text{m}$  from the end of the specimen) into the matrix.

The diffusion profiles of the solute from AES analysis indicate that the bulk diffusion is small compared to the diffusion on the interface. The results of the sputtering by argon ion show that the sulfur diffused into the bulk only up to 4 nm for a one day thermal cycling. The solute diffuses up to  $400\text{ }\mu\text{m}$  down the interface for the same period of thermal cycling, a  $10^5$  difference in the diffusion distance. This confirms that the interface is in high energy state which provides high mobility of the environmental elements. Under these conditions, the grain boundary diffusion equation proposed by Fisher<sup>17</sup> can be applied to the present interface diffusion of sulfur in the environment in the titanium MMCs.

Consider the interface to be a thin layer of high diffusivity area between the titanium matrix and the  $\text{B}_4\text{C/B}$  fiber. The interface

can be considered to be approximately a plane ignoring the curvature effects of the 150  $\mu\text{m}$  fiber diameter. The model system is shown in Fig. 5. The problem is to determine the concentration of sulfur in a semi-infinite solid having a semi-infinite slab as the interface of highly permeable material imbedded in it.

The boundary conditions are:

$$\begin{aligned} C &= C_s \quad \text{for } z=0 \text{ and } T \geq 0 \\ C &= 0 \quad \text{for } z>0 \text{ at } t = 0 \end{aligned} \quad (3)$$

Following Fisher's analysis<sup>17</sup>, the differential equation which is valid inside the interface slab can be obtained. Consider an element of the slab which is  $dz$  long by  $l$  thick by unit length deep. The fluxes into, or out of, the faces normal to the  $y$  and  $z$  axes are shown in Fig. 5. Any plane normal to the  $x$ -axis is a symmetry plane, so  $J_x$  would be equal to zero. Then,

$$\begin{aligned} \partial C / \partial t &= (1/dz l) (l(J_z - J_z - (\partial J_z / \partial z) dz) - 2dz J_y) \\ \partial C / \partial t &= -\partial J_z / \partial z - (2/l) J_y \end{aligned} \quad (4)$$

$J_y$  is the flux out of the interface into the bulk and can be replaced by  $-D_b(\partial C / \partial y)$  with the gradient evaluated in the bulk just outside the interface slab. An expression for  $J_z$  can be obtained if an interface diffusion coefficient  $D_i$  is defined by the equation

$$J_z = -D_i \frac{\partial C}{\partial z} \quad (5)$$

Then,

$$\frac{\partial C}{\partial t} = D_i \frac{\partial^2 C}{\partial z^2} + \frac{2D_b}{\delta} \left( \frac{\partial C}{\partial y} \right)_{y=\frac{\delta}{2}} \text{ or } y=0 \quad (6)$$

Outside the interface, diffusion would obey the equation

$$\frac{\partial C}{\partial t} = D_b \nabla^2 C = D \frac{\partial^2 C}{\partial y^2} \quad (7)$$

The approximate solution of equations 6 and 7 is obtained as follows based on several experimental observations. The interface concentrations, at some point, as measured after two different aging times were within 20 % difference during the thermal cycling treatment (Fig. 6). It was also observed that the diffusion of sulfur into the bulk was very slow.

It can then be assumed that the interface concentration,  $C_b(y)$ , is imposed on each slice at the slab not too far from the free surface and held constant for the duration of the heat treatment. It is also assumed that the flux of solute in the bulk is normal to the interface slab. Then the system can be replaced with a series of slices normal to the  $z$ -axis of thickness  $dz$ .

The concentration in each slice is then given by the equation,

$$C(y,z,t) = C_i(z) [1 - \text{erf}(y/2(Dt)^{1/2})] \quad (8)$$

On integration by connecting the points of equal concentration in this "sliced" model,

$$C_i(z) = C_0 \exp \left[ \frac{-z\sqrt{2}}{(\pi D_b t)^{1/2} (D_i/D_b)^{1/2}} \right]$$

Giving

$$C(y,z,t) = C_0 \exp \left[ \frac{-z\sqrt{2}}{(\pi D_b t)^{1/2} (D_i/D_b)^{1/2}} \right] [1 - \text{erf}(\frac{y}{2\sqrt{D_b t}})] \quad (9)$$

Here, the amount of solute in each of a series of slices  $dz$  thick and parallel to the edge of the specimen will be

$$\begin{aligned}\bar{C}(z,t)dz &= C_i(z)dz \int_{-\infty}^{\infty} \left[1 - \operatorname{erf}\left(\frac{y}{2\sqrt{D_b t}}\right)\right] dy \\ &= C_i(z)dz [\text{constant}]\end{aligned}\quad (10)$$

A plot of  $\ln \bar{C}$  vs  $z$  then should give a straight line of slope,

$$\frac{-\sqrt{2}}{(\pi D_b t)^{1/2} (D_i/D_b)^{1/2}}$$

This diffusion analysis conforms to the experimental results giving a straight line fitting of  $\ln \bar{C}$  vs  $z$  (Fig. 6). From this relationship, the bulk diffusion coefficient of sulfur was calculated to be  $1 \times 10^{-20}$  cm<sup>2</sup>/sec and that of oxygen was  $2 \times 10^{-20}$  cm<sup>2</sup>/sec. The bulk diffusion of sulfur measured from Fig. A2 gave the diffusivity of  $2 \times 10^{-19}$  cm<sup>2</sup>/sec. These values are significantly lower than in those in the literature where  $D_{\text{oxygen}} = 0.45 \exp(-48 \text{ Kcal/RT})$ , cm<sup>2</sup>/sec. In this study, the interface consists of various complex titanium compounds which will change the movement of oxygen.

The analysis indicated that the sulfur concentration decreases exponentially with the diffusion distance,  $\ln C_s = k'z$ . As discussed previously,  $k'$  is the proportionality constant. The rapid diffusion down the interface was separated from the slow diffusion into the bulk resulting in two one-dimensional analyses. The sulfur has negligible solubility in titanium of about 0.017 w/o<sup>18</sup>. Sulfur form eleven different sulfides in the phase diagram<sup>19</sup>,

which results in the sputtering profiles showing continuously decreasing sulfur content into the bulk. A plateau in the sulfur profile would be observed if thicker single concentration sulfides existed in the interface layer, an observation made for measurements close to the end of the specimen. The actual diffusion coefficient is for sulfur diffusing through a series of closely related  $Ti_xS_y$  structures.

Temperature Dependence of the Interface Diffusion of Oxygen and Sulfur in  $B_4C/B/Ti-6Al-4V$  Composites during Thermal Cycling.

Temperature Dependence of Diffusion of Oxygen

From the diffusion study of thermal cycled specimens in the air environment between  $550^{\circ}C$  and room temperature, the diffusion of oxygen is concluded to be dominantly along the interface.

In order to determine the activation energy for the diffusion process measurements were made as a function of cycling time,  $\frac{1}{2}$ , 1, 2 days and maximum cycling temperatures, 480, 530, and  $590^{\circ}C$ . Fig. 7. is a plot of the  $\ln(p/p)$  height of the 510 eV oxygen signal (KLL transition) as a function of heating time at various maximum cycling temperatures at the position of  $150 \mu m$  from the end of the specimen. The slope of the line can be taken as the rate ( $R_o$ ) of oxygen diffusion along the interface from the end of the specimen during the thermal cycling. The rate equation can be expressed by<sup>20</sup>

$$(\text{rate}) = (\text{constant}) \times \exp(-E_a/RT)$$

when there is only one thermally activated process.

The activation energy may be calculated from the data in Fig. 8, by recognizing that the slope of the plot of  $\log R_o$  vs.  $1/T$  for oxygen is,  $-E_a/2.303R$ , where  $E_a$  is the activation energy,  $R$  the gas constant.  $E_a$  for the diffusion of oxygen along the interface in the titanium MMC was about 8 Kcal/mole. It has been reported that  $E_a$  for the diffusion of oxygen in single crystal titanium is about 48 Kcal/mole. In the present case, the  $E_a$  is for the interface diffusion mechanism of oxygen during the thermal cycling treatment.

### Temperature Dependence of Diffusion of Sulfur.

The activation energy for the sulfur diffusion during the thermal cycling was obtained at the temperature range of 480 and 540°C. The AES measurements were the same as for those of the oxygen environment. Fig. 9 is a plot of the logarithm of p/p height of the 152 eV sulfur signal (LMM transition) as a function of heating time at the position of 150  $\mu\text{m}$  from the end of the specimen. The plot of  $\log R_s$  vs.  $1/T$  for sulfur is shown in Fig. 12. The activation energy for the diffusion of sulfur along the interface in the titanium MMC was about 15 Kcal/mole. It is reported<sup>21</sup> that  $E_a$  for the sulfurization reaction of titanium is about 27 Kcal/mole. That of sulfur segregation in powdered titanium is 15.5 Kcal/mole<sup>22</sup> in the temperature range of 25 to 700°C. The later case may have an interface controlling diffusion reaction similar to that observed in this study. A least square fitting of the data for the isothermal treatment resulted in the almost identical slope with that for the thermal cycling treatment as shown in Fig. 2.

Higher sulfur and oxygen concentration along the interface for specimens thermal cycled show that the interface has a thin but finite thickness and is a high diffusion path for the sulfur and oxygen. The enhancement of diffusion for the thermal cycling treatment implies that thermal cycling itself plays a role in the accelerated degradation of the MMCs. Due to differences in coefficients of expansion between the matrix and the fiber, temperature cycling will include cyclic elastic-plastic stresses at the interface. Isothermal treatment does not induce these cyclic stresses.

### Summary and Conclusion

The interaction between the environment and the titanium metal matrix/SiC and  $B_4C/B$  fiber interface was evaluated in terms of interface diffusion under the thermal cycling treatments.

Samples thermal cycled in air between RT and  $550^{\circ}C$  for one day had high concentration peaks of oxygen at the interface near the exposed surfaces and diffused some distance into the interface. The isothermal treatment in air does not significantly increase the oxygen level on the interface. The reduction of longitudinal fracture strength and the fracture mode change in the titanium MMCs are attributed to the higher amount of oxygen and sulphur environments. Thermal cycled SiC/Ti-6Al-4V specimens showed a greater amount of oxygen and sulphur in the matrix side of the fractured interface and virtually none on the fiber side, showing the fracture path to be between the sulfide or oxide and the fiber in the interface.  $B_4C/B/Ti-6Al-4V$  specimens had a strong  $TiB_2$  peak on the matrix side of the fractured interface. This indicates that the fracture occurred at the  $B_4C$  and  $TiB_2$  interface. The plot of logarithm of sulfur concentration vs distance measured from the end of the specimen allowed a straight line fit to the data for thermal cycled specimens as follows :  $\ln S_g = kZ$  .

Similar trend was also noted from the oxygen profile. Results from isothermal treatment also show a straight line relationship.

The two dimensional diffusion problem was evaluated based on the grain boundary diffusion equation . The rapid diffusion down the interface was separated from the slow diffusion into the bulk resulting in two one-dimensional analysis. The sulfur diffusion down the interface was far larger than into the bulk, a  $10^5$  difference in diffusion distance, confirming that the interface provides a high rate diffusion path for environmental elements. The diffusion coefficient of sulfur down the interface was calculated to be



$5 \times 10^{-9} \text{ cm}^2/\text{sec}$  at a maximum temperature of  $550^\circ\text{C}$  during thermal cycling for SiC/Ti-6Al-4V composites. The oxygen diffusion coefficient was calculated to be  $7 \times 10^{-9} \text{ cm}^2/\text{sec}$  for  $\text{B}_4\text{C/B/Ti-6Al-4V}$  composites thermal cycled in air for one day between RT and  $550^\circ\text{C}$ . The activation energy of oxygen diffusion was 8 kcal/mole and that of sulfur was 15 kcal/mole, which are far below those for the bulk diffusion and are consistent with the interface diffusion mechanism.

#### Acknowledgements

The authors would like to acknowledge discussions with Dr. Michael Schmerling. This research was supported by the Air Force Office of Scientific Research under grant AFOSR 80-0052. The composites were supplied by the Air Force Materials Laboratory.

## Appendix A

### Correction of concentratin profiles from AES peak-to-peak Height Measurement.

Conventionally, the relative peak-to-peak (p/p) height of the element at a depth  $y$  below the top surface after sputtering are converted to composition using a relative sensitivity factor from the AES Handbook.<sup>13</sup> When the elemental standards are used, the intensity ratios from the standards must be corrected by factors related to the atom density, electronic escape depth and electron back scatter factor. This improves the accuracy with which the Auger peak intensities can be related to the surface composition<sup>23</sup>. However, the surface composition may still not equal bulk composition. Several attempts have been published to quantify the AES data for the ditribution of elements on the surface. Even though the effect of escape depth was emphasized, it was not directly used for the quantitative surface analysis of the material with thin layer structure.

In the present problem, since sulfur and oxygen are present as thin layers on the interface, the concentration of sulfur and oxygen will be different from the conventional calculation approaches which assume bulk concentration. For example, the p/p height of oulfur,  $S(y)$ , measured at a depth of  $y$  after sputtering is proportional to  $\int_y^\infty C_s(\zeta) e^{-(\zeta-y)/\delta} d\zeta$  (A1) where  $C_s(\zeta)$  is the true concentration at a depth of  $\zeta$  from the sputtered surface and  $\delta$  is the escape depth, as shown in Fig.A-1. The data is taken at a specific value of  $z$ , the distance down the boundary from the free surface.

Now, the problem is to get  $C_s(y)$  from the following integral equation : From equation A-1 with a change in variable,

$$S(y) = N \int_0^\infty C_s(\zeta+y) e^{-\zeta/\delta} d\zeta \quad (A-2)$$

where  $N$  is the sensitivity of the element excluding the escape depth.

In a derivation by H.A.Stevens<sup>12</sup>, eq. A-2 can be written as follows in terms of  $C_s(y)$ .

Since

$$\begin{aligned}
 \frac{dS(y)}{dy} &= N \int_0^{\infty} d\xi \frac{d}{dy} C_s(\xi+y) e^{-\xi/\delta} \\
 &= N \int_0^{\infty} d\xi \frac{d}{d\xi} C_s(\xi+y) e^{-\xi/\delta} \\
 &= N \left[ C_s(\xi+y) e^{-\xi/\delta} \right]_{\xi=0}^{\xi=\infty} + \frac{1}{\delta} \int_0^{\infty} d\xi C_s(\xi+y) e^{-\xi/\delta} \\
 &= -N C_s(y) + \frac{1}{\delta} S(y)
 \end{aligned} \tag{A3}$$

Then,

$$C_s(y) = \frac{1}{N} \left[ \frac{S(y)}{\delta} - \frac{dS(y)}{dy} \right] \tag{A4}$$

This gives the true surface chemistry in terms of the measured value and the slope of the inert ion sputtering profile. The experimental sulfur profile results can be curve-fit in the form shown in Fig. A-1.

$$S(y) = S_0 e^{-\alpha y} \tag{A-5}$$

$S_0$  is the p/p height at  $y = 0$ . Since

$$\frac{dS(y)}{dy} = -\alpha S_0 e^{-\alpha y} \tag{A-6}$$

Eq. 4 can be rewritten

$$C_s(y) = \frac{S_0}{N} \left[ \frac{1}{\delta} + \alpha \right] e^{-\alpha y} \tag{A7}$$

From Fig. A1, the value of  $y$  where the p/p height of sulfur equals  $S_0/e$  is found to be 13 Å. From this observation,

$$S(y) \Big|_{y=13} = S_0 e^{-\alpha \cdot 13} = \frac{S_0}{e}$$

giving  $\alpha = 0.077 \text{ Å}^{-1}$

With the  $\delta$  of the sulfur being 8 Å ,

$$\begin{aligned}
 C_s(y) &= \frac{S_0}{N} \left[ \frac{1}{8} + 0.077 \right] e^{-0.077y} \\
 &= 0.202 \frac{S_0}{N} e^{-0.077y}
 \end{aligned}
 \tag{A8}$$

$$S(y) = S_0 e^{-0.077y} \tag{A9}$$

Here  $S_0 / N$  cannot be obtained by observing the sulfur profile alone. Observation of the titanium sputtering profile,  $T(y)$ , can allow the determination of the true titanium concentration,  $C_{Ti}(y)$ . The sputtering profiles of boron and others including carbon, aluminum and vanadium are found to be approximately constant, giving  $C_B = 55\%$ ,  $C_{others} = 15\%$ ; since below the depth of at least 3  $\text{\AA}$ , the concentrations calculated based on AES Handbook will give approximately true concentrations of elements such as titanium, boron, carbon, aluminum and vanadium, and their sum should be 100%.

From the experimental observations, the p/p height of titanium is given by

$$T(y) = 0.3(1 - pe^{-\beta y}) \tag{A10}$$

since  $T(y) \rightarrow 0.3$  as  $y \rightarrow \infty$  (considering  $C_B = 0.55$  and  $C_{others} = 0.15$ ). Similarly,

$$T(y) = M \int_0^\infty C_{Ti}(z+y) e^{-z/\delta} dz \tag{A11}$$

where  $M$  is the sensitivity of the titanium and  $\delta_{Ti} = 12 \text{ \AA}$ . At  $y = 20 \text{ \AA}$ ,  $T(y)_{\text{at } y=20} = 0.3(1 - pe^{-20\beta}) = \frac{1}{2} \times 0.3$  and  $y = 40 \text{ \AA}$ ,  $T(y)_{\text{at } y=40} = 0.3(1 - pe^{-40\beta}) = \frac{2}{3} \times 0.3$ . Then,  $\beta = 0.002$  and  $p = 0.75$ .

Therefore,

$$\begin{aligned}
 C_{Ti}(y) &= \frac{1}{M} \left[ \frac{1}{\delta} - pe^{-By} \left( \frac{1}{\delta} + \beta \right) \right] \\
 &= \frac{1}{M} [0.083 - (0.75)(0.103)e^{-0.02y}] \\
 &= \frac{1}{M} [0.083 - 0.078e^{-0.02y}]
 \end{aligned}$$

Again since, as  $y \rightarrow \infty$ ,  $C_{Ti} \rightarrow 0.3$ ,  $M = 0.277$ . Therefore,

$$C_{Ti}(y) = 0.30 - 0.282e^{-0.02y} \quad (A12)$$

$$T(y) = 0.30 - 0.225e^{-0.02y} \quad (A13)$$

From the mass conservation,  $C_{others} + C_B + C_{Ti} + C_S = 1$  at  $y=0$ . Then,

$$C_S = 0.282 = \frac{S_0}{N} (0.202)e^{-0.077 \cdot 0}. \quad \frac{S_0}{N} = 1.4.$$

Therefore,

$$S(y) = S_0 e^{-0.077y} \quad (A14)$$

$$C_S(y) = 0.282e^{-0.077y} \quad (A15)$$

The results are shown in Fig. A2.

As shown above,  $S(y)$  or  $T(y)$  should be corrected to  $C_S(y)$  or  $C_{Ti}(y)$  to obtain true concentrations of the elements. In the course of these derivations, several variables were not taken into account. These include, (1) preferential sputtering effects, (2) surface roughness, (3) interaction effects between elements, (4) knock-in effects, and (5) peak shape changes (not too significant for sulfur and titanium).

Even with the other variables not taken into account this attempt to quantify the thin layer chemistry offers a much more meaningful approach. In particular, where the absolute surface concentrations are required for a diffusion analysis, the approach

is even more useful. The corrected data was used for the interface diffusion analysis.

References

1. A.G. Metcalfe, in *Metallic Matrix Composites*, K.G. Kreider, ed., Academic Press, 1974, p. 269.
2. K.G. Kreider, *ibid.*, p. 1.
3. J. Awerbuch and H.T. Hahn, *Experimental Mechanics*, 1980, p. 334.
4. J.R. Hancock, in *Fracture and Fatigue, Composite Materials*, L.J. Broutman, ed., Academic Press, 1974, p. 371.
5. R.T. Bhatt and H.H. Grimes, *Met. Trans. A*, vol. 13A, 1982, p. 1433
6. G. Garmong, *Metall. Trans.*, vol. 5, 1974, p. 2183.
7. G. Garmong, *ibid.*, p. 2191.
8. G. Garmong, *ibid.*, p. 2199.
9. G.C. Olson and S.S. Tomkins, in *Failure Modes in Composites IV*, TMS-AIME, 1979, p.1.
10. K.K. Chawla, *J. Mats. Sci.*, vol. 11, 1976, p. 1567.
11. J. Billingham and S.P. Cooper, *Metal Science*, vol. 15, 1981, p. 311.
12. H.A. Stevens, private communications.
13. L. Davis, et al., in *Handbook of Auger Electron Spectroscopy*, Physical Electronics, Inc., 1976.

14. P.G. Shewmon, in *Diffusion in Solids*, McGraw-Hill, 1963, p. 14.
15. L.S. Darken and R.W. Gurry, in *Physical Chemistry of Metals*, McGraw-Hill, 1953, p. 444.
16. D. David, G. Beranger and E.A. Garcia, *J. Electrochem. Soc.*, vol. 130, 1983, p. 1423.
17. J.C. Fisher, *J. Appl. Physics*, vol. 22, 1951, p. 74.
18. L.B. Berger, *et al.*, *TMS-ASM*, vol. 49, 1957, p. 300.
19. S.A. Shunk in *Constitution of Binary Alloys*, 2nd supplement, McGraw-Hill Book Co., 1969.
20. L.S. Darken and R.W. Gurry, *op. cit.*, p. 466.
21. J.E. Dutrizac, *J. Less Common Metals*, vol. 51, 1977, p. 283.
22. C.P. Lofton and W.E. Swartz, Jr., *Appl. Spectroscopy*, vol. 32, 1978, p. 177.
23. P.H. Holloway and S.K. Hofmeister, *Surf. Interf. Analysis*, vol. 4, 1982, p. 181.
24. J.F. Smith and H.N. Southworth, *Surf. Sci.*, vol. 122, 1982, p. L619.
25. J. Cazaux, *J. Microsc. Spec. Electro.*, vol. 7, 1982, p. 487.
26. S. Bouquet *et al.*, *Spec. Electro.*, vol. 7, 1982, p. 447.
27. G. Luckman, L.A. Adler and W.R. Graham, *Surf. Sci.*, vol. 121, 1982, p. 61.
28. L.V. Phillips, *et al.*, *ASTM-STP 643*, 1978, p. 47.
29. L. Marchut and C.J. McMahon, in *Electron and Positron Spectroscopies in Materials Science and Engineering*, 1979, Academic Press, p. 183.



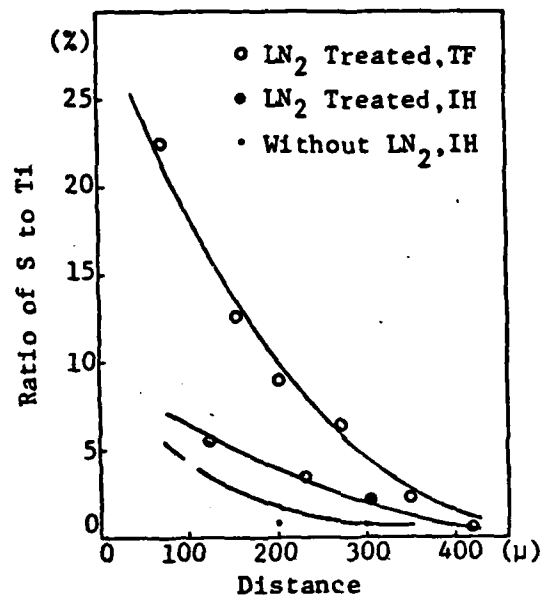


Figure 1. AES analysis of sulfur along the matrix side of interface for SiC/Ti-6Al-4V composites, thermal cycled (TF) and isothermally treated (IH).

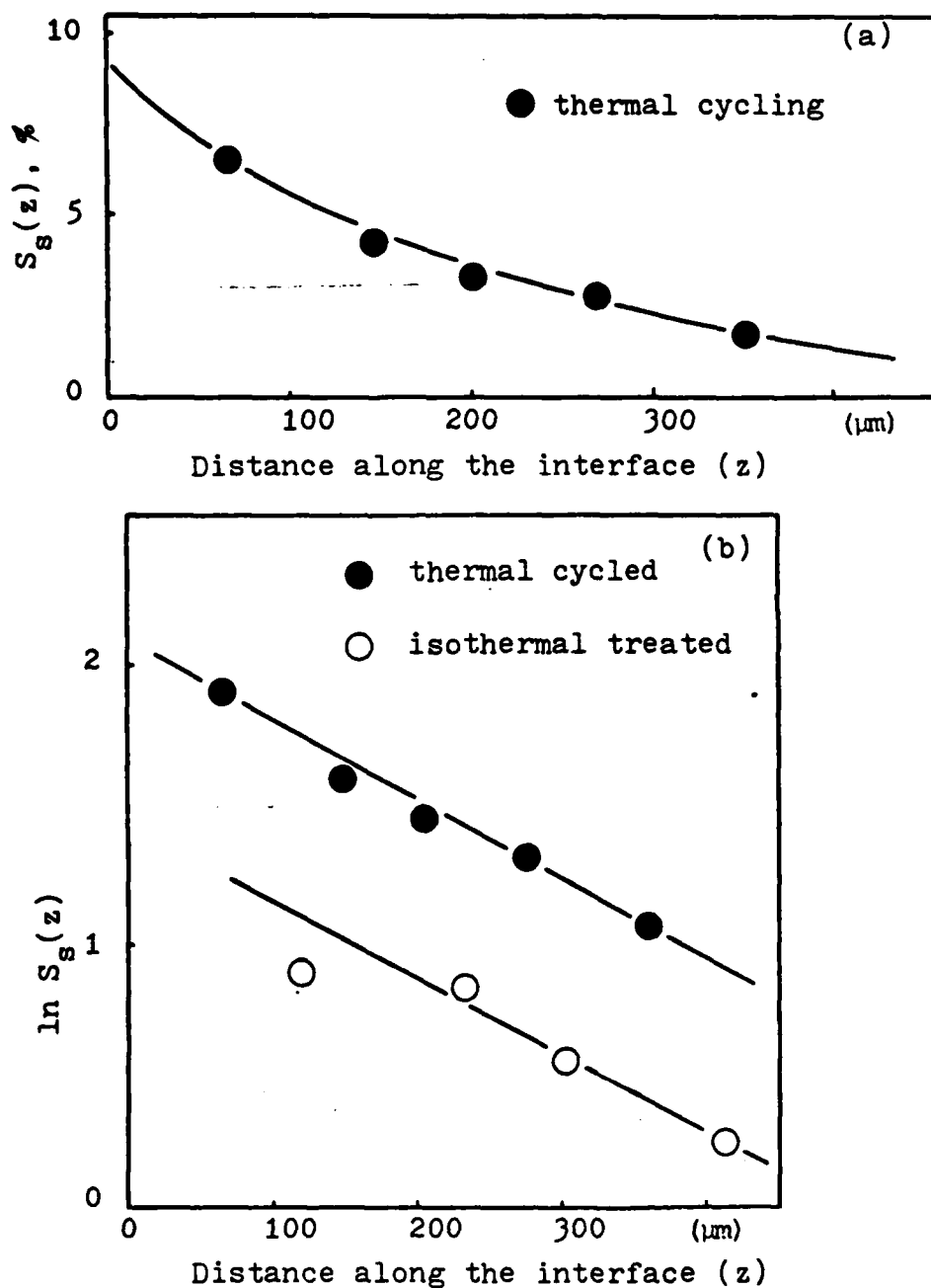


Figure 2. Sulfur concentration changes along the matrix side interface; (a)  $S_g(z)$ , (b) logarithm fitting of  $S_g(z)$  for SiC/Ti-6Al-4V.

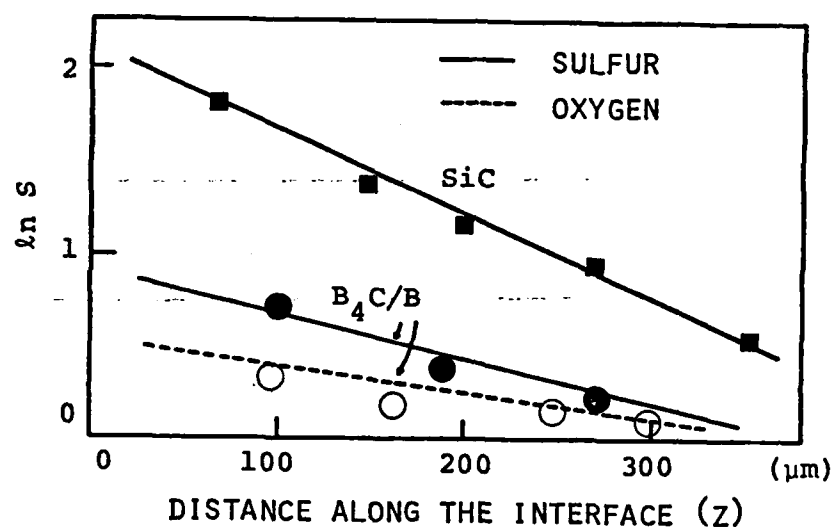
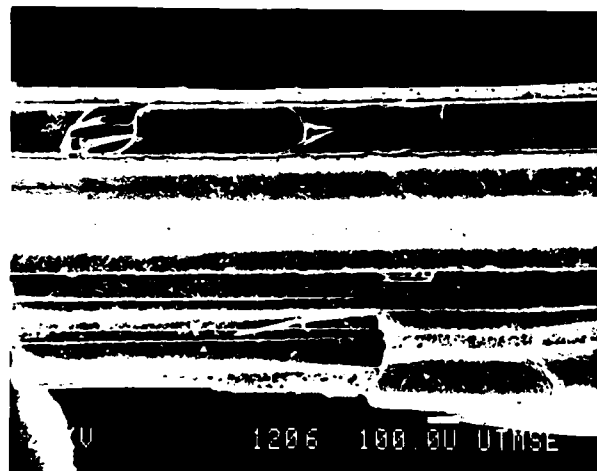
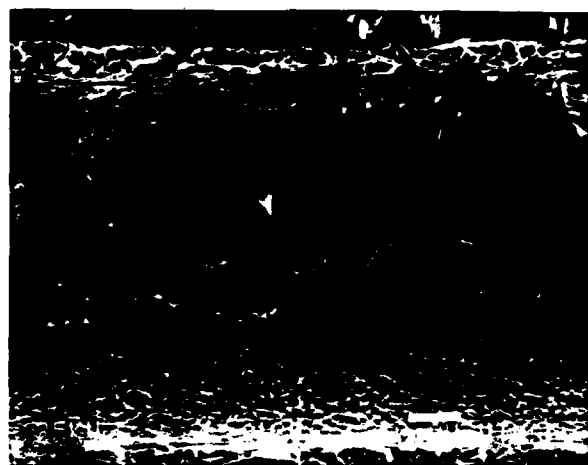


Figure 3. Logarithmic fitting of environmental element concentration along the matrix side interface, sulfur and oxygen, thermally cycled for one day between  $25^{\circ}\text{C}$  and  $550^{\circ}\text{C}$ .



(a)



(b)

Fig. 4. SEM fractographs of SiC/Ti-6Al-4V composite thermal cycled in sulfur between 25 °C and 550 °C for one day; (a) transverse, unnotched, (b) interface showing branch cracks in higher magnification.

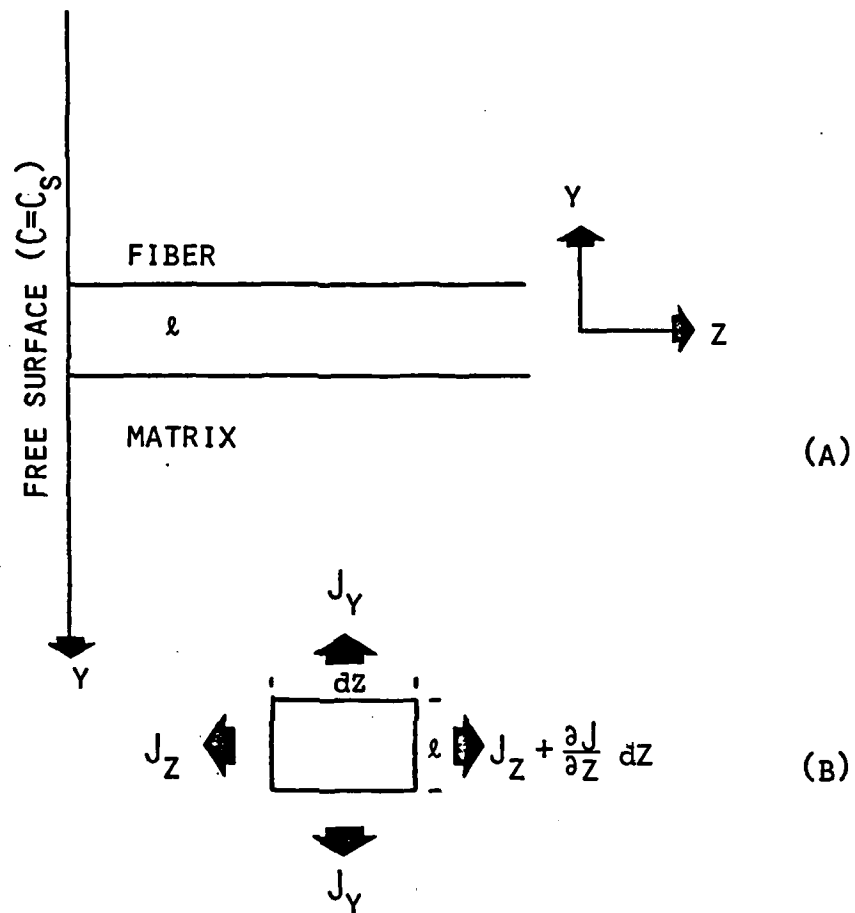


Figure 5. Schematic illustration of the geometry of the two-dimensional diffusion analysis.  
(  $l$  the interface thickness)

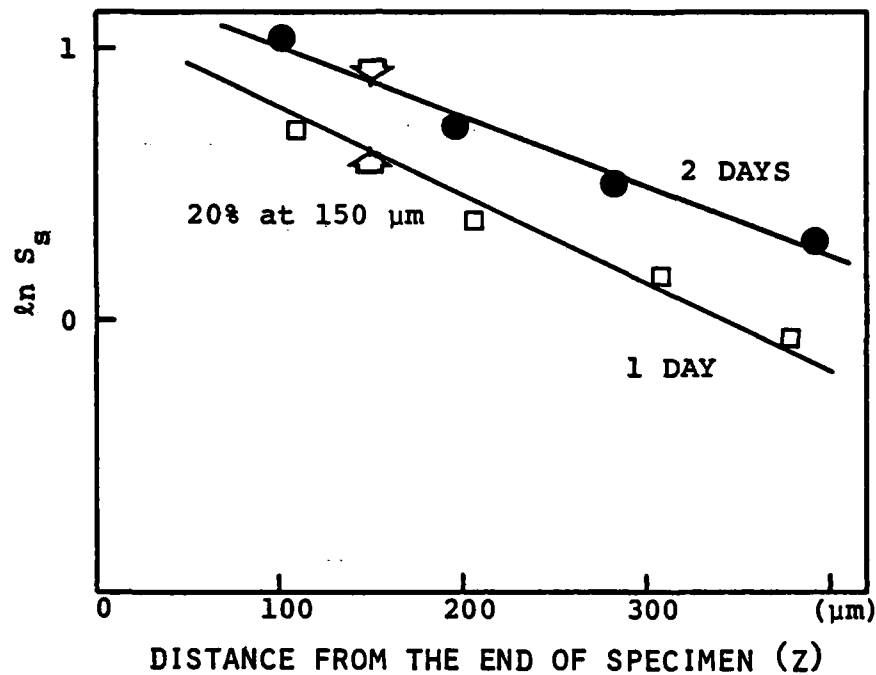


Figure 6. Logarithmic fitting of sulfur concentration along the interface showing the concentration difference for two different aging times is about 20 % for  $\text{B}_4\text{C}/\text{B}/\text{Ti-6Al-4V}$  composite thermal cycled in sulfur to  $540^\circ\text{C}$ .

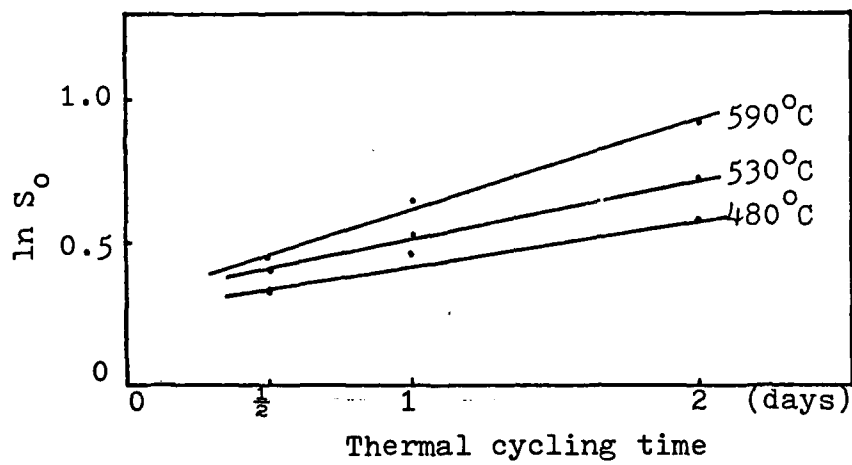


Figure 7. Rate of oxygen diffusion at various temperatures for  $B_4C/B/Ti-6Al-4V$  composite, matrix side interface.

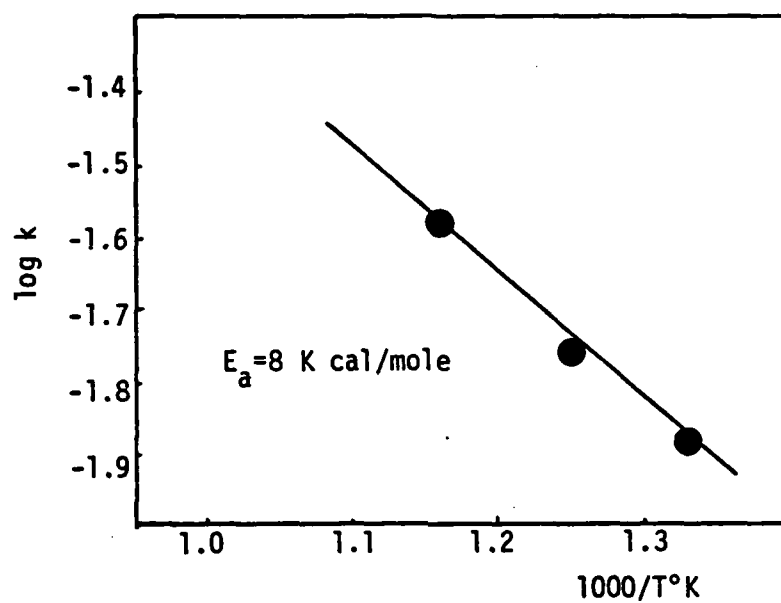


Figure 8 . Activation energy profile of oxygen for  $\text{B}_4\text{C/B/Ti-6Al-4V}$  composite thermal cycled in air.



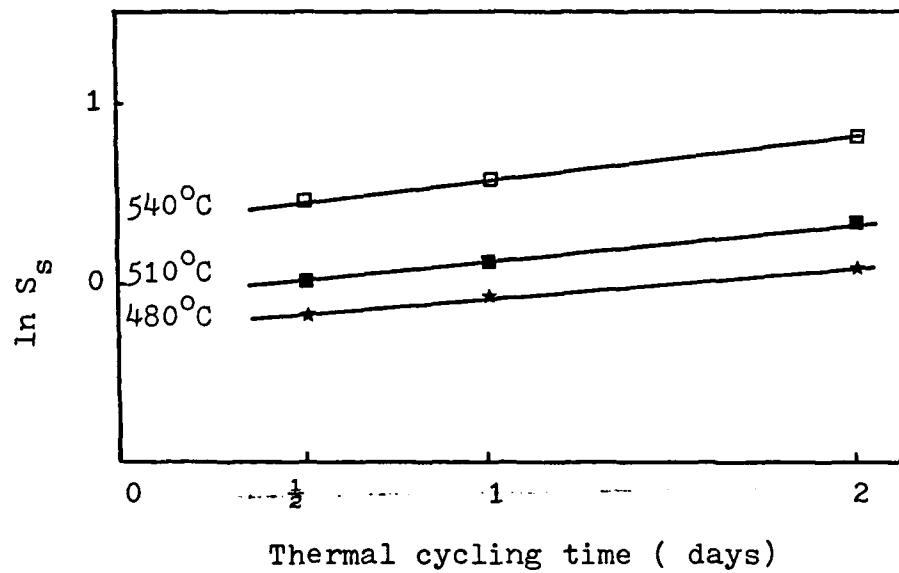


Figure 9. Rate of sulfur diffusion at various temperatures for  $B_4C/B/Ti-6Al-4V$  composite, matrix side interface.

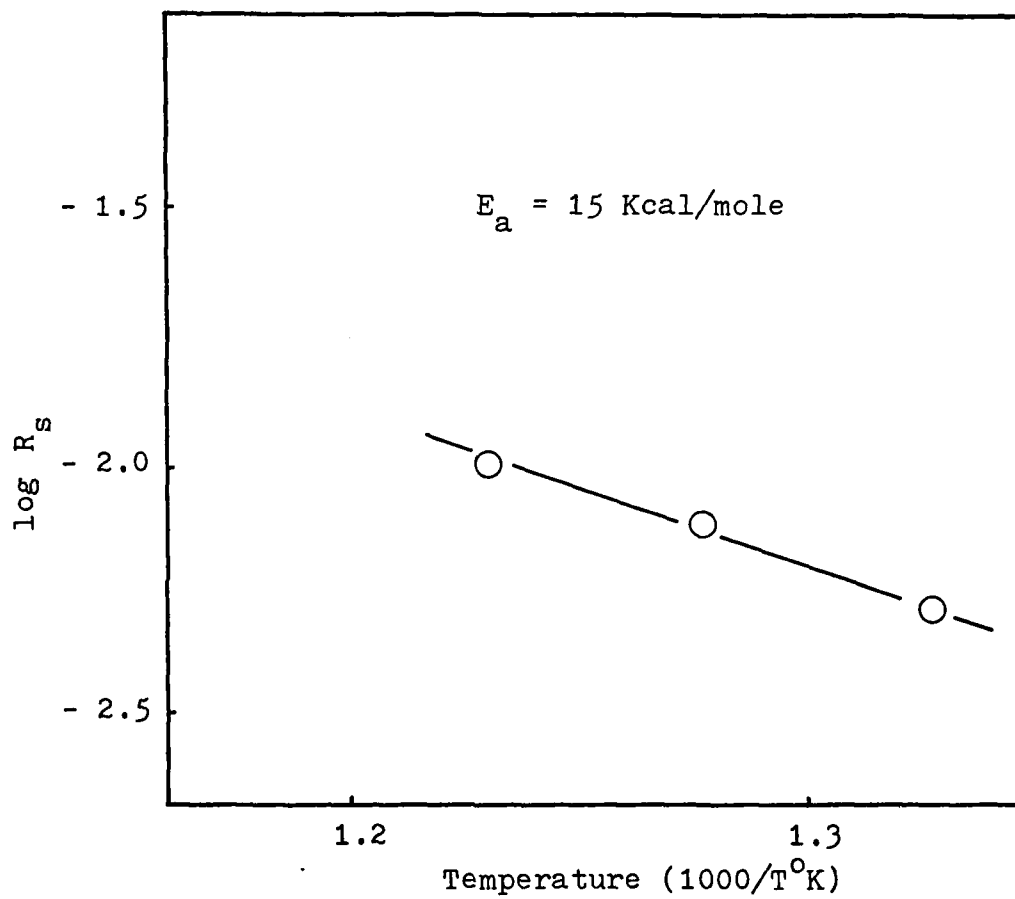


Figure 10. Activation energy profile of sulfur for  $\text{B}_4\text{C/B/Ti-6Al-4V}$  composite thermal cycled in sulfur for one day up to  $550^{\circ}\text{C}$ .

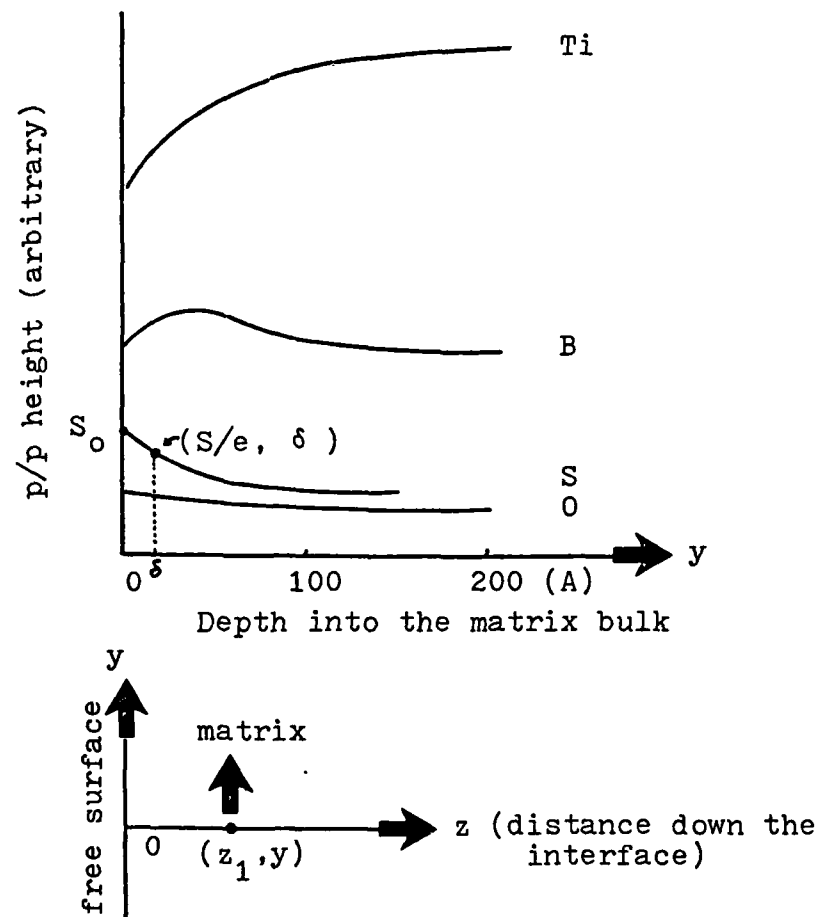


Figure A-1. Sputtering depth profile  
and the geometry of the analysis.  
(  $\delta$  the escape depth)

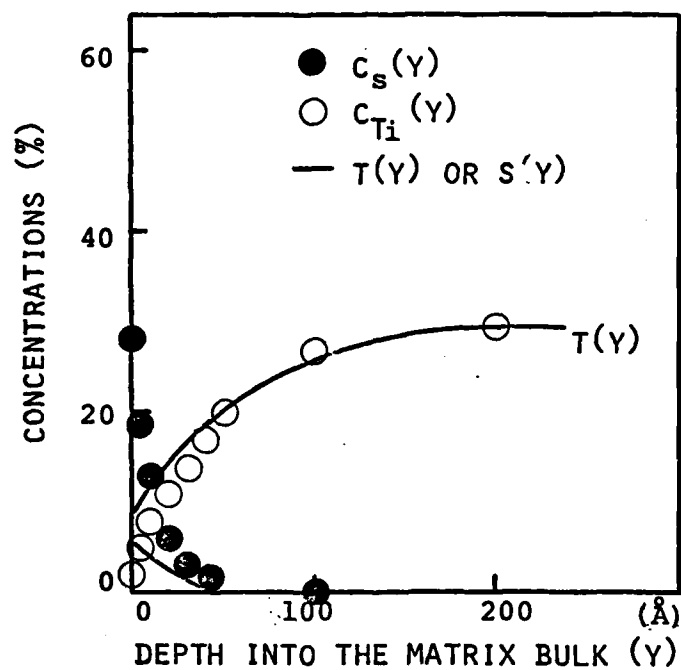


Figure A-2. Diagram of true concentrations of sulfur,  $C_S(y)$  and titanium,  $C_{Ti}(y)$ .

# The Influence of Alloying Elements on Impurity Induced Grain Boundary Embrittlement

D. Y. LEE, E. V. BARRERA, J. P. STARK, and H. L. MARCUS

A nonequilibrium thermodynamic model which describes the effect of solute grain boundary segregation on grain boundary cohesion was extended to Fe ternary systems. The extended model directly and simply predicts the effect of alloying elements on impurity-induced grain boundary embrittlement. According to the extended model, Mo, W, and Zr strongly reduce, Ni, Ti, and V slightly reduce, and Cr and Mn enhance impurity-induced grain boundary embrittlement in an Fe ternary system. For the evaluation of the extended model, Fe-P, Fe-P-Mn, Fe-P-Mo, and Fe-P-W alloys were studied by Auger electron spectroscopy, scanning electron microscopy, 4-point slow bend tests, and tension tests. The experimental results show that for a given amount of P grain boundary segregation the grain boundary strength increases with increasing Mo or W grain boundary segregation and decreases with increasing Mn grain boundary segregation. These experimental results showing the remedial effect of Mo or W and the embrittling effect of Mn on P-induced grain boundary embrittlement are consistent with the predicted results from the extended model. The nonequilibrium model is also used to evaluate impurity-induced interfacial embrittlement in continuous fiber metal matrix composite materials.

## I. INTRODUCTION

RECENTLY, Stark and Marcus<sup>1</sup> have developed a thermodynamic model which describes the effect of impurity (*I*) grain boundary segregation on the grain boundary cohesive energy. The development of the model was based upon a detailed nonequilibrium thermodynamic analysis of the grain boundary segregation process. This nonequilibrium model directly and simply provides a numerical estimate of the grain boundary cohesive energy change associated with impurity grain boundary segregation. However, it has been recognized that understanding the role of alloying elements (*A*) of the transition series is of great importance to predict and control grain boundary embrittlement in Fe alloys since the complex grain boundary embrittlement behavior is often encountered with the presence of alloying elements in Fe alloys. The effect of alloying elements on grain boundary embrittlement can be classified into the direct effect and the indirect effect. The indirect effect arises from the grain boundary cohesive energy change induced by the change in impurity grain boundary segregation due to the existence of the *I*-*A* interaction in Fe alloys. The *I*-*A* interaction and its effect on impurity grain boundary segregation has been rationalized by the Guttman model.<sup>2</sup> However, the direct effect of alloying elements which arises from the grain boundary cohesive energy change induced by their own grain boundary segregation has as yet to be considered.

The main purpose of this study is to investigate the combined direct and indirect effect of alloying elements on impurity-induced grain boundary embrittlement. Therefore, the nonequilibrium model will be extended to Fe-*I*-*A* ternary systems. This will be followed by the experimental study on high purity Fe-P, Fe-P-Mn, Fe-P-Mo, and Fe-P-W alloys for the evaluation of the extended model. In order to determine grain boundary strength, the method recently developed by Kameda *et al.*<sup>3,4</sup> will be adopted.

D. Y. LEE is Senior Research Engineer with General Dynamics Corporation, P.O. Box 748, Fort Worth, TX 76101. E. V. BARRERA, Graduate Research Assistant, J. P. STARK, Professor, and H. L. MARCUS, H. L. Kent, Jr. Professor, are all with the Department of Mechanical Engineering, The University of Texas, Austin, TX 78712.

Manuscript submitted September 13, 1983.

## II. THE EXTENDED NONEQUILIBRIUM MODEL

It is assumed in the development of the nonequilibrium model that the grain boundary (*GB*) region consists of the boundary (*B*) and boundary matrix interface (*BM*) regions as shown in Figure 1. Also, the thicknesses of these *B* and *BM* regions are assumed to be atomic in nature. The development of the extended model is presented in detail in Appendix B. The final result of the extended model can be expressed as:

$$\begin{aligned}\delta H^{GB} &= \delta H^B + \delta H^{BM} \\ &= \delta H_*^B + \delta H_*^{BM} - (\bar{H}_I^M + H_I^M - H_{Fe}^M) \delta N_I^M \\ &\quad - (\bar{H}_A^M + H_A^M - H_{Fe}^M) \delta N_A^M\end{aligned}\quad [1]$$

Where  $\delta H^{GB}$ ,  $\delta H^B$ , and  $\delta H^{BM}$  are enthalpy changes in *GB*, *B*, and *BM* during grain boundary segregation, respectively,  $\bar{H}_I^M$  and  $\bar{H}_A^M$  are the partial molar mixing enthalpies of an impurity *I* and an alloying element *A* in the matrix (*M*), respectively,  $H_I^M$ ,  $H_A^M$ , and  $H_{Fe}^M$  are the molar enthalpies of pure *I*, *A*, and Fe, respectively, and  $\delta N_I^M$  and  $\delta N_A^M$  are the changes in the number of moles of *I* and *A* in *M*, respectively. The terms  $\delta H_*^B$  and  $\delta H_*^{BM}$  in Eq. [1] are the enthalpy changes in *B* and *BM*, respectively, when *B* and *BM* transform from their initial high grain boundary energy state to their final low grain boundary energy state. This transformation is equivalent to the system undergoing grain boundary segregation as an attempt to obliterate the high grain boundary energy. A better understanding of these terms may be obtained from the details of the nonequilibrium model development presented in Reference 1.

Matrix ( <i>M</i> )	
Boundary Matrix Interface ( <i>BM</i> )	$s^{BM}$
Boundary ( <i>B</i> )	$s^B$
Boundary Matrix Interface ( <i>BM</i> )	$s^{BM}$
Matrix ( <i>M</i> )	

Fig. 1—Model of grain boundary region [1].

Since the "pV" terms associated with enthalpy are generally negligible in condensed phases, the enthalpy change in the grain boundary during grain boundary segregation is virtually equal to the change in the grain boundary cohesive energy because it reflects the change in the depth of the energy-well holding the atoms together. Then, it can be noted from Eq. [1] that the grain boundary cohesive energy change associated with grain boundary segregation is given as a function of the partial molar mixing enthalpies of *I* and *A*, the molar enthalpies of *I*, *A*, and Fe, and the changes in the number of moles of *I* and *A* in *M*. The partial molar enthalpies and the molar enthalpies can be obtained from the published thermodynamical data, and the changes in the number of moles of *I* and *A* can be determined from grain boundary chemistry analysis. Thus, a numerical estimate of the grain boundary cohesive energy change associated with grain boundary segregation can be made by using Eq. [1] with a proper approximation of the terms  $\delta H_*^B$  and  $\delta H_*^{BM}$ .

Stark and Marcus<sup>1</sup> have shown that the sum of the two terms,  $\delta H_*^B + \delta H_*^{BM}$ , is energetically equivalent to the energy required for the removal of the grain boundary at the initial grain boundary composition (i.e.,  $\delta H_*^B + \delta H_*^{BM} \approx -22$  kJ/mole). The molar enthalpies are substituted by the negative values of the published molar sublimation enthalpies.<sup>5</sup> Finally, the partial molar mixing enthalpies ( $\overline{H}_I^M$  and  $\overline{H}_A^M$ ) are determined from the details of the Fe-*I* or Fe-*A* binary phase diagram<sup>6</sup> by using a method discussed by Swalin.<sup>7</sup> Here, impurities include the well-known embrittling elements in Fe alloys such as As, P, Pb, S, Sb, Se, Sn, and Te, and alloying elements include the commonly found metallic additions of transition series such as Cr, Mn, Mo, Ni, Ti, V, W, and Zr. Table I lists the molar enthalpies and partial molar mixing enthalpies of the above impurities and alloying elements. As shown in Table I, the contribution of the partial molar mixing enthalpies to the estimation of the grain boundary cohesive energy change is quite small for most impurities and alloying elements. Therefore, this term will be ignored for the element whose partial molar mixing enthalpy could not be determined.

Table II shows the estimated value of the grain boundary cohesive energy change when a monolayer of either an impurity or an alloying element is present at the grain boundary in an Fe-*I* or an Fe-*A* binary system. It can be seen from Table II that all the impurities which have been known as grain boundary embrittlers reduce the grain boundary cohesive energy. Even the order of the embrittling potencies ( $P^E$ ) of P, Sb, and Sn is perfectly consistent with that found in experiments; the  $P^E$  of P, Sb, and Sn have been experimentally found to have the order of

**Table II. Grain Boundary Cohesive Energy Change with a Monolayer Grain Boundary Segregation of *I* or *A* in Fe-*I* and Fe-*A* Binary Systems (kJ/Monolayer)**

Fe- <i>I</i> System		Fe- <i>A</i> System	
<i>I</i>	$\delta H^{GB}$	<i>A</i>	$\delta H^{GB}$
As	-144	Cr	-41
P	-91	Mn	-136
Pb	-242	Mo	+252
S	-95	Ni	+3
Sb	-170	Ti	+39
Se	-231	V	+77
Sn	-130	W	+408
Te	-246	Zr	+336

$P^E(\text{Sb}) > P^E(\text{Sn}) > P^E(\text{P})$ .<sup>9</sup> However, the predicted  $P^E$  for S appears to be somewhat less than expected.

In the case of alloying elements, most of them are beneficial to the grain boundary cohesive energy except Cr and Mn. In particular, Mn exhibits a fairly high embrittling potency (i.e., even higher than P, S, and Sn for a given amount of grain boundary segregation). Of course, the grain boundary segregation enrichment ratio of Mn is much less than those of impurities. However, it is of interest to note that Schulz and McMahon<sup>10</sup> have experimentally found that in the absence of impurities, Mn itself causes grain boundary embrittlement in an Fe-0.7 Mn-0.4C system.

For Fe-*I*-*A* ternary systems, Figure 2 shows the variation of the grain boundary cohesive energy change with the molar fractional monolayer of alloying elements at the grain boundary where 0.5 monolayer of *P* is already present. From Figure 2 the direct effect of alloying elements on *P*-induced grain boundary embrittlement can be observed. By their direct effect, Mo, W, and Zr strongly reduce, Ni, Ti, and V slightly reduce, and Cr and Mn enhance *P*-induced grain boundary embrittlement in Fe alloys. These predicted results are consistent with the published experimental results showing the remedial effect of Mo<sup>10,11,12</sup> and Ti<sup>13,14</sup> and the embrittling effect of Cr<sup>11,15-17</sup> and Mn<sup>18,19,20</sup> on impurity-induced grain boundary embrittlement.

It is also of great interest to note that Schulz and McMahon<sup>10</sup> have experimentally found that Mo reduces Mn-induced grain boundary embrittlement in an Fe-0.7 Mn-0.6 Mo-0.4C system. The remedial effect of alloying elements has been attributed only to the indirect effect arising from the strong attractive *I*-*A* interaction which reduces impurity grain boundary segregation by precipitating the impurity in the matrix. However, the above interesting Mn-Mo behavior can be explained by the direct effect of Mn and Mo on the grain boundary cohesive energy. When both Mn and Mo simultaneously segregate to the grain boundary, Mn embrittles the grain boundary by its embrittling direct effect, while Mo improves the grain boundary cohesive energy by its remedial effect, thereby relieving Mn-induced grain boundary embrittlement.

Here, the effects of alloying elements were considered only on *P*-induced grain boundary embrittlement in Fe-*I*-*A* alloys. By using Eq. [1] the similar diagrams to Figure 2 can be generated for other embrittling elements in Fe-*I*-*A* alloys as well as non-Fe base alloys. Also, the nonequilibrium model can be applied to the interfacial embrittlement problems associated with impurity interfacial segregation in continuous fiber metal matrix composite materials as presented in Appendix C.

**Table I. Molar Enthalpies and Partial Molar Mixing Enthalpies of Impurities and Alloying Elements (Unit: kJ/mole)**

<i>I</i>	$H_I^M$	$\overline{H}_I^M$	<i>A</i>	$H_A^M$	$\overline{H}_A^M$
As	289	5	Cr	397	*
P [1]	334	13	Mn	279	23
Pb	196	1	Mo [8]	659	31
S [1]	276	67	Ni	427	14
Sb	259	9	Ti	472	5
Se	207	*	V	515	*
Sn	301	7	W	837	9
Te	192	*	Zr	611	163

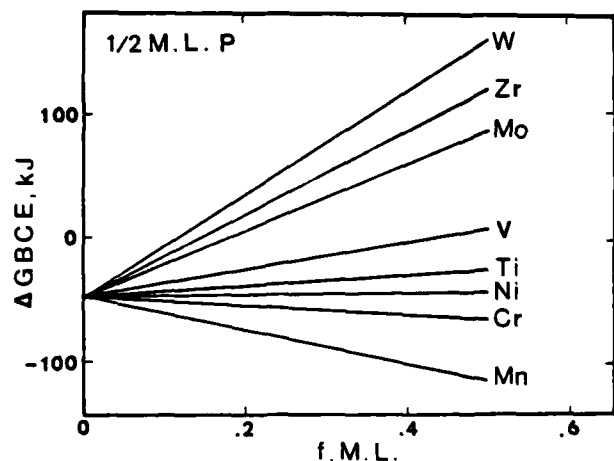


Fig. 2—The variation of grain boundary cohesive energy change with the fraction of a monolayer of grain boundary segregation of alloying elements with  $\frac{1}{2}$  monolayer P grain boundary segregation.

Recently, Seah<sup>21</sup> has proposed a simple pair bonding theory describing the grain boundary fracture energy change associated with solute grain boundary segregation in a binary system. Seah's result can be written as:

$$\Delta\gamma^{GB} = (Z^{GB}/Z^M)X_2^{GB}(H_1^* - H_2^*) \quad [2]$$

where  $\Delta\gamma^{GB}$  is the grain boundary fracture energy change associated with solute grain boundary segregation,  $Z^{GB}$  and  $Z^M$  are the coordination numbers of the atom in the grain boundary and the matrix, respectively,  $X_2^{GB}$  is the molar fractional monolayer of the solute 2 in the grain boundary, and  $H_1^*$  and  $H_2^*$  are the sublimation enthalpies per unit area of pure solvent 1 and pure solute 2, respectively. Here, the grain boundary fracture energy change, that is equivalent to the grain boundary cohesive energy change associated with solute grain boundary segregation, is directly related to the difference between the sublimation enthalpies of solvent and solute. The approach of Seah's pair bonding theory is quite different from that of the extended nonequilibrium model. However, it can be noted from Eqs. [1] and [2] that these two different theories show basically the same result that the grain boundary cohesive energy change associated with grain boundary segregation is directly related to the difference between the sublimation enthalpies of solvent and solute.

By applying equilibrium thermodynamics to the energetics of brittle fracture, several investigators<sup>22,23</sup> have attempted to calculate the work of brittle grain boundary fracture. According to the above approaches the work of brittle grain boundary fracture is often stated by the expression  $2\gamma^s - \gamma^{GB}$ , where  $\gamma^s$  and  $\gamma^{GB}$  are the surface energy and the grain boundary energy, respectively. The implication is that  $\gamma^s$  and  $\gamma^{GB}$  are equilibrium thermodynamic values. However, McMahon *et al.*<sup>24,25</sup> have criticized these attempts since fracture is essentially an irreversible process.

Recently, Losch<sup>26,27</sup> and Briant and Messmer<sup>28,29,30</sup> have studied the chemical bonding aspects of grain boundary embrittlement. Their results have suggested that the grain boundary embrittling impurities draw charge from the neighboring metal-metal bonds, which hold the grain boundary together, to form strong impurity-metal bonds

within the plane of the grain boundary. Thus, the metal-metal bonds across the grain boundary will be weakened, thereby leading to grain boundary embrittlement. The results<sup>30</sup> have also shown that P is more electronegative with respect to Cr and Mn than to Fe and more charge will be drawn from Cr and Mn onto P. Therefore, Cr and Mn exhibit an embrittling effect on P-induced grain boundary embrittlement. However, P is less electronegative with respect to Ni than to Fe. Consequently, Ni does not enhance P-induced grain boundary embrittlement. Even though the interactions between I, A, and Fe were not included in the extended nonequilibrium model, it can be noted that the predicted results on Cr, Mn, and Ni from the extended model are consistent with the above results.

### III. EXPERIMENTAL PROCEDURES

The materials used in this study are high purity Fe-P, Fe-P-Mn, Fe-P-Mo, and Fe-P-W alloys prepared at the General Electric Research and Development Center in the form of hot rolled plates of 12.7 mm in thickness and 76.2 mm in width. The chemical compositions of these alloys were analyzed by Anderson & Associates, Houston, Texas and Chicago Spectro Service Laboratory, Chicago, Illinois. The analyzed chemical compositions of the alloys are shown in Table III.

The reasons for choosing these alloys are the following:

1. Among the well-known grain boundary embrittling impurities (*i.e.*, As, P, S, Sb, Sn, *etc.*), P is the most common impurity in commercial Fe alloys. Hence, the study on P grain boundary segregation and its effect on grain boundary embrittlement is of practical importance.
2. As discussed earlier, the extended model suggests the remedial effect of Mo and W and the embrittling effect of Mn on P-induced grain boundary embrittlement. Therefore, the P-doped Fe alloys that individually contain Mn, Mo, or W were selected in order to evaluate experimentally the extended model.
3. C often causes a complex situation in grain boundary embrittlement studies by segregating to grain boundaries in elemental form and/or by precipitating at grain boundaries in the form of carbides. Hence, the low C content Fe alloys as shown in Table III were chosen to avoid this complex situation.
4. Finally, the effect of alloying elements on impurity-induced grain boundary embrittlement may arise not only from the direct effect but also from the indirect effect. Therefore, for careful study on the indirect effect of Mn, Mo, and W, the level of P grain boundary segregation in the ternary Fe-P-Mn, Fe-P-Mo, and Fe-P-W alloys are to be compared to that in the binary Fe-P alloy.

For heat treatments the plates were cut into the rectangular blocks of 12.7 mm  $\times$  21.4 mm  $\times$  76.2 mm. As pointed out previously,<sup>31,32</sup> the mechanical-structural factors such as hardness, grain size, morphology of grain boundary, and type of microstructure are important variables controlling grain boundary embrittlement. Since the main purpose of this study is to investigate the effect of P, Mn, Mo, and W grain boundary segregation on the grain boundary strength, it would be desirable not to have variables of the mechanical-structural factors. Therefore, the first heat

Table III. The Chemical Compositions of Materials (Wt Pct)

Element	Fe-P		Fe-P-Mn		Fe-P-Mo		Fe-P-W	
	(a)	(b)	(a)	(b)	(a)	(b)	(a)	(b)
B	0.0003		<0.0001		0.002		0.001	
C	0.001	0.001	0.011	0.0080	0.008	0.0080	0.014	0.0090
P	0.1	0.057	0.1		0.1		0.1	
S	0.003	<0.005	0.004		0.003		0.005	
Si	0.008	0.01	0.005		0.068		0.015	
Al	<0.0006		<0.0006		0.02		<0.0006	
Co	<0.002		<0.002		<0.002		0.005	
Cr	0.004	0.01	0.018		0.005		0.011	
Cu	<0.0009	<0.01	<0.0009		<0.0009		<0.0009	
Mn	0.01	0.01	2.6		0.034		0.015	
Mo	0.004	<0.01	0.08		3.2		0.034	
Nb	<0.005		<0.005		<0.005		<0.005	
Ni	0.03	0.01	0.075		0.03		0.03	
Pb	<0.0001		<0.0001		0.008		0.001	
Ti	0.003		0.002		0.01		0.004	
V	0.002		0.004		0.003		0.006	
W	<0.0004		0.008		0.031		4.6	

\*(a) reported from Anderson & Associates, Inc.

(b) reported from Chicago Spectro Service Laboratory, Inc.

treatment was intended to develop the same grain size for all the alloys. However, this could not be achieved due to the following reasons:

1. After grain size control treatment, the Fe-P and Fe-P-Mn alloys exhibit a phase transformation during cooling, while the Fe-P-Mo and Fe-P-W alloys remain in the same phase.
2. The conditions of the as-received alloys were too different. The Fe-P and Fe-P-Mn alloys had a very fine and equiaxed grain structure, while the Fe-P-Mo and Fe-P-W alloys had a very large and elongated grain structure.

Hence, the resulting grain size of the Fe-P-Mn alloy is significantly smaller when compared to those of the Fe-P, Fe-P-Mo, and Fe-P-W alloys. The problems arising from the grain size difference will be discussed later. The grain size control treatment was followed by tempering and aging treatments to vary the level of P, Mn, Mo, and W grain boundary segregation. The heat treatment conditions of the alloys are shown in Figure 3. In order to identify the type of alloy, aging temperature, and aging time, the specimens were designated with 5-digit numbers as:

	X X X X X		
type of alloy	aging temperature	aging time	
0: Fe-P	40:400 °C	01:10 hrs	
1: Fe-P-Mn	45:450	03:30	
2: Fe-P-Mo	50:500	10:100	
3: Fe-P-W	55:550	30:300	
	60:600		

After each heat treatment a hardness measurement was made in HRB scale using a Wilson Rockwell hardness tester.

Recently, Kameda *et al.*<sup>3,4</sup> have developed a direct method to determine the critical local tensile stress necessary for the grain boundary brittle crack initiation ( $\sigma_c$ ) using 4-point slow bend tests and tension tests, in conjunction with the Griffiths-Owen finite element elastic-plastic stress analysis.<sup>33</sup> In this study, the method developed by Kameda *et al.* will be adopted in order to determine the effect of P,

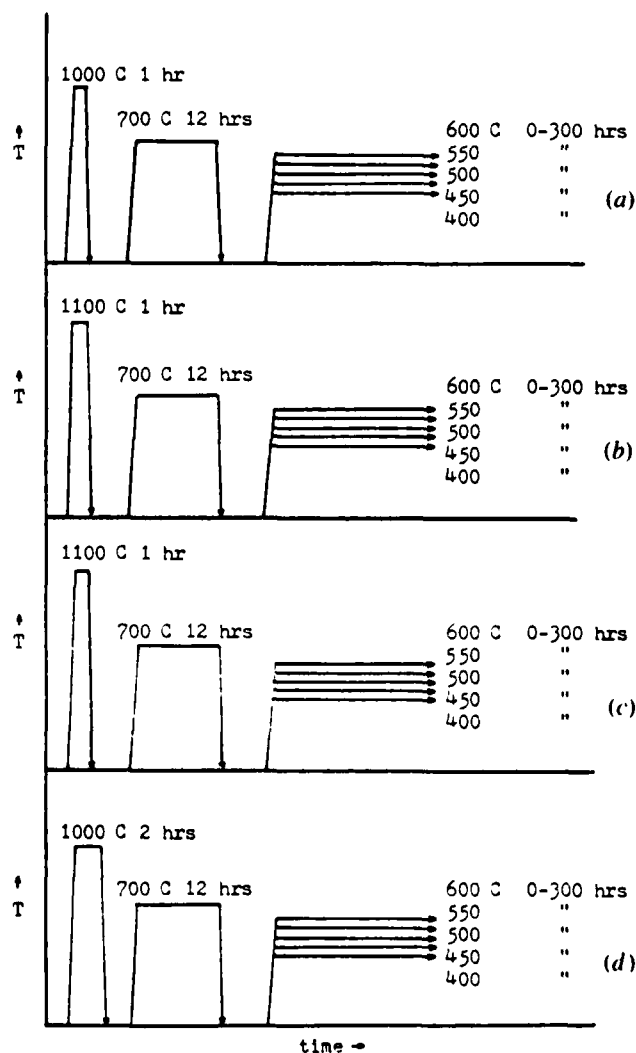


Fig. 3—Conditions of heat treatment for the (a) Fe-P, (b) Fe-P-Mn, (c) Fe-P-Mo, and (d) Fe-P-W alloys.



Mn, Mo, or W grain boundary segregation on the grain boundary strength. Hence, after heat treatments and hardness measurements, each rectangular block was cut into a notched bend test specimen and an unnotched tension test specimen. The geometry of the notched bend test specimen is the same as that used in the Griffiths-Owen analysis.

Both bend and tension tests were conducted using an Instron universal testing machine. The primary test temperatures were  $-140^{\circ}\text{C}$  for Fe-P and Fe-P-Mn alloys and  $-100^{\circ}\text{C}$  for Fe-P-Mo and Fe-P-W alloys. These test temperatures were chosen so the specimens fractured at initial yielding, but before general yielding in the bend test. In order to find the above test temperatures and the temperature dependence of yield stress ( $\sigma_y$ ), some of the specimens of each alloy were tested over the temperature range of  $-196^{\circ}\text{C}$  to room temperature. All the test temperatures were obtained by controlling the amount of liquid nitrogen per unit time sprayed to the specimen and were monitored by a thermocouple embedded in the specimen. Cross-head speeds were 0.5 mm per minute for bend tests and 2 mm per minute for tension tests.

In order to determine the mode of fracture and the percentage of intergranular fracture (pct IF), the fractured bend test specimens were examined using scanning electron microscopy (SEM). For the estimation of pct IF, three SEM fractographs were taken for each specimen from the fracture surfaces located near the notch root in the center region of the specimen. Since the main interest is to find the fracture behavior in the area under  $\sigma_y$ , the distance from the notch root to the area where  $\sigma_y$  occurred ( $D_y$ ) was determined for each specimen from the obtained nominal bending stress

( $\sigma_{nom}$ ),  $\sigma_y$ , and the Griffiths-Owen analysis. Then, the line indicating the location of  $\sigma_y$  was drawn on the SEM fractograph. The pct IF was estimated by measuring the length of the line occupied by intergranular fracture surfaces. Figure 4 shows the examples of the fractographs used in the pct IF estimation.

For the determination of P, Mn, Mo, and W grain boundary concentration, Auger electron spectroscopy (AES) was employed. The Auger samples were prepared from the fractured bend test specimens. Auger samples were fractured *in situ* at the pressure of about  $10^{-8}$  Pa and at the temperature of about  $-30^{\circ}\text{C}$  in the ultrahigh vacuum chamber of a scanning Auger spectrometer (Physical Electronics Industries model PHI 590). Auger spectra from the individual grain boundary facets were recorded as  $dN(E)/dE$  vs  $E$  under the following conditions: 5 KeV, 300 to 500 nA, 2  $\mu\text{m}$  primary beam; 3 V peak-to-peak modulation; 3 eV per second sweep rate; 0.3 second time constant. From the obtained Auger spectra quantitative estimates of grain boundary chemistry were made based on the method given in Reference 34. Auger sputtering depth profiles were also taken to examine whether P, Mn, Mo, and W are segregated locally at grain boundaries or tied up in a three dimensional (3D) second phase.

#### IV. RESULTS AND DISCUSSION

##### A. The Effect of Mn, Mo, and W on P Grain Boundary Segregation

As shown in Figure 5 the Auger sputtering depth profiles show that P, Mn, Mo, and W are concentrated locally at

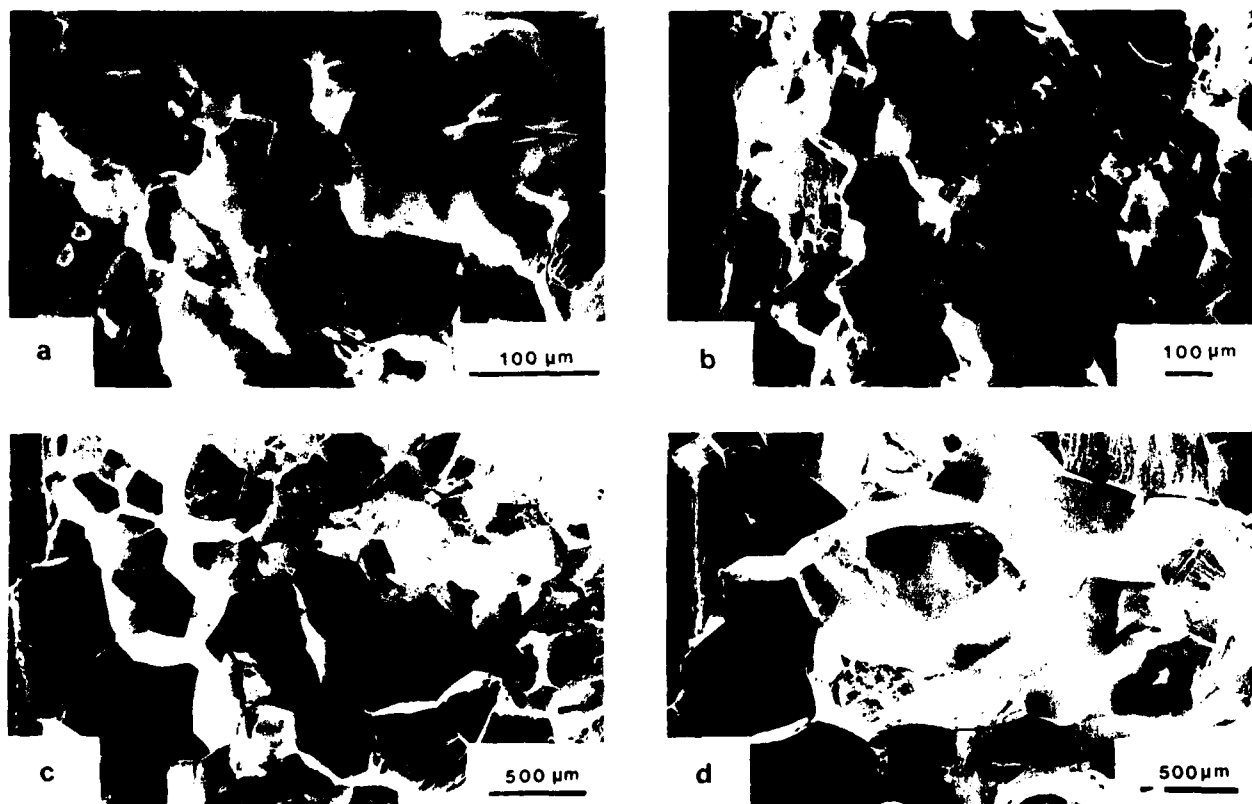


Fig. 4—Examples of the fractographs used in the estimation of the pct IF. (a) 05030, (b) 15530, (c) 25003, and (d) 35001 specimens.

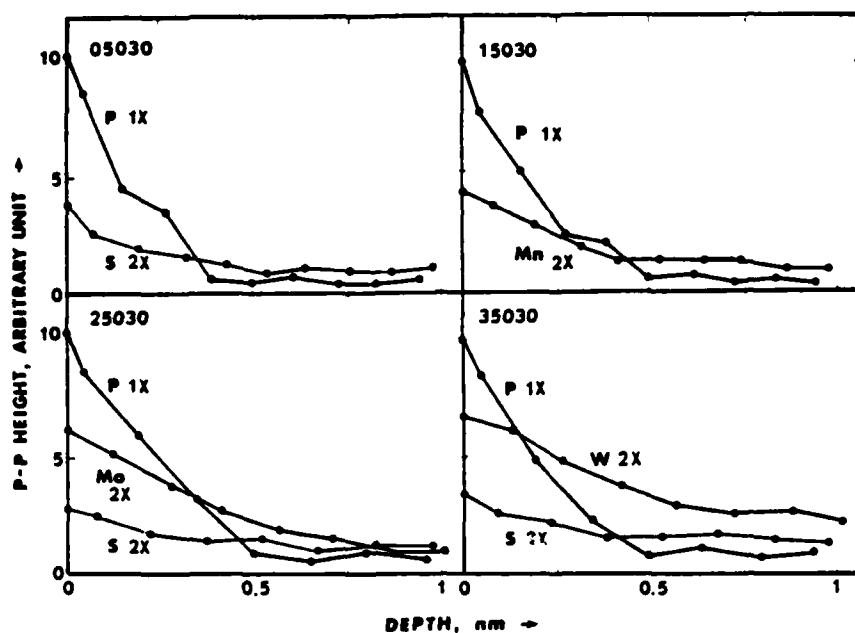


Fig. 5—Examples of the Auger sputtering depth profiles.

grain boundaries. This suggests that P, Mn, Mo, and W segregated at grain boundaries are not tied up in a 3D second phase. If they formed a 3D second phase at grain boundaries, their concentration profiles would extend over a much greater distance. The concentration profiles of Mo and W extend a little more than those of P and Mn. This is assumed to be because of the slower sputtering rate of Mo and W as pointed out previously by Schmerling *et al.*<sup>35</sup> It should be noted that this reduced sputtering rate of Mo or W would be expected from the grain boundary cohesive energy change associated with Mo and W grain boundary segregation. As described earlier, the grain boundary cohesive energy increases with Mo or W grain boundary segregation but decreases with P or Mn grain boundary segregation.

From Figure 5 it can be noted that a small amount of S grain boundary segregation occurs in the Fe-P, Fe-P-Mo, and Fe-P-W alloys, while S does not segregate to grain boundaries in the Fe-P-Mn alloy even though the S matrix concentration is virtually the same for all the alloys (Table III). It has been recognized that due to the very strong attractive S-Mn interaction, S is in general completely precipitated in the matrix of an Fe alloy containing Mn. This is why S does not participate in the grain boundary embrittlement problems of commercial Fe alloys which always contain a certain amount of Mn for that purpose.

The variations of P, Mn, Mo, and W grain boundary segregation are plotted as a function of aging time in Figure 6 and as a function of aging temperature in Figure 7. Each data point in Figures 6 and 7 represents the average of about 10 grain boundaries. As expected, it is found from Figure 6 that at the aging temperature of 500 °C, P, Mn, Mo, or W grain boundary segregation increases with increasing aging time. It is also found from Figure 7 that with 300 hours aging the maximum P grain boundary segregation occurs at the aging temperature of 500 °C for all the alloys. Seah's recent study<sup>36</sup> on the kinetics of P grain boundary segregation in an Fe-Cr-Ni-C alloy has also shown

that with 300 hours aging the maximum P grain boundary segregation can be obtained at the aging temperature of about 500 °C. In the case of alloying elements it can be seen from Figure 7 that the aging temperature for the maximum grain boundary segregation after 300 hours aging is also 500 °C for Mo and W, but is 550 °C for Mn.

From Figures 6 and 7 it can be seen that for a given aging treatment the amount of Mn, Mo, or W grain boundary segregation is somewhat less than that of P grain boundary segregation even though the Mn, Mo, or W matrix concentration is much higher than P. This suggests that Mn, Mo, or W possesses a much lower grain boundary segregation enrichment ratio than P. Here, it should be noted from Figure 6 that in the early stages of aging the grain boundary segregation rate of Mn, Mo, or W is apparently slower than that of P.

It has been believed that impurity grain boundary segregation is influenced by the presence of alloying elements in Fe alloys due to the existence of *I-A* interaction. The *I-A* interaction and its effect on impurity grain boundary segregation have been explained by the Guttman model.<sup>2</sup> According to the Guttman model, Cr, Mn, and Ni enhance impurity grain boundary segregation by cosegregating with the impurity to grain boundaries due to their moderate attractive *I-A* interaction, while Mo, Ti, V, W, and Zr reduce impurity grain boundary segregation by precipitating the impurity in the matrix due to their strong attractive *I-A* interaction. It was therefore expected that when the Fe-P, Fe-P-Mn, Fe-P-Mo, and Fe-P-W alloys were selected for this study, P grain boundary segregation would be enhanced in the Fe-P-Mn alloy and would be reduced in the Fe-P-Mo and Fe-P-W alloys compared to P grain boundary segregation in the Fe-P alloy. However, it is of great interest to note from Figure 8 that for a given aging treatment the level of grain boundary segregation is basically the same for all the alloys. This fact could suggest that P grain boundary segregation is not affected by the presence of Mn, Mo, or W,

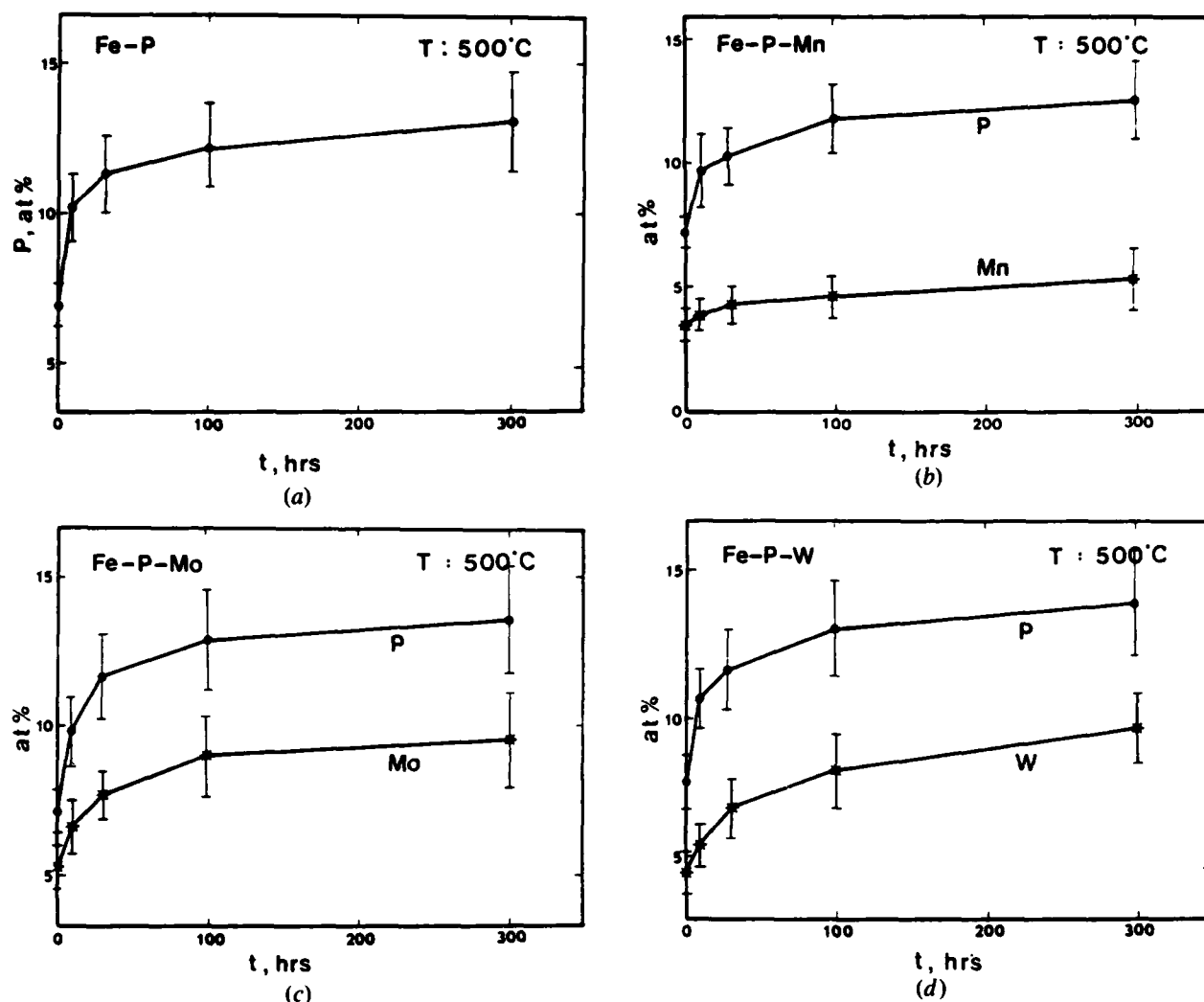


Fig. 6—The variation of P, Mn, Mo, or W grain boundary segregation with aging time in the (a) Fe-P, (b) Fe-P-Mn, (c) Fe-P-Mo, and (d) Fe-P-W alloys.

and that Mn, Mo, or W does segregate to grain boundaries simultaneously with P but independently of P. Since the alloys have different grain size, the P diffusion distances must be considered in order to examine if P grain boundary segregation may be affected by the difference in grain size. Gruzin and Minal<sup>37</sup> have obtained the diffusivity of P in Fe as:

$$D_P^{\text{Fe}} = 7 \times 10^{-7} \exp(-20,130/T) \text{ m}^2/\text{sec} \quad [3]$$

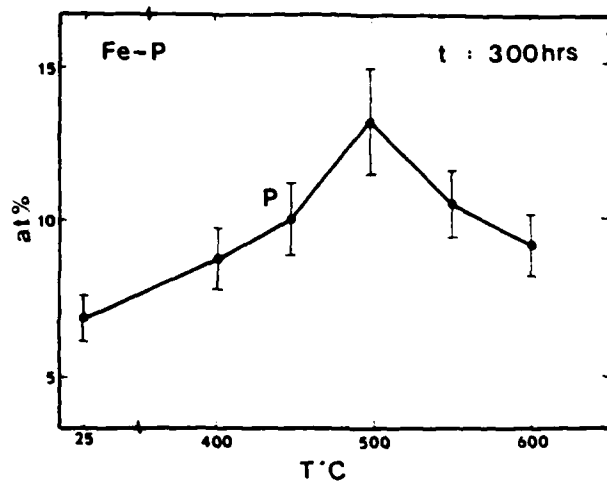
With 300 hours aging treatment the calculated P diffusion distances are 0.28  $\mu\text{m}$  and 8.55  $\mu\text{m}$  for the aging temperatures of 400 and 600  $^{\circ}\text{C}$ , respectively. These values are much less than the grain diameters of the alloys used in this study. The grain diameters of the alloys are 50 to 700  $\mu\text{m}$  as shown in Figure 4. Therefore, the grain size effect on P grain boundary segregation would be negligible even though the grain boundary area/volume ratio varies with grain size. Based upon his experimental study on the grain size effect, Guttman<sup>31</sup> has also claimed that grain boundary segregation itself does not vary with grain size.

Recently, Briant<sup>38</sup> has conducted a grain boundary segregation study by systematically varying the matrix concen-

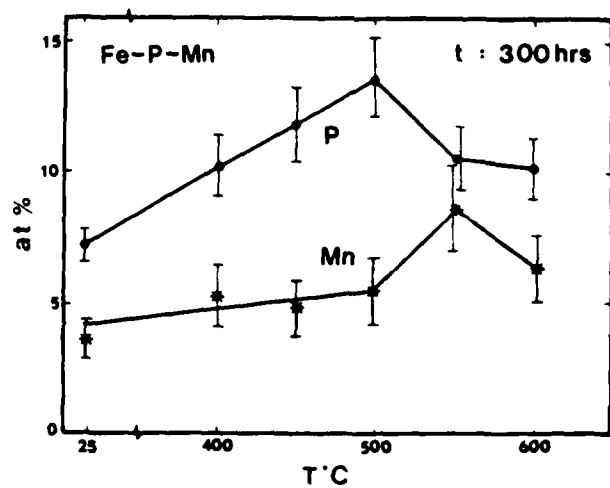
trations of Cr, Mn, and Ni in P-doped Fe alloys. His results have also shown that the changes in the matrix concentrations of Cr, Mn, and Ni do not influence P grain boundary segregation. Based upon his experimental results, he has claimed that P grain boundary segregation is independent of Cr, Mn, and Ni grain boundary segregation. Hence, it can be concluded from the results of this study and of Briant's that P and alloying elements segregate to grain boundaries independently and that P grain boundary segregation is thereby not influenced by the presence of alloying elements.

#### B. The Effect of Mn, Mo, and W on Grain Boundary Embrittlement

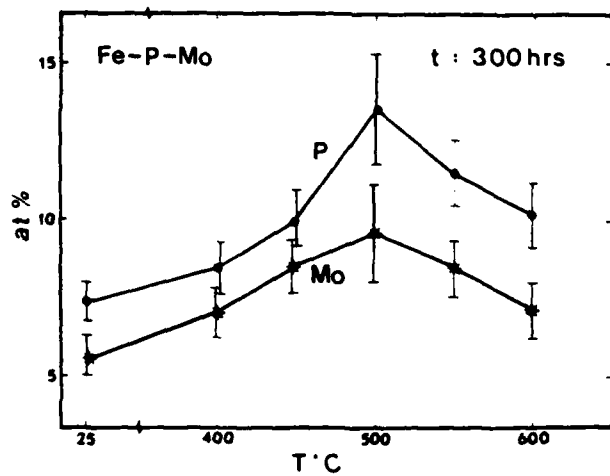
As mentioned earlier, the mechanical-structural factors which are also very important variables controlling grain boundary embrittlement could not be effectively controlled in this study; the Fe-P, Fe-P-Mn, Fe-P-Mo, and Fe-P-W alloys have different grain size and hardness. However, the values of grain size and hardness are virtually identical for all the specimens of each alloy after the different aging treatments. Therefore, it is intended that in the following



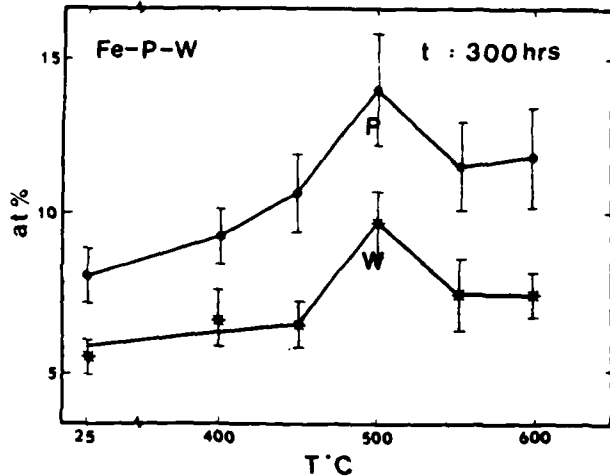
(a)



(b)

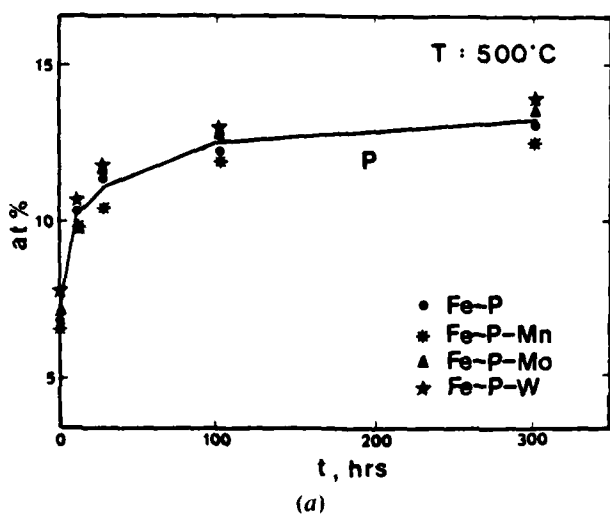


(c)

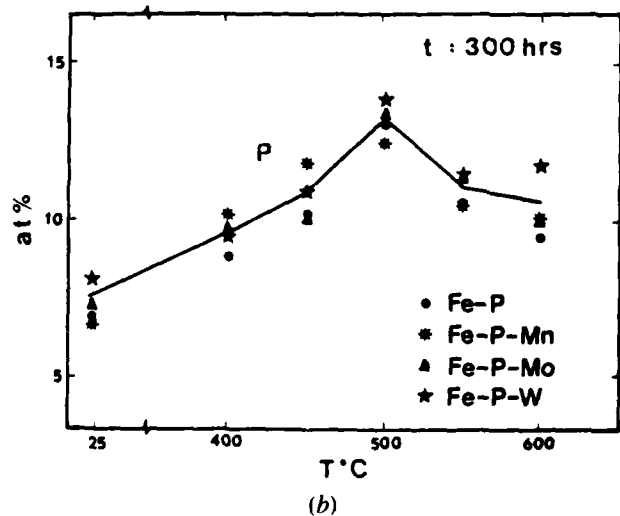


(d)

Fig. 7—The variation of P, Mn, Mo, or W grain boundary segregation with aging temperature in the (a) Fe-P, (b) Fe-P-Mn, (c) Fe-P-Mo, and (d) Fe-P-W alloys.



(a)



(b)

Fig. 8—The variation of P grain boundary segregation (a) with aging time and (b) with aging temperature in the Fe-P, Fe-P-Mn, Fe-P-Mo, and Fe-P-W alloys.

discussion the comparison of the experimental results will focus on the individual alloys.

The results of hardness, bend, and tension tests are summarized in Table IV. It can be seen that for a given test temperature  $\sigma_y$  is virtually identical for all the specimens of each alloy, but varies with the test temperature. Figure 9 shows that the temperature dependence of  $\sigma_y$  becomes large at the test temperature below about  $-100^\circ\text{C}$  and that the

large temperature dependence for the Fe-P-Mo and Fe-P-W alloys occurs at higher test temperatures than those for the Fe-P and Fe-P-Mn alloys.

From the values of  $\sigma_{nom}$  and  $\sigma_y$  in Table IV, the critical local tensile stress necessary for the grain boundary brittle crack initiation ( $\sigma_c$ ) and the distance from the notch root to the region of  $\sigma_c(D_c)$  were calculated using the Griffiths-Owen analysis.<sup>33</sup> Figure 10 shows the variations of  $\sigma_c$  and

Table IV. Hardness, Bend, and Tension Test Results of the Fe-P, Fe-P-Mn, Fe-P-Mo, and Fe-P-W Alloys

Specimen	HRB	$T(^{\circ}\text{C})$	$\sigma_{nom}$ (MPa)	Pct IF	$T(^{\circ}\text{C})$	$\sigma_y$ (MPa)	$\sigma_{fr}$ (MPa)	Pct e
00000	38	-140	527	53	-140	305	409	1.9
04001	38	-196	623	*	-160	419	446	1.1
04003	36	-140	511	61	25	119	131	59.2
04010	40	-100	*	*	-80	161	*	*
04030	36	-140	494	58	-140	305	397	2.9
04503	37	-140	460	57	-140	293	335	1.1
04510	39	-140	482	67	-140	300	310	0.9
04530	34	-140	490	57	-140	300	305	0.9
05001	38	-196	603	*	-140	300	325	1.0
05003	38	-140	482	70	-140	300	312	0.9
05010	38	-140	423	85	-140	*	268	0.7
05030	35	-140	393	98	-140	*	260	0.6
05501	39	-140	494	68	-160	*	365	0.8
05503	38	-140	473	75	*	*	*	*
05510	37	-140	489	74	-80	149	*	*
05530	37	-140	460	75	-140	303	315	0.9
06001	38	-140	519	50	-160	*	355	0.8
06003	37	-140	519	82	-80	156	*	*
06010	36	-140	519	61	*	*	*	*
06030	36	-140	511	95	-140	298	360	1.2
10000	68	-140	887	32	-140	379	689	4.4
14001	64	-120	*	*	-160	476	707	2.3
14003	65	-196	536	*	-100	273	*	*
14010	65	-196	493	*	*	*	*	*
14030	65	-140	783	45	-140	367	675	4.2
14503	64	-140	858	48	*	*	*	*
14510	65	-140	741	49	-160	471	471	1.0
14530	65	-140	720	46	-140	379	694	4.0
15001	66	-140	728	42	-140	419	699	3.5
15003	66	-140	657	48	-140	434	665	3.4
15010	65	-140	603	60	-140	432	594	2.5
15030	66	-140	544	79	-140	429	558	1.6
15503	66	-140	720	38	*	*	*	*
15510	66	-140	552	58	*	*	*	*
15530	66	-140	502	81	-140	402	511	1.5
16003	66	-196	552	*	*	*	*	*
16010	65	-196	460	*	25	181	179	49.9
16030	59	-140	695	53	-140	362	684	3.1
20000	68	-100	561	38	-100	315	454	2.2
24010	67	-100	490	39	-120	377	389	0.9
24030	68	-100	531	34	-100	315	422	1.8
24501	67	-80	*	*	-140	*	377	0.7
24503	68	-100	494	41	-80	265	434	3.1
24510	67	-100	536	45	-80	263	417	2.2
24530	68	-100	557	36	-100	327	434	1.8
25001	68	-100	473	47	-100	310	360	1.2
25003	67	-100	419	55	-100	*	285	0.6
25010	68	-100	485	48	-100	308	315	0.9
25030	67	-100	502	40	-100	310	402	1.5
25501	69	-100	515	33	-100	*	407	0.8
25503	65	-100	427	26	-100	*	288	0.7
25510	69	-100	494	45	-100	325	404	1.3
25530	67	-100	523	41	-100	320	417	1.7
26001	68	-120	737	*	25	146	298	43.5
26003	67	-80	*	*	-50	206	*	*
26010	70	-100	490	35	*	*	*	*

Table IV. Cont. Hardness, Bend, and Tension Test Results of the Fe-P, Fe-P-Mn, Fe-P-Mo, and Fe-P-W Alloys

Specimen	HRB	$T(^{\circ}\text{C})$	$\sigma_{nom}$ (MPa)	Pct IF	$T(^{\circ}\text{C})$	$\sigma_y$ (MPa)	$\sigma_{fr}$ (MPa)	Pct $e$
26030	70	-100	494	28	-100	310	417	1.5
30000	71	-100	674	41	-100	342	449	1.8
34001	70	-100	728	31	-160	*	429	0.9
34003	71	-100	661	38	-80	270	441	3.8
34010	71	-100	670	44	*	*	*	*
34030	67	-100	720	44	-100	340	417	1.2
34501	70	-100	707	46	-120	397	414	1.0
34503	69	-100	665	36	-80	253	*	*
34510	72	-100	665	43	*	*	*	*
34530	67	-100	661	60	-100	332	379	1.2
35001	68	-100	557	66	-100	*	332	0.7
35003	69	-100	636	50	-100	337	337	0.8
35010	70	-100	661	48	-100	337	402	1.1
35030	67	-100	674	46	-100	355	417	1.3
35503	71	-100	624	67	-100	*	310	0.7
35510	71	-100	653	55	-100	352	372	0.9
35530	70	-100	657	44	-100	340	389	1.0
36001	71	-100	619	28	25	154	347	39.9
36003	70	-100	628	53	-100	397	422	1.1
36010	71	-100	653	60	*	*	*	*
36030	71	-100	657	47	-100	337	409	1.2

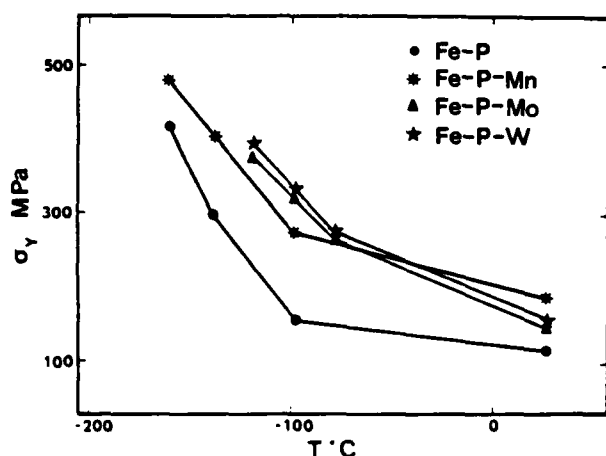


Fig. 9—The temperature dependence of yield stress in the Fe-P, Fe-P-Mn, Fe-P-Mo, and Fe-P-W alloys.

$D_c$  with aging time at the aging temperature of 500 °C. With increasing aging time, for the Fe-P and Fe-P-Mn alloys  $\sigma_c$  and  $D_c$  decrease in the whole range of aging time, but for the Fe-P-Mo and Fe-P-W alloys they decrease in the early stages of aging and then increase in the later stages of aging. The variations of  $\sigma_c$  and  $D_c$  with aging time in the Fe-P-Mo and Fe-P-W alloys look anomalous, but these could have arisen from the remedial effect of Mo or W on P-induced grain boundary embrittlement which can be predicted from the extended model; the earlier P grain boundary segregation weakens grain boundaries and the subsequent Mo or W grain boundary segregation strengthens the weakened grain boundaries. It was already noted from Figure 6 that in the early stages of aging the grain boundary segregation rate of P is apparently faster than that of Mo or W. The remedial effect of Mo and W will be further considered later.

It can be noted from Table IV that for each alloy the values of  $\sigma_{nom}$ , tensile fracture stress ( $\sigma_{fr}$ ), and pct elongation (pct  $e$ ) show the similar variations with aging time to those of  $\sigma_c$  and  $D_c$ , while the variation of pct IF with aging time shows the very opposite of those of  $\sigma_c$ ,  $D_c$ ,  $\sigma_{nom}$ ,  $\sigma_{fr}$ , and pct  $e$ .

Before  $\sigma_c$  is correlated to the P, Mn, Mo, and W grain boundary segregation to observe the effect of P, Mn, Mo, and W grain boundary segregation on the change in  $\sigma_c$ , it needs to be briefly considered how  $\sigma_c$  can be regarded as the grain boundary strength. It has been suggested that brittle fracture in a deformable solid may be thought of as a three-stage process which can lead to a three-fold fracture criterion.<sup>3</sup> The three stages are the following:

1. A microcrack nucleates at an obstacle (*i.e.*, a second phase precipitate, inclusion, grain boundary, *etc.*) due to the blockage of a slip band or twin. For this first stage, at least local yielding is required.
2. The microcrack initiates its propagation beyond the obstacle. Hence, a certain value of  $\sigma_{22}^{max} = \sigma_c$  is required depending on the plastic work of fracture ( $\gamma_p$ ).
3. The propagating microcrack leads to the long range propagation. This depends on the gradient in the maximum principal stress.

Now, the above three-fold fracture criterion will be combined with the following assumptions:<sup>4</sup>

1. There is one grain boundary facet per grain which is oriented essentially normal to  $\sigma_{22}$ .
2. The nucleated microcrack initiates its propagation along the embrittled grain boundary in the region of  $\sigma_{22}^{max}$ .
3. The first grain boundary along which the microcrack propagates triggers unstable fracture of the specimen.

Then,  $\sigma_c$  can be considered as the critical local tensile stress necessary for the initiation of the grain boundary brittle fracture which is equivalent to the grain boundary strength.

Recently, Jokl *et al.*<sup>39,40</sup> have developed a Griffith-type fracture criterion assuming that the two processes of bond

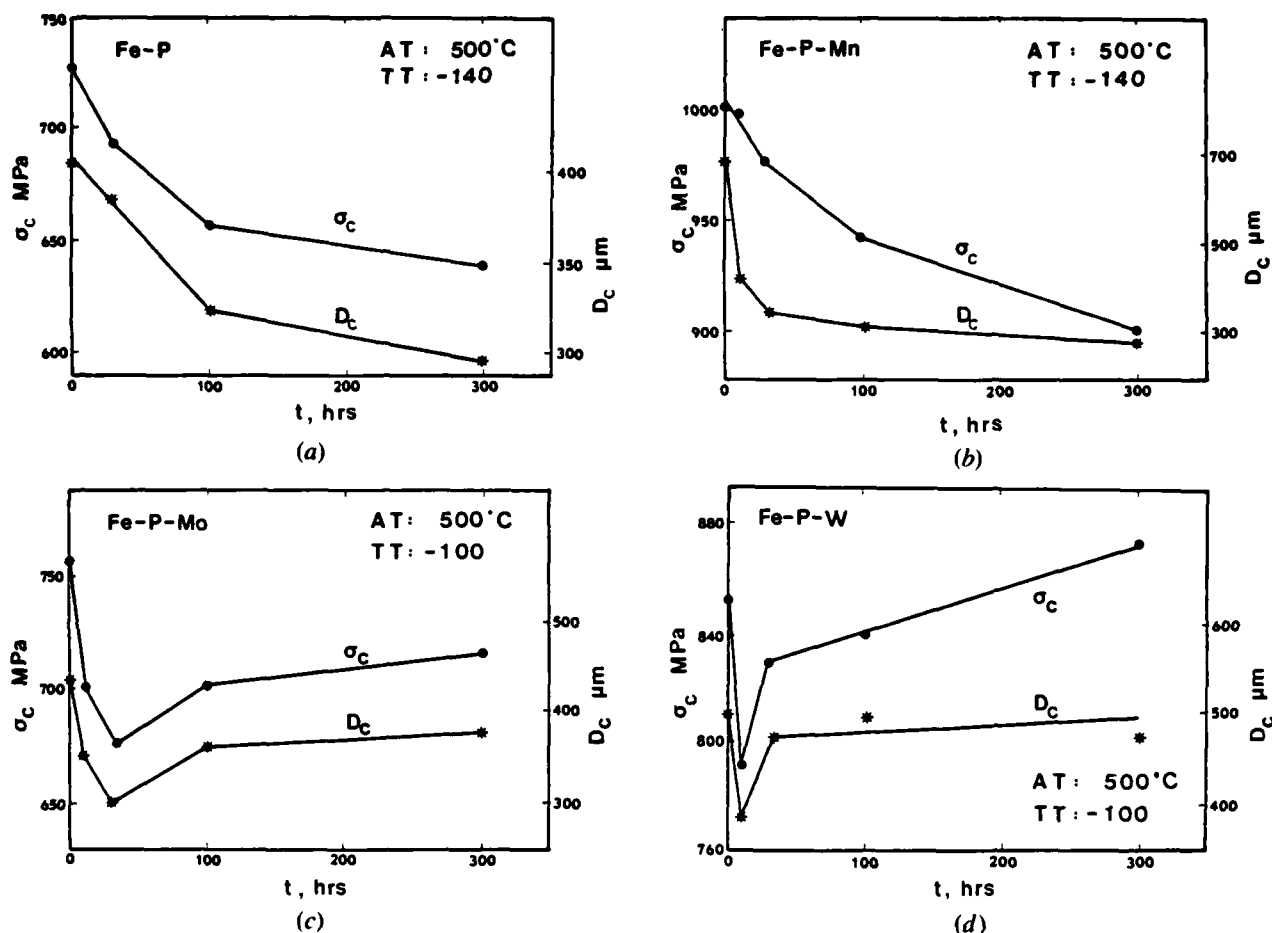


Fig. 10—The variations of the critical local tensile stress for grain boundary brittle crack initiation ( $\sigma_c$ ) and the distance from the notch root to the region of  $\sigma_c$  with aging time in the (a) Fe-P, (b) Fe-P-Mn, (c) Fe-P-Mo, and (d) Fe-P-W alloys.

breaking and dislocation emission occur concomitantly at the tip of a microcrack during brittle fracture of a deformable solid. This criterion suggests that the plastic work of fracture and the microcrack stress intensity are directly related to the ideal work of fracture. They have also proposed that the microcrack stress intensity at fracture would be related to  $\sigma_c$  in the form:

$$k_{FR}^2 = (\sigma_c \sqrt{\pi c})^2 + [f(\sigma_c, c, l, \tau)]^2 \quad [4]$$

where  $c$  is the length of the microcrack,  $l$  is the length of the initial dislocation pile-up that nucleates the microcrack, and  $\tau$  is the lattice friction stress for dislocation motion. Therefore, it would be expected that the grain boundary strength is directly related to the ideal work of fracture which is equivalent to the grain boundary cohesive energy.

Combining the information of the grain boundary strength with the grain boundary chemistry, the variation of the grain boundary strength may be considered for each alloy as a function of the amount of P, Mn, Mo, or W grain boundary segregation. As mentioned earlier, a very small amount of S grain boundary segregation occurs in Fe-P, Fe-P-Mo, and Fe-P-W alloys. However, the amount of S grain boundary segregation does not much vary with different aging treatments for each alloy. Therefore, the effect of S on the grain boundary strength would be about the same for all the

specimens of each alloy, and the grain boundary strength change would mainly be attributed to the change in P, Mn, Mo, or W grain boundary segregation for the specimens of each alloy.

Figure 11 shows the variation of grain boundary strength with the amount of P grain boundary segregation. It can be seen that the grain boundary strength decreases with increasing P grain boundary segregation in the Fe-P alloy and in the Fe-P-Mn, Fe-P-Mo, or Fe-P-W alloy for a given Mn, Mo, or W grain boundary segregation. The variation of the grain boundary strength is plotted for the Fe-P-Mn, Fe-P-Mo, or Fe-P-W alloy as a function of Mn, Mo, or W grain boundary segregation in Figure 12. It can be noted from Figure 12 that for a given P grain boundary segregation the grain boundary strength decreases with increasing Mn grain boundary segregation and increases with increasing Mo or W grain boundary segregation. Since, as discussed earlier, the grain boundary cohesive energy would be directly related to the grain boundary strength, the grain boundary cohesive energy would show the similar variation with P, Mn, or W grain boundary segregation to that of the grain boundary strength; the grain boundary cohesive energy would decrease with increasing P or Mn grain boundary segregation and would increase with increasing Mo or W grain boundary segregation. These experimental

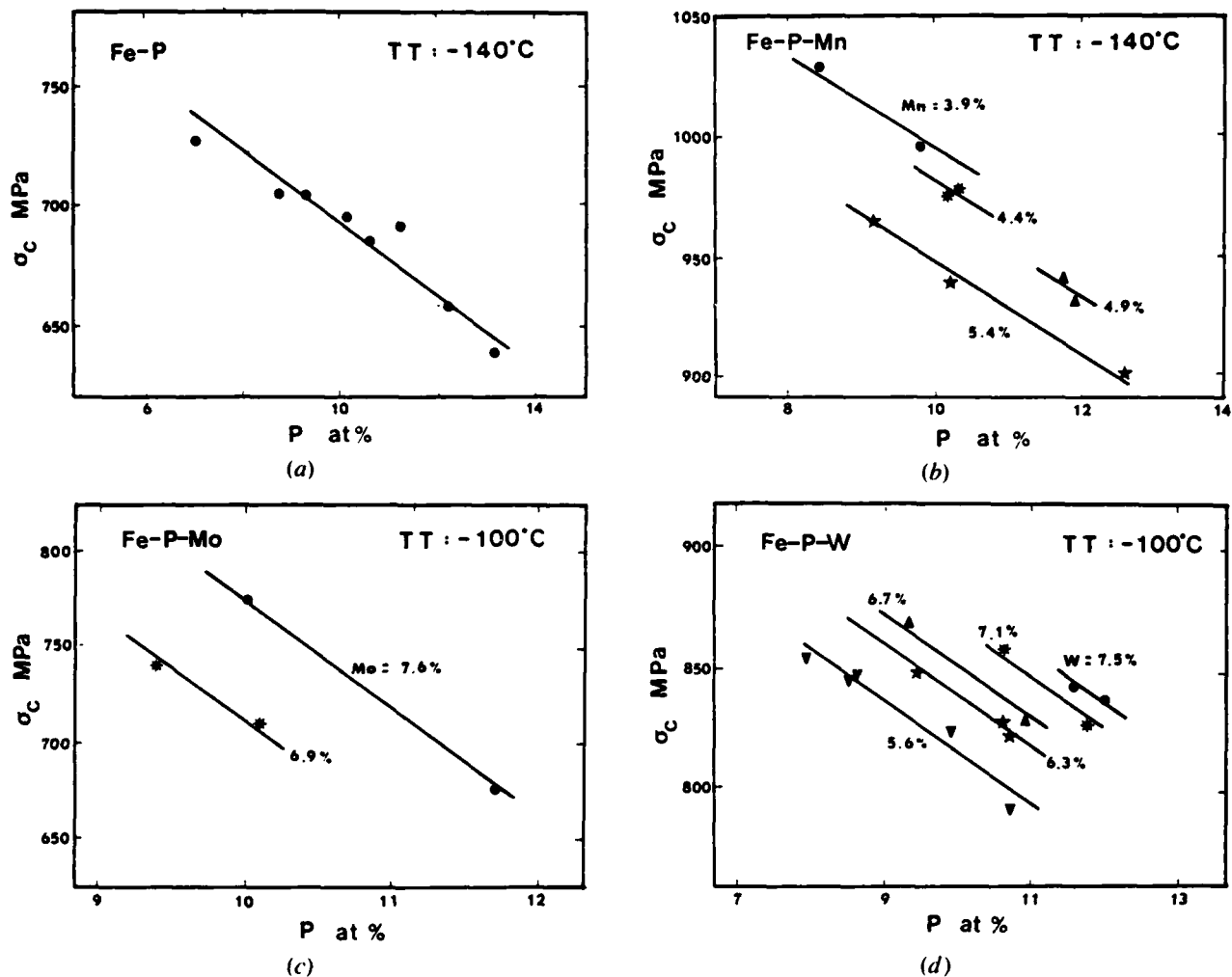


Fig. 11 — The variation of the grain boundary strength with P grain boundary segregation in the (a) Fe-P, (b) Fe-P-Mn, (c) Fe-P-Mo, and (d) Fe-P-W alloys.

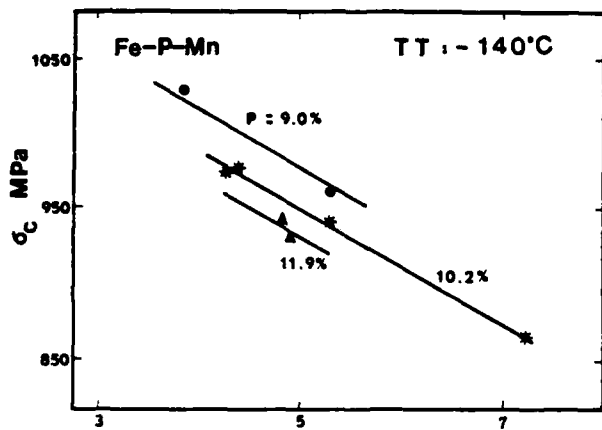
results are consistent with the original and extended nonequilibrium models. The reduced grain boundary cohesive energy due to P grain boundary segregation was predicted from the original model, and the embrittling effect of Mn and the remedial effect of Mo and W on P-induced grain boundary embrittlement in the Fe-P-Mn, Fe-P-Mo, and Fe-P-W alloys were predicted from the extended model.

As discussed previously, the effect of alloying elements on P-induced grain boundary embrittlement could also be explained by the effect of alloying elements on the P embrittling potency determined by their relative electronegativities to P and Fe.<sup>30</sup> This idea could be promising to reveal the interaction between impurities and alloying elements at the grain boundary and its effect on grain boundary embrittlement. This study did not intend to confirm experimentally this idea. The results from an AES and ionization loss spectroscopy study have suggested some evidences of the above effect, but still are not quite satisfactory.<sup>26</sup> More research efforts are necessary to establish fully the *I-A* cross-effect on the embrittling and remedial effects of impurities and alloying elements.

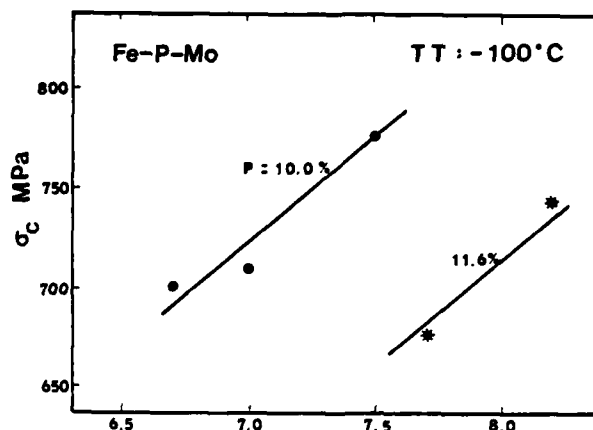
## V. CONCLUSIONS

1. The extended nonequilibrium model can directly and simply predict the effect of alloying elements on the impurity-induced grain boundary embrittlement in terms of the grain boundary cohesive energy. The extended model suggests that Mo, W, and Zr strongly reduce, Ni, Ti, and V slightly reduce, and Cr and Mn enhance impurity-induced grain boundary embrittlement in an Fe-*I-A* system. In this study the predictions were made only for an Fe-*I-A* system, but the extended model can be applied to all the materials which encounter a grain boundary embrittlement problem associated with grain boundary segregation of the substitutional solutes. This model is also applied to the impurity-induced interfacial embrittlement in a metal matrix composite containing low impurity solubility fibers.
2. The experimental results on the Fe-P, Fe-P-Mn, Fe-P-Mo, and Fe-P-W alloys show that for a given P grain boundary segregation the grain boundary strength decreases with the Mn grain boundary segregation and

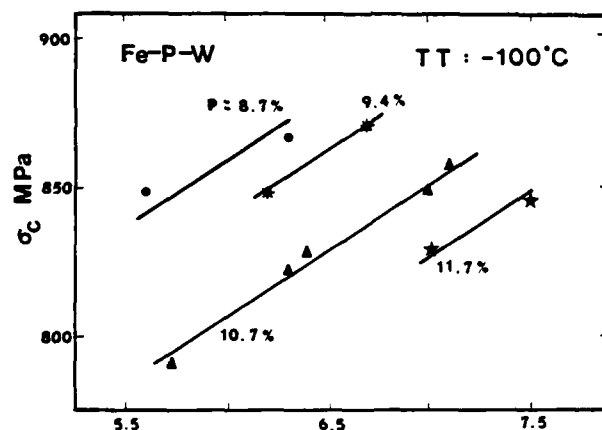




(a)



(b)



(c)

Fig. 12—The variation of the grain boundary strength with Mn, Mo, or W grain boundary segregation in the (a) Fe-P-Mn, (b) Fe-P-Mo, and (c) Fe-P-W alloys.

increases with Mo or W grain boundary segregation, which is consistent with the predictions from the extended model.

3. The grain boundary strength decreases with P grain boundary segregation in the binary Fe-P alloy. Also, for a given Mn, Mo, or W grain boundary segregation the grain boundary strength decreases with P grain segregation in the Fe-P-Mn, Fe-P-Mo, or Fe-P-W alloy.
4. P grain boundary segregation is not influenced by the presence of Mn, Mo, or W in the Fe alloy. Mn, Mo, or W grain boundary segregation occurs simultaneously with P grain boundary segregation; but Mn, Mo, or W grain boundary segregation is independent of P grain boundary segregation.
5. In the Fe-P, Fe-P-Mn, Fe-P-Mo, or Fe-P-W alloy, with 300 hours aging treatment, the maximum P, Mo, or W grain boundary segregation occurs at 500 °C, while the maximum Mn grain boundary segregation occurs at 550 °C.
6. In the early stages of aging treatment, the grain boundary segregation rate of Mn, Mo, or W is apparently slower than that of P in the Fe-P-Mn, Fe-P-Mo, or Fe-P-W alloy.
7. With increasing aging time at 500 °C, the grain boundary strength decreases for the Fe-P and Fe-P-Mn alloys; but for the Fe-P-Mo and Fe-P-W alloys the grain bound-

ary strength decreases in the early stages of aging and then increases in the later stages of aging. This anomalous variation in the Fe-P-Mo and Fe-P-W alloys is caused by the remedial effect of Mo and W on P-induced grain boundary embrittlement (*i.e.*, the earlier P grain boundary segregation weakens grain boundaries and then the subsequent Mo or W grain boundary segregation strengthens the weakened grain boundaries).

## APPENDIX A

### List of symbols

#### Superscript

- B* boundary region in a grain boundary (see Figure 1)  
*BM* boundary matrix interface region in a grain boundary (see Figure 1)  
*f* final state  
*F* fiber in a composite material  
*GB* grain boundary which consists of *B* and *BM*  
*i* initial state  
*I* interface region in a composite material (see Figure A1)  
*M* matrix (see Figures 1 and A1)  
*T* total system

#### Nomenclature

- A* interfacial area  
*c* microcrack length  
*d<sub>c</sub>* distance from the notch root to the region  $\sigma_c$

$D_p$	diffusion coefficient of P
$G$	Gibb's free energy
$H$	enthalpy
$H_j$	molar enthalpy of pure element $j$
$\bar{H}_j$	partial molar enthalpy of component $j$ ( $\bar{H}_j = \delta H / \delta N_j$ )
${}^m\bar{H}_j$	partial molar mixing enthalpy of component $j$ ( ${}^m\bar{H}_j = \bar{H}_j - H_j$ )
$H_j^*$	sublimation enthalpy of pure element $j$ per unit area
$k_{FR}$	microcrack stress intensity at fracture
$l$	length of the initial dislocation pile-up
$N_j$	number of moles of component $j$
$s$	interfacial tension
$S$	entropy
$X_j$	molar fractional monolayer of component $j$
$Z$	coordination number
$\gamma$	ideal work of fracture
$\mu_j$	chemical potential of component $j$
$\sigma_c$	critical local tensile stress
$\sigma_{fr}$	tensile fracture stress
$\sigma_{nom}$	nominal bending stress
$\sigma_y$	tensile yield stress
$\sigma_{22}^{max}$	maximum principal stress

## APPENDIX B

The extension of the nonequilibrium model to Fe-I-A ternary systems

By the definition of the Gibb's free energy (*i.e.*,  $G = H - TS$ ), the total Gibb's free energy change during the grain boundary segregation process can be expressed as:

$$\delta G^T = \delta H^T - T \delta S^T \quad [B1]$$

where  $H^T$  and  $S^T$  are total enthalpy and entropy of the system, respectively. Since the configuration entropy does not contribute to the grain boundary cohesive energy<sup>1</sup> and the contribution of the vibrational entropy to the grain boundary cohesive energy is negligible,<sup>7</sup> the enthalpy change in the grain boundary region during the grain boundary segregation process is equivalent to the grain boundary cohesive energy change associated with grain boundary segregation.

The total enthalpy of the system consisting of the boundary ( $B$ ), boundary matrix interface ( $BM$ ), and matrix ( $M$ ) regions as shown in Figure 1 can be described as the sum of the enthalpy of each region since enthalpy is an extensive thermodynamic variable:

$$H^T = H^B + H^{BM} + H^M \quad [B2]$$

From Eq. [B2] the total enthalpy change of the system during grain boundary segregation can be expressed as the sum of the enthalpy change of each region:

$$\delta H^T = \delta H^B + \delta H^{BM} + \delta H^M \quad [B3]$$

Here, we are mainly interested in the enthalpy change in the grain boundary region since this is directly equivalent to the grain boundary cohesive energy change associated with grain boundary segregation. Hence, by rearranging Eq. [B3], we obtain the grain boundary cohesive energy change associated with grain boundary segregation as:

$$\delta H^{GB} = \delta H^B + \delta H^{BM} = \delta H^T - \delta H^M \quad [B4]$$

The terms  $\delta H^T$  and  $\delta H^M$  in Eq. [B4] have been calculated by Stark and Marcus.<sup>1</sup> For a multi-component system the terms  $\delta H^T$  and  $\delta H^M$  can be expressed as:

$$\delta H^T = \delta H_*^B + \delta H_*^{BM} \quad [B5]$$

$$\delta H^M = \underline{H}_1^M \delta N_1^M + \sum_{j=2}^n \bar{H}_j^M \delta N_j^M \quad [B6]$$

where  $\underline{H}_1^M$  is the molar enthalpy of the pure solvent 1 in  $M$ ,  $\bar{H}_j^M$  is the partial molar enthalpy of the solute  $j$  in  $M$ ,  $\delta N_1^M$  is the change in the number of moles of 1 in  $M$ , and  $\delta N_j^M$  is that of  $j$  in  $M$ . The terms  $\delta H_*^B$  and  $\delta H_*^{BM}$  in Eq. [B5] are the enthalpy changes in  $B$  and  $BM$ , respectively, when  $B$  and  $BM$  are transformed from their initial high energy state to their final low energy state. This transformation is equivalent to the system undergoing grain boundary segregation as an attempt to obliterate the high grain boundary energy. A better understanding of these terms may be obtained from the details of the development of Eqs. [B5] and [B6] presented in Reference 1.

Assuming that each solute atom displaces one solvent atom from  $B$  or  $BM$  to  $M$  when solute atoms segregate from  $M$  to  $B$  or  $BM$ , we may find that the sum of the changes in the number of moles of solvent and solutes in  $M$  is zero:

$$\delta N_1^M + \sum_{j=2}^n \delta N_j^M = 0 \quad [B7]$$

The above assumption is at least approximately true for a grain boundary segregation process of the substitutional solutes. Therefore, the following analysis can be applied only to the substitutional solutes segregating to grain boundaries.

Substituting Eq. [B7] to Eq. [B6], we obtain:

$$\delta H^M = \sum_{j=2}^n (\bar{H}_j^M - \underline{H}_1^M) \delta N_j^M \quad [B8]$$

By using the partial molar mixing enthalpy term which is defined as  ${}^m\bar{H}_j^M = \bar{H}_j^M - \underline{H}_1^M$ , Eq. [B8] can be rewritten as:

$$\delta H^M = \sum_{j=2}^n ({}^m\bar{H}_j^M + \underline{H}_1^M - \underline{H}_1^M) \delta N_j^M \quad [B9]$$

Now, combining Eqs. [B4], [B5], and [B9], we may obtain the grain boundary cohesive energy change during grain boundary segregation for a multicomponent system as:

$$\begin{aligned} \delta H^{GB} &= \delta H^B + \delta H^{BM} \\ &= \delta H_*^B + \delta H_*^{BM} - \sum_{j=2}^n ({}^m\bar{H}_j^M + \underline{H}_1^M - \underline{H}_1^M) \delta N_j^M \end{aligned} \quad [B10]$$

The main purpose of this analysis is to study the effect of alloying elements on impurity-induced grain boundary embrittlement in Fe alloys. Hence, Eq. [B10] will be applied to an Fe-I-A ternary system. For an Fe-I-A ternary system, Eq. [B10] can be rewritten as:

$$\begin{aligned} \delta H^{GB} &= \delta H^B + \delta H^{BM} \\ &= \delta H_*^B + \delta H_*^{BM} - ({}^m\bar{H}_I^M + \underline{H}_I^M - \underline{H}_{Fe}^M) \delta N_I^M \\ &\quad - ({}^m\bar{H}_A^M + \underline{H}_A^M - \underline{H}_{Fe}^M) \delta N_A^M \end{aligned} \quad [B11]$$

By using Eq. [B11], it is now possible to estimate numerically the effect of alloying elements on impurity-induced grain boundary embrittlement using the published thermodynamical data on the molar enthalpies, the partial molar mixing enthalpies, and the measured grain boundary chemistry with the proper assumption on the terms  $\delta H^b_*$  and  $\delta H^{BM}_*$ .

## APPENDIX C

### The segregation effect on interfacial cohesion in composite materials

The nonequilibrium model which describes the influence of grain boundary segregation on the grain boundary cohesive energy can be applied to the interfacial embrittlement problems associated with impurity interfacial segregation in continuous fiber metal matrix composite materials. The nonequilibrium model has been modified for the application to composite materials<sup>41</sup> by adopting most of the basic assumptions used for the development of the nonequilibrium model with some other assumptions which are suitable for the nature of composite materials.

The total Gibbs free energy of a multicomponent system which consists of the matrix ( $M$ ), interface ( $I$ ), and fiber ( $F$ ) as shown in Figure A1 can be given as:

$$G^T = \sum_{j=1}^n \sum_k \mu_j^k N_j^k + s'A' \quad [C1]$$

where  $\mu_j^k$  is the chemical potential of component  $j$  in  $k$  ( $k = M, I, \text{ or } F$ ),  $N_j^k$  is the number of moles of  $j$  in  $k$ ,  $s'$  is the interfacial tension, and  $A'$  is the interfacial area. Assuming that  $F$  is made of pure element and defining that the component 1 is the solvent in  $M$ , the components 2 to  $n-1$  are the solutes in  $M$  and the component  $n$  is the element of pure solid  $F$ , we may rewrite Eq. [C1] as:

$$G^T = \sum_{j=1}^{n-1} \sum_q \mu_j^q N_j^q + \mu_n^F N_n^F + s'A' \quad [C2]$$

where  $q$  is  $M$  or  $I$ .

With the following three assumptions: (1) interfacial segregation takes place at the constant interfacial area, temperature, and pressure, (2) entropy production during the interfacial segregation process is negligible, and (3) no flux occurs between  $F$  and  $M$  or  $I$  during the interfacial segregation (i.e.,  $\mu_n^{IF} = \mu_n^{IF}$  and  $N_n^{IF} = N_n^{IF}$ ), we may describe the total Gibbs free energy change associated with interfacial segregation as:

$$\delta G^T = \sum_{j=1}^{n-1} \sum_q (\mu_j^{iq} N_j^{iq} - \mu_j^{if} N_j^{if}) + (s^{if} - s^{ii})A' \quad [C3]$$

where superscripts  $i$  and  $f$  represent the initial and final state, respectively. Following the derivation of the nonequilibrium

Matrix ( $M$ )	
Interface ( $I$ )	$s'$
Fiber ( $F$ )	
Interface ( $I$ )	$s'$
Matrix ( $M$ )	

Fig. A1—Model of the interface region in composite materials.

model,<sup>1</sup> the enthalpy change in the interface region can be written as:

$$\delta H^I = \delta H^I_* - \underline{H}^I_* \delta N^I_* - \sum_{j=2}^n \bar{H}^I_j \delta N^I_j \quad [C4]$$

Since the enthalpy change in the interface region during interfacial segregation is equivalent to the interfacial cohesive energy change associated with interfacial segregation, the effect of interfacial segregation on the interfacial cohesive energy in continuous fiber metal matrix composite materials can be numerically estimated by using Eq. [C4].

## ACKNOWLEDGMENT

The authors would like to express their appreciation to the Air Force Office of Scientific Research for the partial support of this study under contract.

## REFERENCES

1. J. P. Stark and H. L. Marcus: *Metall. Trans. A*, 1977, vol. 8A, pp. 1423-29.
2. M. Guttman: *Surf. Sci.*, 1975, vol. 53, pp. 213-27.
3. J. Kameda and C. J. McMahon: *Metall. Trans. A*, 1980, vol. 11A, pp. 91-101.
4. J. Kameda and C. J. McMahon: *Metall. Trans. A*, 1981, vol. 12A, pp. 31-37.
5. L. Brewer: in *Electronic Structure and Alloy Chemistry of the Transition Elements*, P. A. Beck, ed., Interscience Publishers, 1963, pp. 221-35.
6. *Metals Handbook*, 8th edition, ASM, 1973, vol. 8.
7. R. A. Swalin: *Thermodynamics of Solids*, John Wiley & Sons, 1962.
8. H. L. Marcus, M. E. Fine, and L. H. Schwartz: *J. Appl. Phys.*, 1967, vol. 38, pp. 4750-58.
9. C. J. McMahon: *Mar. Sci. Eng.*, 1976, vol. 25, pp. 233-39.
10. B. J. Schulz and C. J. McMahon: in *Temper Embrittlement of Alloy Steels*, D. L. Newhouse, ed., ASTM STP 499, ASTM, 1972, pp. 91-103.
11. H. L. Marcus, L. H. Hackett, and P. W. Palmberg: in *Temper Embrittlement of Alloy Steels*, D. L. Newhouse, ed., ASTM STP 499, ASTM, 1972, pp. 91-103.
12. C. J. McMahon, A. K. Cianelli, and H. C. Feng: *Metall. Trans. A*, 1977, vol. 8A, pp. 1055-57.
13. H. Otani, H. C. Feng, and C. J. McMahon: *Metall. Trans.*, 1974, vol. 5, pp. 516-18.
14. H. Otani, H. C. Feng, and C. J. McMahon: *Metall. Trans. A*, 1976, vol. 7A, pp. 1123-31.
15. R. A. Mulford, C. J. McMahon, D. P. Pope, and H. C. Feng: *Metall. Trans. A*, 1976, vol. 7A, pp. 1183-95.
16. R. A. Mulford, C. J. McMahon, D. P. Pope, and H. C. Feng: *Metall. Trans. A*, 1976, vol. 7A, pp. 1269-74.
17. J. Yu and C. J. McMahon: *Metall. Trans. A*, 1980, vol. 11A, pp. 291-300.
18. P. R. Krahe and M. Guttman: *Scripta Met.*, 1973, vol. 7, pp. 387-94.
19. M. Guttman, P. R. Krahe, F. Abel, G. Amsel, M. Bruneaux, and C. Cohen: *Metall. Trans.*, 1974, vol. 5, pp. 167-77.
20. J. P. Coad, J. C. Riviere, M. Guttman, and P. R. Krahe: *Acta Metall.*, 1977, vol. 25, pp. 161-71.
21. M. P. Seah: *Acta Metall.*, 1980, vol. 28, pp. 955-62.
22. R. J. Asaro: *Phil. Trans. R. Soc. Lond.*, 1980, vol. A295, pp. 151-63.
23. J. P. Hirth and J. R. Rice: *Metall. Trans. A*, 1980, vol. 11A, pp. 1501-11.
24. C. J. McMahon, V. Vitek, and F. R. Belton: *Scripta Met.*, 1978, vol. 12, pp. 785-89.
25. C. J. McMahon and V. Vitek: *Acta Metall.*, 1979, vol. 27, pp. 507-13.
26. W. Losch: *Acta Metall.*, 1979, vol. 27, pp. 567-73.
27. W. Losch: *ibid.*, pp. 1885-92.
28. C. L. Briant and R. P. Messmer: *Phil. Mag. B*, 1980, vol. 42, pp. 569-76.

29. R. P. Messmer and C. L. Briant: *Acta Metall.*, 1982, vol. 30, pp. 457-67.
30. C. L. Briant and R. P. Messmer: *ibid.*, pp. 1811-18.
31. M. Guttman and D. McLean: in *Interfacial Segregation*, W. C. Johnson and J. M. Blakely, eds., ASM, 1979, pp. 251-348.
32. D. Y. Lee and H. L. Marcus: in *Metallurgical Treatises*, J. K. Tien and J. F. Elliott, eds., TMS-AIME, 1981, pp. 571-87.
33. J. R. Griffiths and D. R. J. Owen: *J. Mech. Phys. Solids*, 1971, vol. 19, pp. 419-31.
34. P. W. Palmberg, G. E. Riach, R. E. Weber, and N. C. MacDonald: *Handbook of Auger Electron Spectroscopy*, Physical Electronic Industries, 1976.
35. M. Schmerling, D. Finello, and H. L. Marcus: *Scripta Met.*, 1980, vol. 14, pp. 1135-38.
36. M. P. Seah: *Acta Metall.*, 1977, vol. 25, pp. 345-57.
37. P. L. Gruzin and V. V. Minal: *Phys. Met. Metallogr.*, 1963, vol. 16, pp. 551-56.
38. C. L. Briant: *Scripta Met.*, 1981, vol. 15, pp. 1013-18.
39. M. L. Jokl, V. Vitek, and C. J. McMahon: *Acta Metall.*, 1980, vol. 28, pp. 1479-88.
40. M. L. Jokl, J. Kameda, C. J. McMahon, and V. Vitek: *Met. Sci.*, 1980, vol. 14, pp. 375-84.
41. D. Y. Lee: Ph.D. Dissertation, The University of Texas at Austin, 1983.

## APPENDIX I

TEM AND EELS INTERFACIAL STUDIES OF Ti  
METAL MATRIX COMPOSITES

Li-Jiuan Fu, M. Schmerling, L. Rabenberg  
and H.L. Marcus  
Center for Materials Science and Engineering  
The University of Texas  
Austin, TX 78712

Introduction

The interface of Ti MMC plays a significant role in the mechanical properties [1-5]. In terms of the fiber, the matrix, the processing and elements diffused down the interface, extremely complex interfaces can be established. To establish the chemical and crystallography of the interface ion thinned specimens were studied using TEM and EELS. Some TEM results had been reported in the literature [6] describing the morphology and phases present at the interface.

The results of the TEM/EELS studies are reported here. The materials analyzed are the Ti-6Al-4V metal matrix composites containing continuous SiC, B<sub>4</sub>C/B and Borsic fibers.

Sample Preparation

In order to perform the TEM interfacial analysis, 150-200  $\mu\text{m}$  transverse sections were cut with a diamond cutting wheel. The specimen was then glued to a glass slide and thinned with a 9  $\mu\text{m}$  diamond paste on a glass plate followed by 3  $\mu\text{m}$  diamond paste for the final polishing. The sample was approximately 30  $\mu\text{m}$  thick and

was ready for ion beam thinning. It should be noted that diamond paste on a nylon cloth did not work for the thinning operation.

An Edwards IBT 200 ion beam accessory was used to prepare the TEM specimens. It was found that at the 20° tilting angle (the specimen plane with respect to the incident ion beam), the 6 Kev accelerating ion beam voltage would sputter the Ti metal matrix faster than the three kinds of fibers, Fig. 1a. If the accelerating voltage was adjusted to 5½ Kev, fiber sputtering was observable, Fig. 1b. The large fiber diameter leads to easy breakout from specimen surface. Therefore, extreme care must be taken to preserve the composite interface.

#### Interface TEM Results and Discussion

In the as-received Ti/SiC MMC specimens, many phases were present at the interface. These include TiO, TiC and TiO<sub>2</sub>. The TiC results are shown in Fig. 2 and the TiO<sub>2</sub> in Fig. 3. Following thermal cycling of the Ti/SiC MMC in the sulfur environments TiS<sub>2</sub> was found at the interface. The comparison of d spacing data of TiS<sub>2</sub> diffraction pattern with the many other Ti-sulfide compounds showed that the TiS<sub>2</sub> was the main one formed.

In the Ti/B<sub>4</sub>C/B MMC the compounds TiO and TiB<sub>2</sub> were found in the interfaces. This was in samples in the as-received condition. The TiB<sub>2</sub> is shown in Fig. 4.

The interface of Ti/Borsic MMC shows the SiC layer of the borsic fiber as confirmed by STEM-EELS and TEM (Fig. 5). Near to the Ti matrix there is a thin layer which was indexed as TiC. The EELS spectrum taken from this region shows Si, C and Ti (Fig. 6). Since

Ti+SiC will yield TiC+Si thermodynamically, it is probable that this region contains TiC with Si either dissolved in the TiC or possibly as an amorphous oxide. The oxygen could not be identified in EELS because the O edge is very close to the Ti edge.

The limited results found here clearly show how complex the interfaces are in the Ti MMC. The chemistry and crystallography will strongly depend on the method of preparation as well as the subsequent thermal and mechanical exposure.

#### References

1. D.S. Mahulikar, Y.H. Park and H.L. Marcus, "Mixed Mode Crack Propagation in Continuous Fiber Metal Matrix Composites," Proceedings of the Greece/USA Mixed Mode Fracture Conference, Athens, Greece; Sih, G.C. and Theocaris, P.S., Editors, Sijthoff and Noordhoff, p. 385 (1981).
2. D.S. Mahulikar, Y.H. Park and H.L. Marcus, "Environmental Influences on the Fracture and Fatigue Properties of Titanium Metal Matrix Continuous Fiber Composites," in Fracture Mechanics, Fourteenth Symposium, J.C. Lewis and G. Sines, eds. ASTM-STP 791, vol. II, 1983, pp. 579-597 (Philadelphia, PA).
3. Y.H. Park and H.L. Marcus, "Influence of Interface Degradation and Environment on the Thermal and Fracture Fatigue Properties of Titanium Matrix/Continuous SiC Fiber Composites," in Mechanical Behavior of Metal-Matrix Composites, J.E. Hack and M.F. Amateau, eds., 1983, TMS-AIME:New York, pp. 65-75.
4. Y.H. Park, D. Narayen and H.L. Marcus, "Interface Diffusion Studies in Titanium Metal Matrix/Continuous SiC and B<sub>4</sub>C/B Fiber Composites," in press, MS&E, 1984.
5. Deepak Mahulikar and H.L. Marcus, "Mixed Mode Fracture in Titanium Metal Matrix Composites," Theoretical and Applied Fracture Mechanics, 1984.
6. C.G. Rhodes and R.A. Spurling, Recent Advances in Composites in the United States and Japan, ASTM STP 864, J.R. Vinson and M. Taya, eds., in press, 1984.

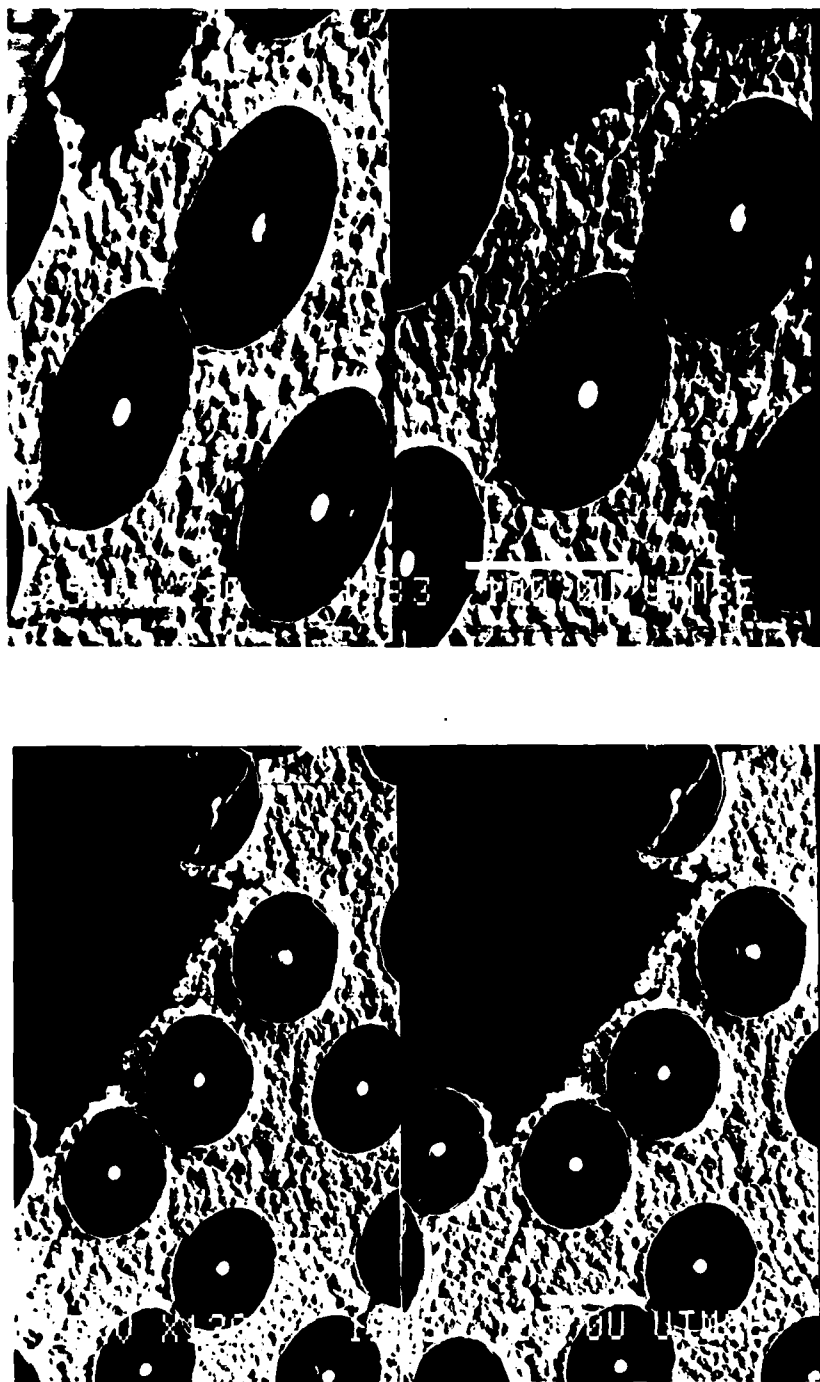


Fig. 1. Ion beam thinning of Ti MMC. The SEM stereo pairs show that:  
(a) After sputtering at 6 Kev the fibers have not been sputtered sufficiently so they are thicker than the Ti Matrix.  
(b) After adjusting the ion beam accelerating voltage to 5.5 Kev, the fibers were about the same thickness as the matrix.



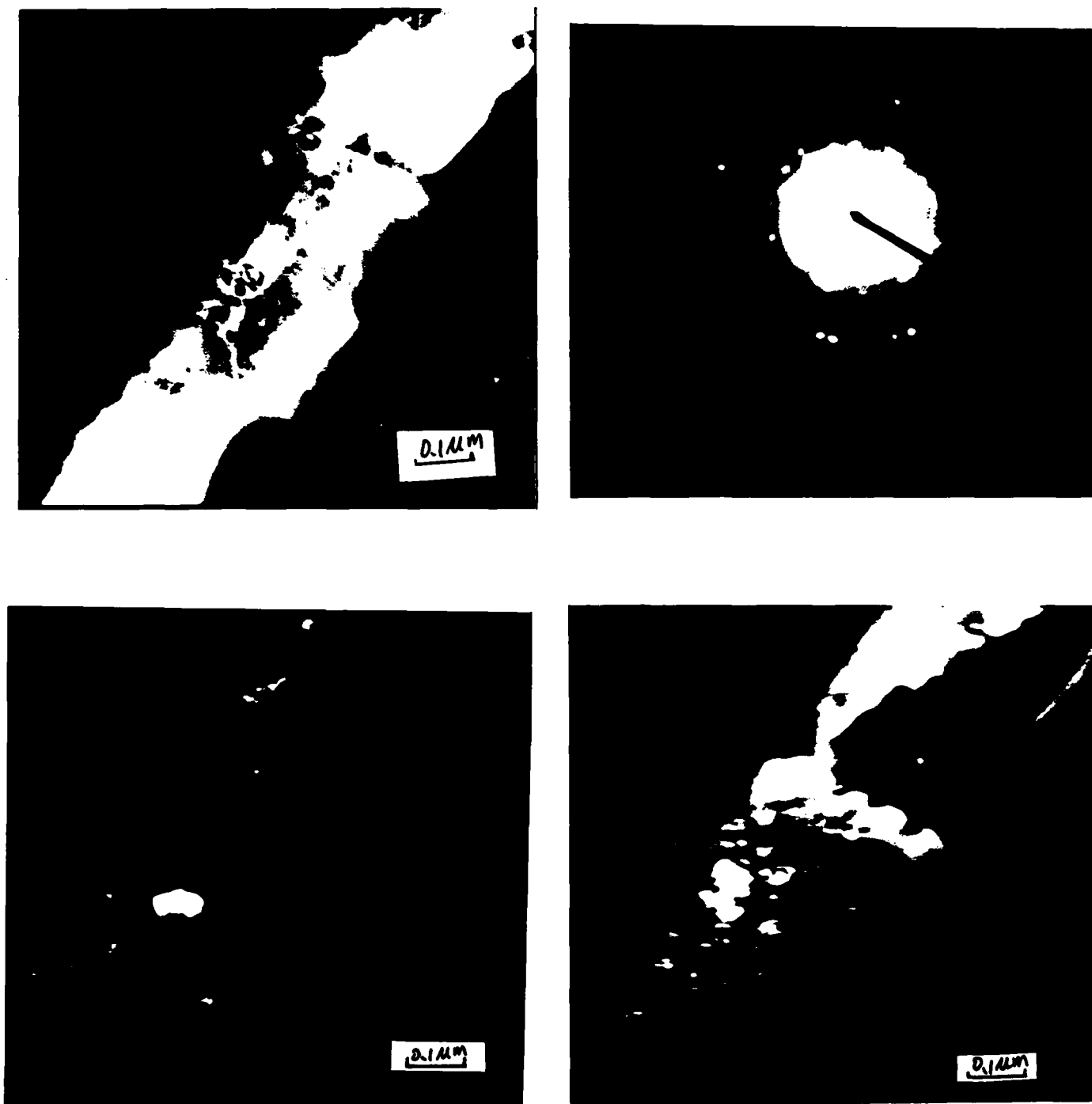


Fig. 2. TiC was found in the interface of as-received Ti/SiC MMC.

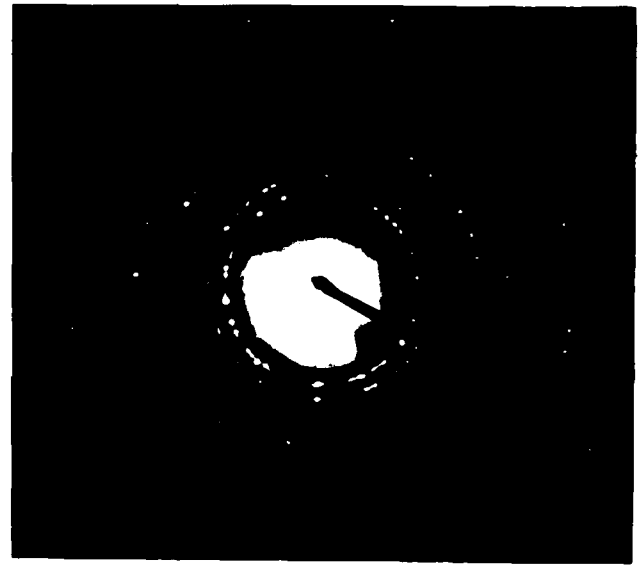


Fig. 3.  $\text{TiO}_2$  in Ti/SiC MMC interface.

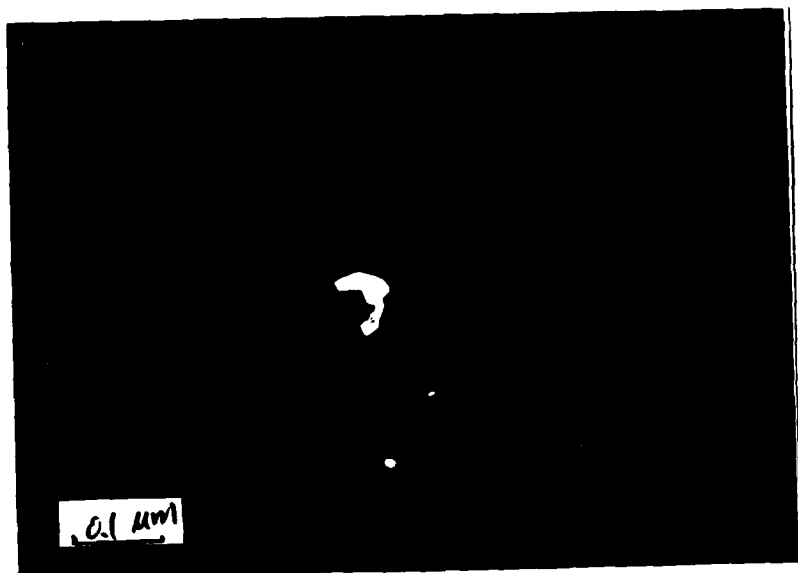


Fig. 4.  $\text{TiB}_2$  was found in the interface of Ti/ $\text{B}_4\text{C}$ /B MMC.  
(a) diffraction pattern; (b) bright field; (c) dark field  
of  $\text{TiB}_2$ .



B                      S: C                      T: C                      T: i

Fig. 5. Interface area of Borsic fiber; SiC layer, TiC layer and Ti matrix.

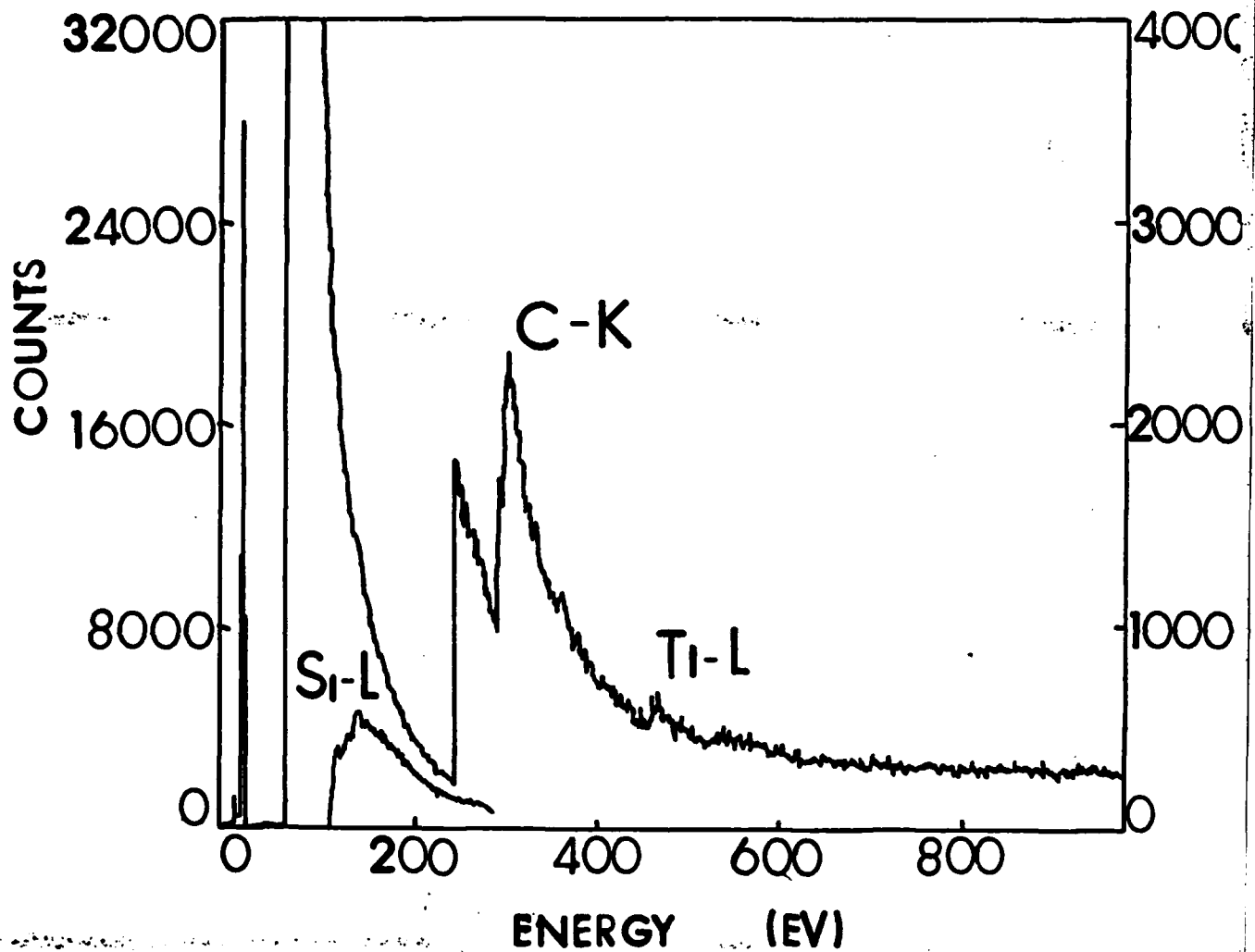


Fig. 6. STEM-EELS spectrum shows that there is a thin TiC interface layer with a little Si near to the Ti matrix of the Ti/Borsic MMC.